Collision Dynamics as a tool to Investigate the Interactions of Radicals with Liquid Surfaces

Kerry Louise Relf

A thesis presented for the degree of Doctor of Philosophy

Heriot-Watt University

Institute of Chemical Sciences

February 2014

Abstract

This thesis presents new results which are aimed at furthering the understanding of collision dynamics at gas-liquid interfaces. These experiments included the use of open shell radicals such as OH and both ground sate O(^{3}P) and excited state O(^{1}D) oxygen. The liquids used included an un-reactive standard per fluoropolyether, Krytox 1506 but were mostly focussed on the potentially reactive saturated and unsaturated counterparts squalane and squalene. The products of scattering from these liquid surfaces were detected by laser induced fluorescence (LIF).

The radicals were all used as a "chemical probe" of the liquid surface. Using information on the translational and internal energy distributions of the scattered species the structure and reactivity of each liquid surface could be investigated. Important findings included the first measurements of the reaction of O(^{1}D) with a liquid hydrocarbon surface. The data collected were analysed to provide the first comparisons of O(^{1}D) scattering from a liquid with previous gas phase measurements. Relevant mechanisms identified for these comparable gas-phase reactions were assigned as far as possible to the new results.

For the first time, the interactions of rotationally excited OH radicals with liquid surfaces were investigated. Liquid surfaces of atmospheric relevance were studied. This work was compared to that completed previously using a rotationally near-thermal source of OH radicals. Important scattering mechanisms were identified and assigned to the results collected. A possible loss mechanism for OH radicals interacting with unsaturated species was identified.

The first comparison of the interfacial reaction of O(^{3}P), with squalane and its unsaturated counterpart, squalene was conducted. Scattering mechanisms were identified and characterised where possible. Differences in scattering dynamics were observed with the unsaturated liquid surface, which were attributed to differences in the chemical nature of the bonds present in the liquid. Where possible, all results were related to reactions which occur in the atmosphere.

Acknowledgements

In the first instance I would like to thank my primary supervisor Professor Ken McKendrick. I really appreciate the great amount of time spent in suggesting additions and alterations to this work. His willingness to answer all questions (no matter how trivial) and seemingly endless knowledge in all areas of chemistry were greatly accepted.

Massive thanks are also due to Dr. Matt Costen, whose daily visits to the lab were always informative, often spotting problems before I did. His almost computer-like ability to recall constants and compute complex calculations is astounding.

Thanks to all past and present members of the group including Dr. Tom Sharples, Maria Serrate, Sarah Causier, Dr. Paul Bagot, Marija Iljina and Giovanni Rossi. In particular, thanks must go to Dr. Carla Waring-Kidd for being my mentor for the first few months and explaining how everything works and Dr. Grant Paterson for his great theoretical knowledge and tried and tested method for realigning laser beams. Thanks also to Iain Drummond for being able to fix absolutely anything. A special mention must go to Stephen McGurk, together we shared the whole PhD experience and he never failed to make me smile when my experiment wasn't working. My personal highlights included the drinking straw glasses, the bike incident and the afternoon of emergency button madness.

Thanks to all my family for always supporting me and often listening politely with blank looks when I try and explain my work. Special sister points must go to Gill who spent ages reading this thesis from a non-scientist point of view. Your dedication is admirable! Thanks to my friends for still being there after the whole thesis writing social hiatus.

One of the biggest thanks must go to my parents; for all of your time, your love and support (and sometimes sneaky monetary donations) have never and will never go unnoticed.

Finally thank you to my husband Andrew. Your patience is amazing, your calmness unwavering and your enthusiasm infectious. If it wasn't for you I would never have got here.

Table of Contents

Chapter 1: Introduction

1.1: Objectives

The aims of this thesis are to improve the current understanding of reactions at the gas-liquid interface, infer the nature of the liquid surface and, where relevant, relate results to reactions which occur in atmospheric chemistry.

Specifically, the work presented here is built on previous work on the dynamics of hydrogen abstraction by an $O(^3P)$ atom at a saturated liquid hydrocarbon surface. This work will be expanded to study the reaction dynamics of $O(^3P)$ atoms with an unsaturated liquid hydrocarbon and compare the reaction mechanisms and collision dynamics (Chapter 6).

This thesis will also explore the reaction dynamics of the excited singlet state of oxygen ($O(^1D)$) with a saturated liquid hydrocarbon (Chapter 4). This work will be compared and contrasted with the work on the ground state ($O(^3P)$) of oxygen (Chapter 6).

Finally, results are presented on the interaction of rotationally hot OH, generated from photolysis of allyl alcohol, with both saturated and unsaturated hydrocarbons (Chapter 5). This work is compared and contrasted to earlier work on OH generated from HONO photolysis with a near-thermal rotational temperature.

In all cases, the properties of the scattered species will be compared to pre-collision species. The effect the nature of the liquid surface has on these properties will be investigated and where applicable the possible mechanisms for reaction identified.

1.2: Motivation

The motivation behind this work is to gain a better understanding of collision dynamics at the gas-liquid interface and what inferences about the physical and chemical properties of the liquid may be drawn from this. Heterogeneous gas-liquid interactions are less well understood than their counterpart gas-solid or homogeneous gaseous reactions. This may in part be due to the fact that liquids are harder to study. Due to the low pressures required to study the nascent gaseous products of the reaction, only certain liquids with suitable physical properties (i.e. a low vapour pressure) may be

used. Yet despite the limited knowledge on this subject, it is known that gas-liquid processes are vital to a number of areas of chemistry including combustion, distillation and atmospheric chemistry. It is hoped that the work presented in this thesis will address some of the questions which have arisen as a result of this knowledge gap.

The work presented here is mainly centred around the reactions of both the ground ($O(^3P)$) state of oxygen as well as the hydroxyl radical (OH) with organic liquids. There are not many comparative studies of the excited state of oxygen ($O(^1D)$) and it is all conducted in the gas phase. As a result of this the background literature will be presented in the appropriate chapter (Chapter 4) while that presented here will concentrate on investigations relevant to the $O(^3P)$ and OH chapters (5 and 6).

One specific motivation for the study of $O(^3P)$ atoms with liquid hydrocarbons is the erosion of polymeric materials on spacecraft in a low Earth orbit (LEO), which ranges from 200 – 700 km above the Earth [1]. Within these boundaries $O(^3P)$ is the most abundant neutral species. Due to the orbital motion, effectively stationary atmospheric constituents collide with spacecraft at energies of around 5 eV (~480 kJ mol^{-1}). These high collision energies can lead to substantial permanent damage to essential technical components such as solar panels or protective materials. This is therefore a topic of interest to space agencies and technology manufacturers.

$O(^3P)$, $O(^1D)$ and OH are important in the cycle by which aerosols are oxidised in the atmosphere. An aerosol is a suspension of fine solid or liquid particles in a gas. In this case, our study uses liquid surfaces which can be considered as proxies for the liquid component of aerosols. The liquid portion of aerosols can have many functional groups such as acids, alkyl, unsaturated or aromatic. Specific examples of these include: carboxylic acids such as oleic acid; alkanes such as squalane; unsaturated alkenes such as squalene; and aromatics such as cyclohexane. The structure of some aerosols has been proposed [2] to consist of an organic hydrophobic layer coating an inorganic hydrophilic layer, with an inverted micelle-type structure (Figure 1.1). As the outer layer resembles an organic liquid, these can be used as proxies for atmospheric aerosols in laboratory studies such as those presented here.

The importance of investigating these proxies is that in the atmosphere, the aerosol must be oxidised (known as aging) if it is to become hydrophilic. As this complex

reaction progresses, the aerosols begin to collect water and eventually form raindrops: the aerosols are then functioning as cloud condensation nuclei. This is an extremely important process as it is partly responsible for the formation of rain which is vital to the survival of life on Earth. Aging also affects the optical properties of the aerosol and is one of the most poorly understood aspects of atmospheric chemistry [3]. It should now be evident that an understanding of the reactions of radicals with organic aerosol proxies would be an important step in deciphering the mechanism of aerosol aging.

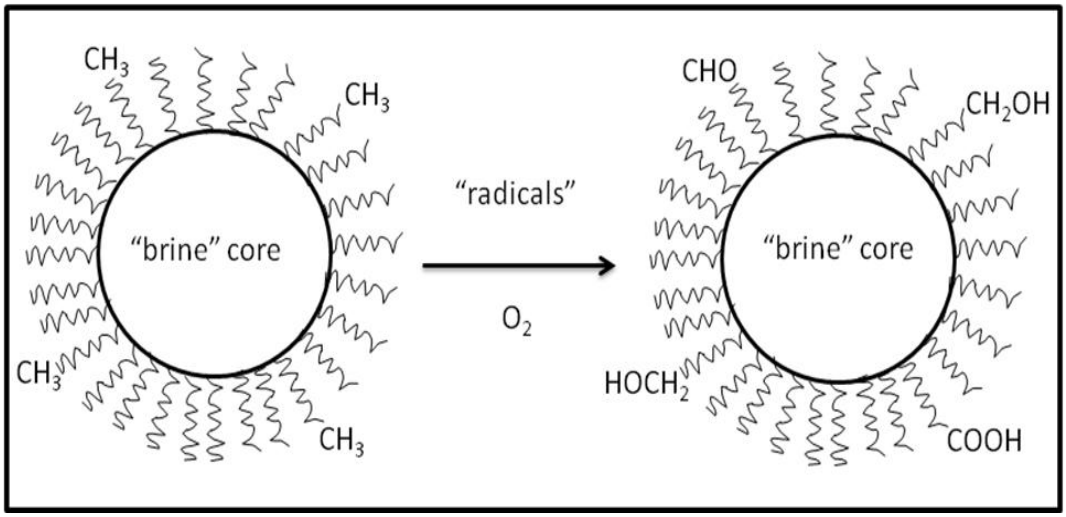

Figure 1.1: The proposed micelle-like structure of the aerosols shown to age by the action of radicals. Figure adapted from: Ellison *et al*. J. Geophys. Res **1999,** *104*, 11633.

1.3: Atmospheric chemistry

In the past few decades, great leaps have been made to understand the processes which occur in the atmosphere. The action of aerosols is one of the aspects of atmospheric chemistry which is least well known. It is known that aerosols can cause pollution, have an impact on the Earth's climate and may even be responsible for a negative radiative forcing. Aerosols are also involved in rainfall through their actions as cloud condensation nuclei (CCN), as introduced above. Although these processes have been documented [3, 4], the underlying chemical mechanisms are not well understood. By applying knowledge from the study of dynamics to the field of atmospheric chemistry it may be possible to design experiments which can help to clarify some of these unknown interactions.

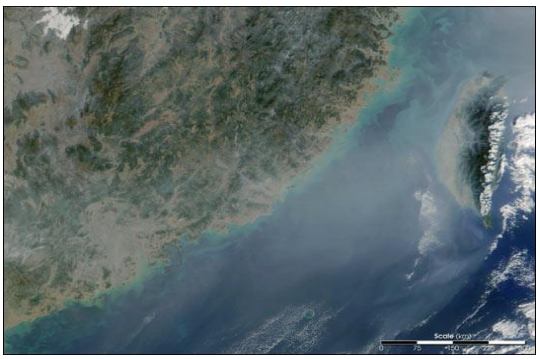

Figure 1.2: Aerosol pollution over China as shown from the NASA Terra satellite in 2002. Figure taken from http://earthobservatory.nasa.gov/IOTD/view.php?id=1608

1.3.1: Dynamics

The main aim of collision dynamics is to understand how molecules change when they interact with one another. This interaction may vary the physical state of the initial species or may result in a new species being formed. Understanding how these collisions affect the properties of the molecules involved and how they react is vital in many areas of chemistry.

1.4: Review of experimental work relevant to $O(^3P)$, $O(^1D)$ and OH scattering

1.4.1: Gas-phase studies pertaining to new results presented in this thesis

Most of the earliest work on collision dynamics was performed in the gas phase. These types of studies are of less direct relevance to the studies conducted here but are useful for assessing mechanistically what type of interactions may occur as long as care is taken to exclude any that are not possible in a condensed phase.

The area of the current work where the gaseous studies play a larger role as a basis for comparison is in the study of $O(^1D)$ radicals with liquid hydrocarbons (Chapter 4). At the time of this study there were no papers published on the subject of $O(^1D)$ interactions with a liquid hydrocarbon surface. Therefore the nearest equivalents to the work presented here are the homogeneous gas phase reactions. For that reason those studies will be discussed in greater detail in the appropriate chapter (Chapter 4).

For OH inelastic energy transfer in the gas-phase, there are a vast number of studies which exist. As the gas-phase studies cannot provide a direct comparison to the new

results on gas-liquid scattering this section is not intended as a comprehensive review of the area. A few key studies have been identified which are applicable to the scope of this work.

A representative early study was performed by Crosley and co-workers. Who measured parity propensities and energy transfer of the OH molecules during collisions with helium using laser induced fluorescence (LIF) [5]. They found that rotational energy transfer occurred in all cases. These results were echoed by Ter Meulen and co-workers who have performed several studies of OH collisions with other species in the gas-phase. These include He, Ar, H_2, CO, N_2 and CO_2 [6-8]. Their findings were that rotational energy transfer was efficient with nearly all colliders but parity preferences varied greatly with different collider gases.

More relevant to the experimental set–up presented in Chapter 2 is the study conducted by Farrow and Kliner [9], where a broad rotational distribution of OH was prepared by photolysis of H_2O_2. The collisional relaxation of OH with various colliders such as Ar, N_2 and O_2 was monitored by LIF. These experiments showed a curvature in the Boltzmann plot constructed to measure relaxation which may indicate the presence of more than one collision mechanism.

A great deal of the recent studies concluded on the topic of $O(^3P)$ collisions in the gas-phase have been performed by Minton and co-workers. The group have utilised a crossed molecular beam in their experimental set-up with products detected by a velocity map imaging detector which employs resonance enhanced multi-photon ionization (REMPI).

The investigations the group have completed include the collisions of $O(^3P)$ with a wide range of species such as H_2, D_2 and CO [10-12]. The studies most relevant to the scope of the work presented here are those that encompass the use of a hydrocarbon species in collision with the $O(^3P)$ atoms such methane [13] and ethane [14]. The problem with direct comparisons with the Minton studies, is that most were collected with $O(^3P)$ which had kinetic energy much higher than the energies used here (Chapter 6). The studies completed by the Minton group are discussed further in Chapter 6.

Andresen and Luntz used molecular beam techniques coupled with mass spectrometric detection to investigate the reactions of $O(^3P)$ with saturated hydrocarbons [15]. The study investigated the effects that abstracting primary, secondary and tertiary hydrogens on the product state distribution. The results showed that no lambda doublet preference existed in the products but that vibrational characteristics were highly dependent on the type of hydrogen abstracted. Primary hydrogens produced exclusively v' = 0, while secondary and tertiary produced both v' = 0 and v' = 1, with secondary producing more v' = 0 and tertiary producing more v' = 1.

Two large advances in the area occurred as a result of the work of Whitehead and co-workers. Who investigated the reaction of $O(^3P)$ with cyclohexane, cyclohexene and cyclohexadiene. The group monitored the OH formed from reaction using LIF. Their results showed that rotational distributions were very similar for all three gases with only modest quantities (1 -3 %) of energy being partitioned into rotation. The vibrational distributions exhibited only modest differences.

Whitehead and co-workers also conducted the first study using photolysis of NO_2 as a source of $O(^3P)$ for reaction with alkanes in the early 1990's [16]. This advancement was important as it allowed $O(^3P)$ to be studied in much higher concentrations as well as creating a definitive time zero in the reaction. This investigation utilised GeH_4 as the gas under study and paved the way for future investigations.

Perhaps the best summation of gas-phase literature relevant to the $O(^3P)$ experiments detailed in this thesis was produced by Ausfelder and McKendrick [17]. In this review the authors noted both LIF and spectroscopic detection were present but commented on the lack of studies completed using crossed molecular beams. The review summarised the main results collected from previous gas-phase studies. These key results included: a lack of rotational energy release, meaning product distributions were surprisingly cold; a surprisingly high spin-orbit splitting in favour of F_1 (discussed further in section 3.3.3) in varying ratios and a clear preference for increasing relative production of OH along the series primary < secondary < tertiary.

1.4.2: Studies using self-assembled monolayers

In recent years a new proxy for atmospheric aerosols has been developed, self-assembled monolayers (SAMs). These monolayers are formed from the attachment of

amphiphillic molecules to a suitable substrate. The most common type of SAM is the alkylthiol SAM which is formed from the spontaneous attachment of thiols onto gold substrates. The reason that SAMs can be used as a liquid proxy is their structure. Each individual chain of molecule attached to the substrate protrudes into the vacuum at an angle perpendicular to the substrate surface. When several strands are aligned together, the SAM is very organised (Figure 1.3), unlike a liquid surface. To an incoming collider, they begin to mimic a liquid surface due to the additional degrees of freedom afforded relative to a solid. An example of this is the ability of chains to sway from side to side.

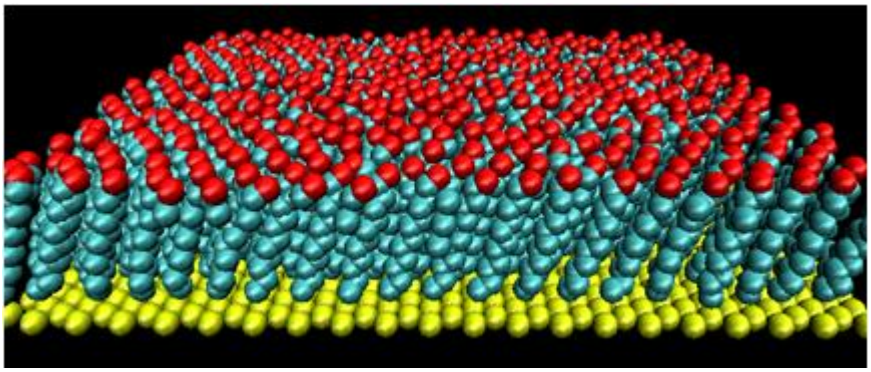

Figure 1.3: A representation of a SAM surface generated from a molecular dynamics simulation. Generated by Paul Bagot, Private communication.

1.4.3: Inelastic scattering from SAM surfaces

The work discussed in this section is the inelastic scattering of gaseous species from SAM surfaces. This type of work is most comparable to the OH results presented in Chapter 5.

One of the main drawbacks of using a SAM surface is that they can be destroyed when subjected to a high pressure or lengthy exposures of gas. This causes the amphiphillic chains to lie flat and sometimes holes to form (known as pitting) and can be detected by specialist types of microscopy such as scanning tunnelling microscopy (STM). A few studies have published results which show these structural changes occurring [18-21]. Once these changes have occurred, the SAM no longer behaves like a liquid proxy. For this reason, this introduction will concentrate on studies where no structural changes were observed.

The earliest SAM experiments were carried out by Cohen, Naaman and Sagiv two and a half decades ago [22]. Their investigation centred on the translational energy transfer of four gases to both fluorine (PTFE) and alkyl terminated (OTS and Cd(II) arachidate) SAMs. The gases used were He, Ar, O_2, and NO and the gaseous products were detected by mass spectrometry. In this study, the molecules exhibited a higher degree of thermalisation during collision with the SAM than those which comparatively collided with a bare substrate. For He, Ar and O_2, more kinetic energy was transferred to the surface of the alkylated SAM over the fluorinated SAM. NO was found to have roughly the same energy transfer quantities for both the alkyl and fluoro terminated SAMs. They also found that when comparing He and Ar collisions with the fluorinated surfaces that a greater quantity of kinetic energy transfer was observed for He (~28 %) over Ar (~4 %). The authors also postulated that some contamination could be present in their work, affecting their results. This stems from the fact that SAM surfaces cannot be refreshed and may change structure during exposure. This could not have been explored at the time but now STM can be used to detect these changes.

Since this seminal paper on the subject of inelastic collisions with SAM surfaces, two main experimental groups have investigated the inelastic collisions of gaseous species with SAMs. One of these groups is the Sibener group who have investigated the features of collisions of noble gases on SAM surfaces [23-25]. Their studies involve using mass spectrometry to detect gas-phase products.

In all of these inelastic scattering experiments, the translational energy distributions revealed a fast impulsive scattering component (IS) and a slower Maxwell-Boltzmann type thermally desorbed (TD) component. The study on argon [23] provided results where the TD component was well described by a cos θ angular distribution at the temperature of the surface. This indicates that the Ar molecules underwent a sufficient number of collisions to reflect the temperature of the surface. Conversely in the study on neon [24], the TD style component was found to be hotter than the liquid surface. This indicated that the Ne molecules were able to escape the liquid surface before becoming thermally accommodated. The authors proposed that these slow Ne molecules were due to high energy transfer events from single collisions.

In the experiments on xenon [25], these two reaction channels were observed along with a third channel which the authors identified as “directed ejection” scattering. This channel was proposed to arise from Xe molecules which had penetrated deep between alkyl chains and which were subsequently ejected at normal angles (relative to the SAM tilt angles) and with high energy when the chains returned to their equilibrium positions. This was exclusively seen in the Xe study but was speculated to be possible for other heavy projectiles due to their larger momentum.

The Morris group has also been prolific in performing studies in this area [26-39]. Their approach is similar to the Sibener group and utilises molecular beams coupled with a mass spectrometry detection system. They have investigated many aspects of dynamics of collisions of gaseous molecules with SAM surfaces. These include aspects such as how chain length [27], packing density [30] and surface density [32] affect the scattering dynamics. Only the aspects more relevant to the experimental work (in Chapters 4-6) will be studied in more detail.

In two of their earliest papers [26, 28], the Morris group investigated the effect that varying the terminal alkyl group has on the scattering dynamics. Methyl (-CH_3), alkene (-C=C), hydroxyl (-OH) and carboxylic acid (-COOH) groups were used in the study. The results showed that Ar thermally accommodated better in the alkyl terminated groups (-CH_3 and –C=C) which exhibited similar scattering dynamics. The hydrogen-bonded terminal groups (-OH and –COOH) formed less TD products and those IS products detected appeared to be travelling faster. This effect was attributed to kinematics as the hydrogen bonding makes the SAM surfaces more rigid and increases the effective mass.

Similar experiments were conducted later where the polar collider HCl was used to investigate the effects of terminal groups on scattering dynamics. In this case –OH and –CH_3 terminated SAMs were used [29, 31]. The polar HCl thermally accommodated well on both the alkyl and hydroxyl terminated group. This increase in hydroxyl thermal accommodation was attributed to the strong intermolecular forces between the two charges species which would “hold” the HCl molecule close to the SAM surface for a longer time, enabling thermal accommodation to occur. In these studies, the Morris group introduced a third distinct mechanism to the well known IS and TD

mechanisms. It was called “thermal accommodation followed by prompt desorption” and was distinct from the TD mechanism by the time spent trapped on the liquid surface. As the name implies, this mechanism involved only a short stay on the liquid surface. This mechanism was favoured over TD at higher surface temperatures and as the available thermal energy more readily overcomes the barrier to desorption.

The investigation into polar and non-polar colliders was completed with a very full study on the effects of surface and collider polarity [34]. This study involved the use of polar (ND_3 and D_2O) and non-polar (Ne and CD_4) gases from the usual non-polar alkyl ($-CH_3$) and polar (-OH and NH_2) terminated SAMs. The polar gases were thermally accommodated on both polar and non-polar SAM surfaces. The non-polar gases transferred more energy to the non-polar SAMs than the polar ones. The polar surfaces were found to be more rigid, causing less thermal accommodation. This effect was greatest in the Ne scattering where very little thermal accommodation was present at all. This effect was also seen by the Sibener group in their own Ne studies [24] where less thermal accommodation was observed than other gases. The Sibener group saw a quantitatively larger thermally accommodated component in their Ne experiments. This could be attributed to different collision energies (< 10 $kJmol^{-1}$ in the Sibener experiments and ~ 60 $kJmol^{-1}$ in the Morris experiments).

The final area of investigation for the Morris group was into the effects on the scattering dynamics of methyl, hydroxyl and perfluoro-terminated ($-CF_x$) monolayers in collision with Ar, CO, CO_2, NO_2 and O_3 gases [36, 38, 39]. In the study using argon [38], less energy is transferred to the –OH and $-CF_x$ terminated SAMs than the alkyl terminated ones. This is due to the hydrogen bonding network in the hydroxyl terminated SAMs as described earlier. In the perfluoro-terminated SAMs, this occurs as a result of the high effective mass of the perfluoro groups and the added degree of rigidity they impose on the SAM surface. CO_2, NO_2 and O_3 exhibit similar tendencies to accommodate more readily on all surfaces as a result of having a larger polarisability than Ar. This result is echoed by the CO molecule as it also exhibits a higher thermal accommodation than for Ar.

In all five experiments, the IS mechanism is dominant over the TD with more energy being lost in collision with the alkyl-terminated SAMs. This is due to the lower effective

mass of the alkyl groups coupled with the added degree of flexibility which makes them a more effective energy sink. The translational energy distribution of the IS channel is similar for all five gases. In all cases F-terminated SAMs generate more IS type molecules than alkyl or OH.

It is clear from the work above that a great deal can be learned from the inelastic scattering of gaseous colliders with SAM surfaces. However, it is important to note that differences between the SAM and gas-liquid surface do exist so direct comparisons should be performed with caution. These differences will be explored more closely in section 1.4.7. It is also important to note that all of the studies summarised here employ mass spectrometry as a method of detection and the field would benefit from a wider number of studies using different detection methods, such as has happened with gas-liquid studies.

1.4.4: Reactive scattering from SAM surfaces

The work summarised in this section is most comparable to the O(^{3}P) results presented in Chapter 6 but is also relevant to the OH results shown in Chapter 5.

There have been studies on the scattering of many different types of atmospherically relevant reactive species from SAM surfaces. These include atomic hydrogen [40, 41], ozone [42-45], and even charged species such as O^+ [46-48]. In this section, only those papers directly relevant to the experimental results which follow will be examined. They include the use of potentially reactive species such as O(^{3}P) and OH.

The pioneering papers on scattering of O(^{3}P) from SAM surfaces was performed by Paz, Trakhtenberg and Naaman in the early 1990's [49, 50]. In the earlier paper [49] they studied both the 18-carbon chain octadecyltrichlorosilane (OTS) SAM along with a simple methyltrichlorosilane (MTS) SAM. Results were obtained from contact angle measurements (wettability) as well as three types of infrared (IR) spectroscopy (external multi-reflection Fourier transform infrared (EXRIR); single pass direct absorption spectroscopy (DIAR) and attenuated total reflection (ATR) spectroscopy). In this experiment reactivity was measured as peak loss from an IR spectrum as well as with the contact angle measurements. It was found that OTS was much more reactive than MTS. Initially the authors thought that this was a result of the methylene groups in OTS having a lower barrier to reaction than the terminal methyl, and that they were

reacting. However, on continuing their experiment, it was found that the methyl group was reacting first in the OTS and the reaction of the methylene groups only occurred later. The rationale for OTS being more reactive was that the larger more complex surface accommodated the $O(^3P)$ atoms for a longer time period at the surface allowing more reactions to occur in OTS than for MTS.

Conducting the same experiment with a less ordered OTS sample, the authors found that the methylene groups reacted quickly, leading to a conclusion that the ordered structure of the SAM meant that the $O(^3P)$ could not immediately penetrate to the methylene groups to react. It was also found that as the surface temperature of the monolayer was increased, reaction in the methylene groups happened faster. The reason for this was proposed as a structural change from an all trans backbone to a cis-trans mix which may have made methylene groups more accessible.

In the later paper [50] X-ray photoelectron spectroscopy (XPS) was added to the analysis methods used and Fourier transform infrared spectroscopy (FTIR) was used in addition to the aforementioned wettability measurements. The study found that nearly all impinging $O(^3P)$ atoms react, regardless of their kinetic energy. The methyl groups present in the SAMs were found to react three times faster than comparative groups in the gas phase. Applying the same logic to the methylene groups, they reacted twenty five times faster than in the gas-phase. The authors postulated that the activation barrier in the SAM surface was much lower than in the corresponding gas-phase reactions. This fact is disputed by other papers summarised in the following few paragraphs [51, 52].

In more recent years the reaction of $O(^3P)$ atoms with self-assembled monolayers has been investigated by Fairbrother and co-workers [53, 54]. The group have used XPS to investigate the penetration depth of molecular oxygen into X-ray modified self-assembled monolayers.

Over the course of the two papers, the Fairbrother group found that semi-fluorinated SAMs were initially resistant to reaction until the oxygen atoms had permeated through the fluorine containing layer. In contrast the alkanethiolate SAMs reacted readily. In these studies, the reactions were allowed to progress until the carbon backbones of the SAM had begun to react and break off as CO_2. This indicates that

secondary reactions were occurring and, as a result of this, are not directly comparable to the result presented here where a continually refreshed liquid surface is used couple with low gas pressures to ensure single collision conditions as described in section 2.4.1.

Molina and co-workers conducted a study into the reactions of OH with methyl- and vinyl- terminated monolayers [55]. The experiments were carried out in a flow-tube style reactor with loss of OH was detected by chemical ionisation mass spectrometry (CIMS). This study provided a value for reaction probability (γ_{OH}), which is comparable to the results presented in Chapter 5.

In the study it was determined that the reaction probability of the methyl-terminated monolayer was 0.29 and the vinyl terminated monolayer was 0.6. The increased reactivity of the vinyl monolayer is probably due to the lower energy required to abstract a hydrogen.

Moussa and Finlayson-Pitts [56] conducted a study into the reaction of OH radicals with alkene-terminated monolayers (7-octenyltrichlorosilane). Loss of the reactant SAM and formation of other surface products such as organic nitrates and carbonyl compounds was monitored as the reaction progressed by FTIR.

The reaction probability measured for this reaction was indistinguishable from unity. This means that secondary reactions may have been present and that OH may have been lost in a collision which was not the primary encounter. This investigation is interesting as it also monitors the other products formed in the reactions and therefore gives an insight into how this reaction may further progress in the troposphere. However, as there is the possibility of secondary collisions involved in the experimental results, the reaction probability is not comparable to the work presented here.

The McKendrick group carried out a study on the reactions of $O(^3P)$ with SAM surfaces [51]. $O(^3P)$ was generated from NO_2 and products were detected by LIF. SAMs of chain length C_6 and C_{18} were studied. The investigation found that $O(^3P)$ reacted with the SAM surfaces to form OH but that only minor differences existed between the two chain lengths. This lead the authors to postulate that the $O(^3P)$ projectiles must

penetrate into the SAMs surfaces sufficiently to reach the more reactive secondary hydrogens but that they must not penetrate far beyond the first few carbon atoms. This led to a second study with SAM chains labelled to a different degree with deuterium [52]. This enabled the penetration of $O(^3P)$ projectiles into SAM chains to be further characterised. The findings showed that 16 ± 3% of projectiles reacted with hydrogens on C_1; 42 ± 5% of projectiles reacted with hydrogens on C_2; 42 ± 4% reacted with hydrogens on C_3 –C_6; and 0 ± < 4% reacted with hydrogens on C_7 – C_{12}.

The studies using SAM surfaces in reaction with gaseous species is a useful qualitative comparison to the work presented here. Identification of specific mechanisms and enhanced reactivity over gas-phase reactions is comparable with the work presented here. The main problem with SAM surfaces experimentally when compared to liquid surfaces is their inability to be refreshed during experiment. This means that often SAMs surfaces are destroyed during experiments. As a result of this, the experimental results may contain some OH generated from secondary collisions. This makes the work not directly comparable to the gas-liquid work presented here. Nevertheless these works provide a valuable background and aid with understanding of how reactions progress. The use of SAM surfaces and can show how aging of an aerosol may progress over time while gas-liquid experiments are useful in isolating the first step.

1.4.5: Gas-liquid experiments

Most directly comparable to the work presented in this thesis are other studies of gas-liquid scattering. This is a field which was relatively poorly studied but recently many papers have been generated on the subject. Heterogeneous gas-liquid studies are particularly interesting because they are the only type of experiment where a continually refreshed surface can be generated. This means that single direct encounters with the surface may be studied. This is in direct contrast to SAMs experiments where ensuring single collision conditions is very difficult to achieve. By using proxies for atmospheric aerosols as the liquid surfaces, an understanding of the first step of oxidation reactions which occur in the troposphere may begin to be understood. It is this importance coupled with the many different detection methods mentioned below which means this field has grown rapidly in recent years.

1.4.6: Inelastic scattering from gas-liquid interfaces

Inelastic scattering from gas-liquid surfaces has been more fully investigated than inelastic collisions from SAM surfaces. Investigations into this area began in the early 1990's and are still continuing presently.

One of the first groups to begin investigating this area was the McCaffery group. Their investigations involve using a molecular beam experiment coupled with LIF detection methods to investigate the scattering of I_2 from polydimethylsiloxane (PDMS), squalane, perfluorinated polyether (PFPE) and liquid and solid Gallium [57, 58].

The I_2 beam used in this experiment was translationally hot with a vibrational temperature of 100 K and a rotational temperature of 10 K. The delays between the laser pulses were varied to probe the direct IS channel at early times and then to probe the trapping desorption channel at later times. The results showed that for all liquids, a slight rotational warming was observed in the IS channel. This warming decreased in the order PDMS > PFPE > squalane. The increase in temperature for PFPE was 10 K. This slight warming is likely a result of a weak translational to rotational energy transfer in the I_2 molecules. A modest vibrational warming was observed from squalane and PFPE and vibrational cooling from PDMS. The authors suggested that that PDMS was better able to absorb energy from collisions due to the fact of having more surface modes available to absorb energy during collision. It seems unlikely that vibrational cooling would have been observed from PDMS as the surface was warmer than the vibrational temperature of the beam. The translational energy is also higher than the equivalent average vibrational energy.

The experiments on the TD channel showed that products exhibited more significant internal state excitation than the molecules in the pre-collision beam. This indicates that the cold pre-collision molecules undergo collisional thermalisation at the liquid surface, consistent with the presence of the trapping-desorption mechanism. The trend in internal energy present in the desorbed species was PDMS > squalane > PFPE. This shows that the nature of the liquid surface greatly affects how much energy is gained when the species undergoes trapping desorption. This gain occurs from a warming of initially cold molecules during trapping. In all cases, the I_2 molecules never undergo sufficient thermalisation to reflect the temperature of the liquid surface,

falling short in all cases. The reason for this incomplete thermalisation could be either due to inefficient energy transfer from the liquid surface or at the point in time when the experiment is conducted there may still be some IS mechanism present, which would affect the average rotational and vibrational temperatures of the scattered products.

The studies conducted by McCaffery and co-workers show that the scattering dynamics of the products are dependent on the nature of the liquid surface from which it scatters. This will be reflected in the results of the work presented here and is especially prominent in the results shown in Chapter 5.

The majority of studies in this area have been carried out by the Nathanson group. Beginning in the early 1990's the group have used a molecular-beam experiment coupled with mass spectrometric detection methods, to investigate the inelastic scattering dynamics of a large range of different systems [59-68]. Their experimental methodology involves the use of a rotating wheel to generate the refreshed liquid surface. The group have investigated a wide range of systems including scattering from liquid metal surfaces [63], sulphuric acid surfaces [66] and salty glycerol surfaces [68]. This summary will concentrate on the scattered species and liquid surfaces most relevant to the results presented in this thesis.

The Nathanson group were the first to observe that time of flight profiles were bimodal and introduced in the context of gas-liquid scattering the two types of mechanism which are now well known: the inelastic or impulsive scatter (IS) and the thermal desorption mechanism (TD).

In one of their earliest studies, the Nathanson group investigated the scattering of Ne, Ar and Xe from a perfluorinated polyether, PFPE, and a liquid hydrocarbon, squalane [60]. The results of the study showed that energy transfer to the liquid surface varied depending on the species scattered. The authors noted that the energy transfer was larger in the higher mass species meaning that these are more effectively trapped than lighter molecules. This study was later expanded to show that energy transfer was most efficient to the squalane surface. This was attributed to the lighter masses of the CH_x groups compared to the CF_x groups. The CH_x groups are comparable to the

scattering species in mass and therefore for simple kinematic reasons can absorb more energy during collision when compared to the much heavier CF_x groups.

In another early study, the effects of hydrogen bonding within a liquid were explored by investigating the collision dynamics of gases with varying polarity: Ne, CH_4, NH_3 and D_2O with a hydrogen bonded liquid (glycerol) and a non-hydrogen bonded one (squalane) [61]. The results of the study showed that the unpolarised gas species (neon and methane) were accommodated best on the non-polar liquid squalane while the most polar gas (D_2O) was accommodated best on the polar liquid, glycerol. This is a demonstration of the general chemical principal that charged species will dissolve well in one another as will uncharged species while a charged and neutral species do not mix well. The study showed that overall squalane accommodated the species which were not strongly attracted best due to the softer and rougher surface.

The Nathanson group have also investigated the effects of temperature on collisions of Ne, Ar and Xe with squalane and PFPE and how this affects the scattering dynamics [62]. The results showed that the impulsive scatter was unaffected by liquid temperature, confirming conclusions that these types of collisions are true single collision events. The TD component increased in magnitude at higher temperatures for Ar scattering. This may indicate that an increase in temperature results in surface roughening and therefore increases the liquid's ability to trap gas-phase molecules.

Using the molecular-beam experimental set-up it was possible for the Nathanson group to investigate the effects of incidence and scattering angle on the scattering dynamics of Ar atoms from PFPE [65]. The results demonstrated that at more normal approach angles, energy transfer and trapping at the PFPE surface increased while at more grazing angles only a small amount of energy was transferred to the liquid surface and trapping was suppressed.

More recently, the Nesbitt group has become involved in this area and have investigated thoroughly the scattering dynamics of CO_2 from liquid PFPE [69-71] and squalane [72]. The experimental set-up involves using a molecular beam of CO_2 usually with an energy of 44.4 $kJmol^{-1}$ coupled with a high-resolution infrared absorption spectroscopy detection method. This approach can provide information on the translational and internal energy distributions of the pre- and post-collision species.

The Nesbitt group identified the two now well-established types of scattering, IS and TD. When fitting the resultant scattered species to a Boltzmann type plot, they found that the CO_2 molecules fitted well to a two-temperature model. The authors concluded that the lower temperature resulted from the TD type mechanism while the higher temperature must occur as a result of IS.

The Nesbitt group found that the rotational temperature of the IS channel increased significantly in all cases from around 15 K in the pre-collision beam to ~ 600 K after collision. This effect was independent of which liquid was studied [72]. The TD component was found to reflect the temperature of the liquid surface. The vibrational temperature of the scattered species was also found to remain close to that of the ingoing beam. The Nesbitt group also found that when increasing the temperature of the liquid surface that an increase in the TD component was found which is in keeping with the results of the Nathanson group [62].

The previous sections have provided an overview of the literature relevant to the results presented in the course of this thesis. There has also been a great deal of OH scattering conducted by the McKendrick group using the same experimental set-up presented in this thesis. These papers are directly relevant but are discussed fully in section 5.2.1 to allow for easier comparison to the data presented in the same chapter. The following sections will provide an overview of complementary theoretical studies conducted in this area. As there are no new theoretical results presented in this thesis, the review will be brief, and only those studies most relevant to the new results presented here will be described.

1.4.7: Reactive scattering in gas-liquid experiments

Gas-liquid experiments have been much more extensively explored than the corresponding reactive gas-SAM experiments. Investigation into this area began in the 1970's and has been increasing ever since then. Limitations on the type of liquids able to be studied exist. As an example liquids must have a sufficiently low vapour pressure to survive under vacuum conditions. The papers relevant to the potentially reactive species used here will be reviewed. In this section that will mainly be on reactions of $O(^3P)$ with hydrocarbon liquid surfaces. This reaction mainly proceeds via a hydrogen abstraction at low energies to form OH as shown in equation 1.1. This means that for

this reaction to proceed a C-H bond must be broken. Within a hydrocarbon, the average C-H activation energies (in the gas phase) are tertiary (~21 kJ mol^{-1}) < secondary (~22 kJ mol^{-1}) < primary (~34 kJ mol^{-1}) < methane (~42 kJ mol^{-1}) as denoted in a recent review paper [17].

$$O(^3P) + RH \rightarrow OH\cdot + RH\cdot \qquad \text{- Equation 1.1}$$

An early paper on the subject of radical interactions with liquid surfaces was published by Jaeger and Ward in 1982 [73]. They investigated the reaction of $O(^3P)$ with cycloalkanes. In this experiment the $O(^3P)$ was produced by microwave discharge of CO_2. The main products were found to be tertiary alcohols formed when the $O(^3P)$ adds on to the molecule and then a rearrangement occurs. A secondary, more minor product observed was epoxides.

Around this time, McKendrick and co-workers performed the first investigations into the reactions of $O(^3P)$ with methane and ethane [74] along with isobutene, cyclohexane and deuterated cyclohexane [75]. The technique of LIF was also used here to detect the OH products. The results showed no lambda doublet preferences, in agreement with Andresen and Luntz [15]. The authors postulated that this occurred as a result of the collinear abstraction mechanism for the removal of hydrogen to form OH. Their results showed that a modest spin-orbit preference existed for the $^2\Pi_{3/2}$ state and proposed that this effect stemmed from selective non-adiabatic mixing of surfaces with the same parity and projection of electronic angular momentum on the intermolecular axis.

Kajimoto and co-workers produced the first paper where Doppler-resolved polarisation spectroscopy was used as a detection method in the reaction of $O(^3P)$ with saturated hydrocarbons [76]. This enabled the differential cross section (DCS) to be measured. Lower collision energies were already known to generate predominantly backscattered products, using previous techniques. Kajimoto and co-workers found that as the collision energy was raised from 12 to 33 kJ mol^{-1} there was an increase in the forward scattered intensity. The quantity of forward scattered products increased to eventually equal the number of backscattered products. The reason for this growing forward scattered component was proposed to be that the increased energy allowed

for a stripping mechanism with a larger impact parameter to become available as a viable reaction mechanism.

Suits and co-workers have used velocity map imaging (VMI) to detect the products of the reaction of $O(^3P)$ first with cyclohexane [77] and then with a range of saturated hydrocarbons [78] with varying collision energies. In contrast to the previous work of Kajimoto [76], scattering was always found to be predominantly backward, representative of a direct abstraction method. The results also showed that a significant fraction of energy is dissipated into the alkyl fragment rather than the OH product.

A study was conducted by Nesbitt and co-workers into the reactions of F atoms with liquid hydrocarbon surfaces [79, 80]. In this experiment an atomic beam of Fluorine was used and the HF (v'=2) products were detected by high resolution infrared spectroscopy. The HF product rotational distribution was found to be bimodal. This was proposed to arise from a direct process resulting in superthermal HF at around 1000 K and a thermal desorption type process resulting in rotationally thermalised HF.

One of the groups, most prolific in studying this area is the Minton group. Their work began in the late 1990's with the investigation of the reaction of $O(^3P)$ atoms with the liquid hydrocarbon squalane [81]. It is from this point that the literature becomes directly comparable to the results presented here (most notably in Chapter 6) as the use of the larger hydrocarbon liquid coupled with the more dynamical nature of the investigation becomes more compatible with the results given in this work.

The Minton group use a molecular-beam-based experimental technique coupled with rotatable quadrupole mass spectrometric detection. This combination can detect both angular and velocity distributions. The group also used a liquid covered wheel to continually refresh their liquid surface. This is similar in type to the wheel used to generate the surface in this work (discussed further in Chapter 2). Squalane was used as the saturated liquid hydrocarbon. Squalane is often chosen due to its low vapour pressure and other physical properties which make it easy to use. The $O(^3P)$ was generated first by a radio frequency discharge of O_2 and later in a unique manner from a CO_2 laser photolysis of O_2 in a plasma source. This method can generate a range of collision energies up to 5 eV.

In the earliest experiments [81, 82], two different beams of $O(^3P)$ atoms were used with translational energies of 21 and 47 kJ mol^{-1}, respectively. Both beams contained less than 5 % of $O(^1D)$ atoms. They observed both inelastic (O atoms) and reactive (OH) scattering. The OH observed was classified into two categories: thermal and hyperthermal. The hyperthermal mechanism was identified as a direct abstraction mechanism while the thermal was identified as a sequential thermal accommodation at the liquid surface followed by desorption. Also evident was a loss mechanism where a second hydrogen could be abstracted to form H_2O. No mechanism for the breaking of C-C bonds was observed.

The work of the Minton group was enhanced with the use of a plasma-breakdown source of $O(^3P)$ atoms [1, 83, 84]. Using this method of generation the collision energies of the $O(^3P)$ atoms could be made higher still while ensuring that there was no significant contribution from the excited oxygen ($O(^1D)$) atoms. The investigations showed that inelastic scattering of oxygen atoms must be the most dominant mechanism as oxygen atoms were the most abundant scattered species. Surprisingly, despite the high collision energies, thermal OH was observed which identifies a trapping mechanism which is efficient at energy dissipation.

OH was the most abundant reaction product observed, its signal size was dependent on collision energy. Higher energies produced a larger quantity of observed OH. The observed OH was found to have a bi-modal speed distribution where the fastest, directly scattered OH was dominant at grazing incidence angles while the slower moving TD component was observed at more normal incidence angles relative to the surface. The presence of this TD component indicates that a minor quantity of OH can be thermally accommodated at the surface and sometimes still escape without reacting further.

The reaction products which had twice abstracted hydrogen to form water, surprisingly also had a minor bi-modal product speed distributions. The majority of the observed water was thermalised at the liquid surface before desorbing and being detected. Conceptually it is surprising to have a hyperthermal distribution of water molecules as they are not formed from a single, direct reaction mechanism. It is

possible that two independent direct single encounters may have generated this result.

Further experiments were carried out by the Minton group [84] to investigate the possibility of H-elimination and C-C bond breakage – both of which were observed in the corresponding gas-phase studies with smaller hydrocarbons [13, 14]. The study identified a C-C bond breaking mechanism by the presence of the product OCH_3. Its angular product distribution was very similar to the OH one and appeared to be formed as the result of a direct mechanism. It was proposed that the O atom abstracted the CH_3 through a very fast, direct collision at the C-C bond. The translational distributions of the OCH_3 and OH were different. The OCH_3 travels much slower than the OH but has a similar angular distribution. This is partially due to the large amount of energy lost in the collision to abstract the CH_3 and partly due to the larger mass of OCH_3 compared to OH. Newton diagrams were constructed to calculate the effective surface mass for each type of collision. The effective mass of collision partner for the O atoms forming OH was ~ 76 atomic mass units. This means that the incoming oxygen atoms do not see the surface as infinitely massive but rather as discrete pockets of varying mass. Oxygen atoms which form OCH_3 were calculated to have a collision partner with an effective surface mass of 124 amu.

In the same study, the H-elimination mechanism could not be identified due to the high background and low detection sensitivity of the experiment. There were also problems in the experiment detecting hydrogen by mass spectrometry. It may be surprising that H-elimination was not observed while C-C bond breakage was as the group's own calculations put the percentage of C-C bond breakage occurring at 2.6 % while H-elimination was much higher at 43 %. It is possible that both of these mechanisms may have been present, with the H-elimination much harder to measure experimentally, which would be in direct agreement with the group's own gas-phase work [14].

The other group who have conducted many studies in the area of reactive scattering of molecules from liquid surfaces is the McKendrick group [85-90]. Their first paper investigating the reaction of $O(^3P)$ molecules with liquid squalane [85] indicated the versatility of the LIF technique. $O(^3P)$ molecules were generated by photolysis of NO_2

and the reaction product was detected by LIF. In this study, the group used a rotating wheel (similar to that used in the Minton group studies) to continually refresh the liquid surface.

Using their experimental set-up, appearance profiles could be collected which are analogous to the TOF profiles recorded with a molecular beam type set-up. These appearance profiles provided information on both the translational energy and (with multiple profiles) internal distributions of the final products. This type of experiment also enables multiple transitions to be studied within the same scan – known as an excitation spectrum. This type of spectrum enables the internal distributions of the final products to be characterised.

In this initial study, McKendrick and co-workers measured OH/OD vibrational branching ratios for squalane and its deuterated analogue. They detected a minor v' = 1 vibrationally excited component of $\frac{v' = 1}{v' = 0}$ = 0.07 for OH. In comparison with gas-phase studies [17] it was concluded that the vibrationally excited OH must stem from an abstraction of H from either secondary or tertiary groups or both. This conclusion led to the belief that these groups must be present at the surface of the liquid interface. The McKendrick group later performed molecular dynamics simulations to determine whether or not this belief was correct. These simulations are discussed further in section 1.5.1.

The McKendrick group expanded upon their initial investigation by conducting a study on the effect of varying surface temperature of the liquid squalane and how this affected the OH reaction product [86]. The rotational temperatures of the OH reaction product were found to partially reflect the liquid surface temperature. This was concluded to be a result of a short trapping on the liquid surface which was not enough to allow the OH products to reflect the surface temperature of the liquid but certainly influenced the temperature to a certain degree. Another possibility for this partial temperature change could be that a quantity of the OH radicals are fully thermally accommodated at the liquid surface before desorption while others perform a direct abstraction which results in little or no temperature change. The averaging of these two cases would provide an intermediate temperature change. In cases where the surface temperature of the liquid was varied by 60 K, the average temperature

variance of the OH products was ~ 311 K. This seems to indicate the presence of both a direct impulsive scatter (IS) as well as a complementary trapping desorption mechanism (TD). This seems to be supported further by the differences in temperature for the vibrationally relaxed OH versus the vibrationally excited OH. In a case where only a trapping mechanism was present the OH products would fully reflect the liquid surface temperature regardless of their vibrational state. In contrast, a fully direct mechanism would result in a larger temperature variance between the two vibrational levels.

A further study was concluded investigating varying temperature effects of the liquid surface in two vibrational states v' = 0 and v' = 1 [89]. The study was conducted over both vibrational levels at a range of temperatures from 263 K to 333 K. In v' = 0, the OH appearance profiles (analogous to TOF profiles) were independent of temperature change at early times and did not vary significantly in magnitude or shape. This is due to OH formed at early times being a result of a direct process. However, in v'=1, the OH products showed both an increase in overall yield and an increase in speed with increasing liquid temperature. McKendrick and co-workers concluded that the reason for the increased OH yield was due to an increase in the survival probability rather than in increased production of vibrationally excited OH. This was proposed as being caused by the higher temperature causing the squalane surface to become more open and hence become more easily escapable.

In a further study, the direct component was isolated and characterised by recording LIF excitation spectra of OH at early time delays which correspond to only the direct scattering mechanism [87]. Those scattered impulsively were found not to suffer from temperature changes as the temperature of the liquid surface was varied as would be expected for a direct single collision where no residence time was spent on the liquid surface. The rest of the OH properties in this study were reminiscent of gas-phase work such as rotational temperature and variation of rotational temperature in accordance with vibrational excitation [74]. This led to a conclusion that the direct nature of this impulsive scatter was similar to gas-phase abstraction mechanisms.

The final study in this area from the McKendrick group was on how the molecular structure of the liquid molecules affected the dynamics of the OH products [90]. In this

study the range of liquids used was extended to include a range of linear and branched hydrocarbons. Similar OH internal state distributions were observed from all liquids. The differences occurred in the OH yield from each liquid. The alternative branched hydrocarbon to squalane used was pristane ($C_{19}H_{40}$). Pristane was found to be less reactive than squalane but only by a reasonable amount comparable to the proportion of different C-H bond types.

When comparing the linear and branched hydrocarbons, the linear hydrocarbons were found to be less reactive. This was initially surprising as there are fewer primary sites in the linear hydrocarbons which are known to be less reactive. The study also showed that shorter linear molecules were lower in reactivity than the longer ones in a ratio which was surprising. This was identified as a result of the proportion of secondary sites along the chain compared to primary sites at chain ends. This reduction in reactivity was attributed to a phenomenon known as “surface freezing” where chains are frozen in a certain orientation allowing only specific sites to be available for reaction. McKendrick and co-workers investigated this with molecular dynamics simulations which will be discussed in more detail along with the surface freezing phenomenon in section 1.5.1.

The area of gas-liquid reactive scattering has been furthered greatly in the last few decades. The use of differing experimental techniques coupled with varying reactive projectiles and liquid surfaces provides a very strong foundation to build on. These experimental studies are often complemented by theoretical investigations which will be discussed in section 1.5.6.

1.5: Previous theoretical work

1.5.1: Molecular dynamics simulations of gas-liquid interfaces

The volume of theoretical papers published on collision dynamics of gas-liquid scattering is not as large as the experimental studies. Recently, the theoretical models used have been developed and can now well describe these types of interactions, leading to an increasing number of studies to be published. The types of modelling used currently are Quantum mechanical/molecular mechanic modelling (QM/MM). Earlier in time, a simpler form of the molecular mechanic modelling was used. These simpler simulations were known as molecular dynamics simulations.

The first paper of this type was published by Harris in 1992 [91]. He modelled linear hydrocarbons decane ($C_{10}H_{22}$) and eicosane ($C_{20}H_{42}$) by using a united atom approach. United atom models treat groups of atoms rather than each individual atom separately, for example each CH_2 is treated as one group. This means that the CH_3 and CH_2 units were treated as pseudo-atoms where hydrogen atoms were not represented explicitly. Realistic bond lengths, angles and torsional potentials were included as parameters in the simulation. Around 300 molecules were included in the simulation volume on which periodic boundary conditions were imposed in all directions. Random velocities from a Maxwell-Boltzmann distribution were assigned and the system was allowed to equilibrate.

The results of the simulation showed that most of the liquid properties could be accurately predicted by the simulation. An over-estimation existed for some of the physical properties, such as surface tension which was overestimated by 20 – 40 %. The author attributed this to the level of accuracy which was attainable in the assumed Lennard-Jones model. For studies based on noble gases this could be corrected by including terms which defined three-body interactions in the potential, and the authors postulated that the same could be true in this case. The study found that at 400 K both decane and eicosane had methyl groups preferentially exposed at the liquid vacuum, perpendicular to the liquid surface; while methylene groups lay parallel with the surface. This was surprising as both liquids melt at < 300 K and any long range ordering should be absent above this temperature.

Yamamoto and co-workers performed molecular dynamics simulations which simulated the surfaces of alkanes [92, 93]. The UA method was adopted but was simpler than that used by Harris [91]. In this case torsional motions and bond angles were neglected to use a simplified bead-spring system. The simulations involved observing the liquid behaviour on heating from a solid to a liquid. The authors observed a preferential melting in the bulk while the surface of the liquid remained frozen [93] at a temperature range around the melting point of the liquid (385 – 410 K [92]). This phenomenon has been independently documented by other groups [94, 95]. The phenomenon of surface freezing was also proposed as a possible explanation for reduced reactivity of linear hydrocarbons compared to branched hydrocarbons by McKendrick and co-workers [90]. These experiments were reminiscent of the

Yamamoto simulations [92, 93] where the liquids used experimentally were studied just above their melting points, making surface freezing a viable explanation for the trend in reactivity.

Siepmann and co-workers improved upon these earlier simulations by developing a TraPPE UA (transferable potential for phase equilibria united atom) force field with a Monte-Carlo (MC) simulation method to study the liquid vapour phase behaviour of squalane [96-98]. Initially ~ 200 squalane molecules were modelled like a layered crystal and subjected to thousands of MC cycles to define a melt system [96]. During the MC cycles each molecule undergoes a random set of functions such as translation, rotation and conformational change. This melt system was then cooled to the desired temperature and equilibrated by performing another 25000 – 100000 MC cycles [97] before analysis. The simulations agreed well with experimental properties measured such as boiling point, showing this model to be a good approximation of a branched liquid hydrocarbon surface.

A further study from the Siepmann group was targeted more towards modelling the interfacial structural properties of liquid squalane [98]. This study investigated the probability of finding each type of carbon group (CH, CH_2 or CH_3) at the gas-liquid interface. The results showed a very rough surface with no particular group appearing preferentially at its interface.

The McKendrick group performed MD simulations of their own relevant to the liquid squalane used in their experiment [99]. Using the Siepmann TraPPE method but expanding to contain more squalane molecules (288 compared to 96). In the MD simulations a tendency for CH_3 groups to protrude into the vacuum was noted at low temperatures which diminished as temperatures were increased. This was in contrast with the work of Siepmann and co-workers [98]. This coupled with an angular constraint on reactivity resulted in a modest preference for $O(^3P)$ atoms to impact with these primary atoms although all atom types were predicted to be accessible to incoming projectiles. The McKendrick group argue that the differences in results were due to the differing sizes of the simulations. The McKendrick group believed that the Siepmann group's results would match their own if scaled by the relative amounts of CH, CH_2 and CH_3 groups present.

1.5.2: Theoretical investigations into scattering from SAM surfaces

There are many examples of papers which are published on the topic of theoretical studies of scattering from SAM surfaces. This is because SAM surfaces are relatively easy to model based on their uniform structure. Indeed they are much easier to investigate theoretically than their liquid counterparts, explaining the relative lack of papers published on theoretical scattering from liquid surfaces.

1.5.3: Inelastic scattering from gas-SAM interfaces

Two main groups have been involved in the investigation of theoretical studies in this area. One of these is the Hase group who have completed a number of studies. They used a UA modelling system to investigate the dynamics of collisions of Ar with alkyl and OH terminated SAMs [34]. The results showed that energy transfer to the OH terminated SAM was less efficient than to the alkyl terminated SAM, this was consistent with previous experimental findings. These simulations showed an interesting result which was not observable experimentally. The group showed that Ar penetrated more effectively into the alkyl-terminated SAM, sometimes reaching the lowest carbon atom in the alkyl chain. The Ar atoms could then escape with a velocity dependent on the number of collisions experienced. The hydrogen-bonding network in the OH-terminated SAMs acted as a barrier to penetration but encouraged physisorption instead.

The second of these groups is the Troya group who published a study on the dynamics of collisions of Ar molecules with SAM surfaces of differing densities [32]. The method employed involved using a hybrid explicit to model the outer two carbons and united atom to model the remaining CH_2 atoms in the SAM chain. The hybrid explicit model treats each atom individually rather than in groups. The results of the study showed that less densely packed SAMs were more efficient at dissipating energy. This is in agreement with the experimental investigation of Morris and co-workers [30]. In addition to this finding, Troya and co-workers identified three distinct mechanisms which could occur on Ar atoms scattering from the SAM surface. The first of these was a direct (IS) method which involved the scatter of Ar atoms from the terminal CH_3 group in a single bounce collision. The second method was a TD method where the Ar atoms have undergone several collisions at the surface or interior of the SAM before

desorbing. The third mechanism was direct penetration where a single bounce collision occurred but below the terminal CH_3 group. These penetration Ar atoms were intermediate in energy between IS and TD scattered Ar atoms.

Troya and co-workers expanded their repertoire to study the collisions of CO with alkyl- and fluoro-terminated SAM surfaces [36, 37]. The simulations were to investigate energy transfer and stereodynamics during collision. The results showed that the CO transferred more energy to the alkyl SAM than the fluoro one. This effect was observed experimentally [37]. The simulations predicted an overall warming of scattered CO compared to pre-collision CO. The effect was more pronounced for fluoro-SAMs. This contradicts the work of Nesbitt and co-workers who observed warming of scattered CO_2 from PFPE and squalane which was found to be the same for each liquid [72]. Troya and co-workers speculate that this difference between alkyl and fluoro warming is due to the fluoro SAM surfaces being able to exert more of a torque on the scattered CO than the alkyl SAMs. Stereodynamically, Troya and co-workers found that a rotational orientation and alignment preference existed regardless of initial geometry. This preference was named “cartwheel topspin” and was strongest in the fluoro SAMs. The authors attributed this difference to increased corrugation in the alkyl SAM derivative.

The Hase and Nesbitt groups’ collaborative study on the dynamics of scattering of CO_2 molecules from a flouro terminated SAM surface [100] used both EA and UA models separately to simulate the SAM surface. The results of the study confirmed that more energy was transferred to the UA surface than the EA surface by around 10 %. This difference has been attributed to the UA surface overestimating important quantities such as energy transfer. The UA model is cheaper to run but is not as accurate as the EA model.

1.5.4: Reactive scattering from gas-SAM interfaces

Most of the studies completed in this area have focused on the reactions of $O(^3P)$ with various SAM surfaces. Investigations into this area have mainly focussed on the breaking of C-C bonds as a possible mechanism and how this may affect degradation of spacecraft in low Earth orbit, where high energy $O(^3P)$ species are abundant.

One of the earlier scattering simulations in this area were carried out by the Hase group who investigated the reactions of $O(^3P)$ molecules with an alkyl thiolate SAM surface [101]. Quantum mechanical/molecular mechanic modelling (QM/MM) was used to model the SAM surface, where the QM models the outer region of the SAM where most reaction would be expected to occur (usually 2-4 carbons) and the simpler MM model treats the inner portion of the SAM surface. PM3 calculations were used to model the $O(^3P)$ atoms. The simulations were able to predict both the direct and TD reaction mechanisms, with a modestly super-thermal temperature distribution for the direct products. The simulation also predicted that most OH products would occupy the ground vibrational state. Hase and co-workers also expanded this study to investigate the non-reactive collisions of the $O(^3P)$ atoms with a SAM surface [102].

The Schatz group published a paper on the reactive collisions of hyper-thermal (~5eV) $O(^3P)$ with hydrocarbon SAM surfaces [103]. They also used a QM/MM model to simulate the SAM surface, $O(^3P)$ reactants and OH products. The results showed some inelastic scattering was present but also that three reactive mechanisms were present. These were H abstraction, addition of $O(^3P)$ into the C-H bond resulting in H elimination and addition of $O(^3P)$ into the C-C bond resulting in C-C bond breakage.

The results suggested that OH formed would be vibrationally cold with only a small quantity present in the upper state. For H-abstraction, the direct reaction products were rotationally hot while the TD component was thermalized, but not completely as it was slightly hotter than the SAM surface temperature. This could be a result of the very high collision energies or the model overestimating rotational temperature. The model predicts that direct OH products will have rotational temperatures of around 3000 K. Experimentally, $O(^3P)$ temperatures have been observed to be around 370 K by McKendrick and co-workers [87]. This huge discrepancy may occur as a result of the large difference in collision energies. However, other studies using this type of low-level theoretical model to predict the potential have also been known to overestimate internal mode energy in product states when compared to experimental values, including studies on $O(^3P)$ reacting with methane and ethane [104, 105].

In a more recent study by Layfield and Troya, this issue seems at least to have been partially addressed with the simulation rotational temperatures more closely

resembling those of experiments [106]. The study involved the reactions of F atoms with alkylthiol SAM surfaces. The group compared a number of semi-empirical Hamiltonians eventually selecting the MSINDO (modified symmetrically orthogonalised intermediate neglect of differential overlap) Hamiltonian to model the SAM surface.

The model predicted that the HF products generated were vibrationally excited and super-thermal. It also predicted that the vibrational distribution was hotter than the rotational one. The predictions were consistent with experiments by the Nesbitt group on F + squalane [79]. Although the Nesbitt results were not on SAMs; the authors argue that the SAM and squalane surfaces will be relatively similar.

The use of theoretical investigations of scattering from SAM surfaces is a useful one. The models can identify different mechanisms of both reaction and inelastic scattering. These would be more difficult to observe experimentally. In the case of inelastic scattering, it may be almost impossible. For the studies to be most effective it is important for them to be conducted where a direct experimental comparison exists. This allows for iterative correction of parameters describing the potential, making the models more accurate.

1.5.5: Theoretical investigations into scattering from liquid surfaces

1.5.6: Inelastic scattering from gas-liquid interfaces

Presently, there have only been a few papers published on simulations of inelastic scattering from a true liquid surface. The Nathanson group have complemented their experimental work by completing an early simulation on collisions of Xe with liquid squalane [107]. The squalane surface was treated as a soft sphere. This model is obviously oversimplified and was used merely to investigate to what degree of accuracy simple models could qualitatively predict the observed scattering behaviour.

The model was accurate in predicting a bimodal product translational energy distribution but underestimated the trapping desorption component. The model did not predict energy transfer due to the lack of internal modes and their coupling to the collisions.

Much later, Hase and co-workers carried out classical chemical dynamics simulations of Ne scattering from a squalane surface [108]. The squalane molecules were modelled

using a UA approach, with realistic bond lengths and angles as well as stretching and torsional modes. The results showed that a bimodal energy distribution was present in scattered products. Thermalised products had undergone multiple collisions with the surface, having short residence times there. Neon atoms appeared to collide preferentially with methyl groups, although collisions with all groups were observed.

1.5.7: Reactive scattering from gas-liquid interfaces

Schatz and co-workers carried out the first simulations of the reaction of O(^{3}P) and F with a squalane surface [109, 110]. In these studies, the liquid squalane was defined with an explicit-atom force field (OPLS-EA). The hydrogen atoms had to be treated explicitly as they are involved in the reaction. The part of the liquid near the surface and therefore involved in reactions was treated with QM (in addition to the incoming and outgoing radicals) while the majority of the liquid was treated with MM. The boundary between the two could be adjusted during simulation. Schatz and co-workers simulated high energy O(^{3}P) atoms (1 – 5 eV) as this correlated with the energies of O(^{3}P) atoms in LEO as well as complementing the experiments of the Minton group [84].

The results of this study showed that H-abstraction was the dominant reaction mechanism but that H-elimination and C-C bond breakage also occurred. These results all agree well with experiment except that the H-elimination channel was not observed experimentally, however it was thought to still be present, as discussed in the complimentary experimental paper [84].

The simulation predicted both IS and TD type encounters but it also showed that IS single-bounce products may sometimes travel slowly while TD, several-bounce encounters may travel relatively fast as well as slow. This may be a due to the degree of accuracy present within the simulation or may just reflect that the IS and TD mechanisms are more complex than first thought and may not be easily separable.

1.6: Summary

This chapter has reviewed a portion of the field of scattering dynamics from liquids and related interfaces such as SAM surfaces as well as provided a brief snapshot of the gas-phase experiments relevant to the new results presented in this thesis. There have been a number of experimental studies conducted on both SAM and liquid surfaces for both inelastic and reactive scattering. The theoretical studies completed are much smaller in number and have been variable in the accuracy of their predictions.

The work presented in this thesis aims to further study this area by exploring either completely new systems or further the understanding of previously investigated ones. These topics include the first instance of scattering of the excited state of oxygen $O(^1D)$ from a liquid surface, investigation of a rotationally and translationally hot source of OH to further understanding of the scattering dynamics of OH from saturated and unsaturated hydrocarbon surfaces and the investigation of scattering of $O(^3P)$ from saturated and unsaturated surfaces.

1.7: References

1. J. M. Zhang, D. J. Garton and T. K. Minton, *J. Chem. Phys.*, 2002, **117**, 6239-6251.
2. G. B. Ellison, A. F. Tuck and V. Vaida, *Journal of Geophysical Research-Atmospheres*, 1999, **104**, 11633-11641.
3. I. P. C. C., *Climate Change Report 2013*, WMO and UNEP, 2013.
4. D. Rosenfeld, *Science*, 2006, **312**, 1323-1324.
5. I. J. Wysong, J. B. Jeffries and D. R. Crosley, *J. Chem. Phys.*, 1991, **94**, 7547-7549.
6. K. Schreel, J. Schleipen, A. Eppink and J. J. Ter Meulen, *J. Chem. Phys.*, 1993, **99**, 8713-8722.
7. K. Schreel and J. J. ter Meulen, *J. Chem. Phys.*, 1996, **105**, 4522-4532.
8. M. C. van Beek, K. Schreel and J. J. ter Meulen, *J. Chem. Phys.*, 1998, **109**, 1302-1309.
9. D. A. V. Kliner and R. L. Farrow, *J. Chem. Phys.*, 1999, **110**, 412-422.
10. D. J. Garton, T. K. Minton, B. Maiti, D. Troya and G. C. Schatz, *J. Chem. Phys.*, 2003, **118**, 1585-1588.
11. D. J. Garton, A. L. Brunsvold, T. K. Minton, D. Troya, B. Maiti and G. C. Schatz, *J. Phys. Chem. A*, 2006, **110**, 1327-1341.
12. A. L. Brunsvold, H. P. Upadhyaya, J. Zhang, R. Cooper and T. K. Minton, *J. Phys. Chem. A*, 2008, **112**, 2192-2205.
13. J. M. Zhang, S. A. Lahankar, D. J. Garton, T. K. Minton, W. Q. Zhang and X. M. Yang, *J. Phys. Chem. A*, 2011, **115**, 10894-10902.
14. D. J. Garton, T. K. Minton, W. F. Hu and G. C. Schatz, *J. Phys. Chem. A*, 2009, **113**, 4722-4738.
15. P. Andresen and A. C. Luntz, *J. Chem. Phys.*, 1980, **72**, 5842-5850.
16. J. C. Whitehead and F. Winterbottom, *Chem. Phys. Lett.*, 1991, **177**, 207-212.
17. F. Ausfelder and K. G. McKendrick, *Prog. React. Kinet. Mech.*, 2000, **25**, 299-370.
18. N. Camillone, C. E. D. Chidsey, P. Eisenberger, P. Fenter, J. Li, K. S. Liang, G. Y. Liu and G. Scoles, *J. Chem. Phys.*, 1993, **99**, 744-747.
19. D. P. Fogarty and S. A. Kandel, *J. Chem. Phys.*, 2006, **124**, 111101.
20. N. A. Kautz and S. A. Kandel, *J. Am. Chem. Soc.*, 2008, **130**, 6908-6909.
21. Y. Wang, Q. J. Chi, N. S. Hush, J. R. Reimers, J. D. Zhang and J. Ulstrup, *J. Phys. Chem. C*, 2011, **115**, 10630-10639.
22. S. R. Cohen, R. Naaman and J. Sagiv, *Phys. Rev. Lett.*, 1987, **58**, 1208-1211.
23. K. D. Gibson, N. Isa and S. J. Sibener, *J. Chem. Phys.*, 2003, **119**, 13083-13095.
24. N. Isa, K. D. Gibson, T. Yan, W. Hase and S. J. Sibener, *J. Chem. Phys.*, 2004, **120**, 2417-2433.
25. K. D. Gibson, N. Isa and S. J. Sibener, *J. Phys. Chem. A*, 2006, **110**, 1469-1477.
26. B. S. Day, G. M. Davis and J. R. Morris, *Anal. Chim. Acta*, 2003, **496**, 249-258.
27. B. S. Day and J. R. Morris, *J. Phys. Chem. B*, 2003, **107**, 7120-7125.
28. B. S. Day, S. F. Shuler, A. Ducre and J. R. Morris, *J. Chem. Phys.*, 2003, **119**, 8084-8096.
29. J. R. Lohr, B. S. Day and J. R. Morris, *J. Phys. Chem. B*, 2005, **109**, 15469-15475.
30. B. S. Day and J. R. Morris, *J. Chem. Phys.*, 2005, **122**, 234714.
31. J. R. Lohr, B. S. Day and J. R. Morris, *J. Phys. Chem. A*, 2006, **110**, 1645-1649.
32. B. S. Day, J. R. Morris, W. A. Alexander and D. Troya, *J. Phys. Chem. A*, 2006, **110**, 1319-1326.
33. S. A. Vazquez, J. R. Morris, A. Rahaman, O. A. Mazyar, G. Vayner, S. V. Addepalli, W. L. Hase and E. Martinez-Nunez, *J. Phys. Chem. A*, 2007, **111**, 12785-12794.
34. U. Tasic, B. S. Day, T. Yan, J. R. Morris and W. L. Hase, *J. Phys. Chem. C*, 2008, **112**, 476-490.
35. M. E. Bennett, W. A. Alexander, J. W. Lu, D. Troya and J. R. Morris, *J. Phys. Chem. C*, 2008, **112**, 17272-17280.
36. W. A. Alexander, J. R. Morris and D. Troya, *J. Phys. Chem. A*, 2009, **113**, 4155-4167.
37. W. A. Alexander, J. R. Morris and D. Troya, *J. Chem. Phys.*, 2009, **130**, 084702.

38. J. W. Lu, W. A. Alexander and J. R. Morris, *Phys. Chem. Chem. Phys.*, 2010, **12**, 12533-12543.
39. J. W. Lu and J. R. Morris, *J. Phys. Chem. A*, 2011, **115**, 6194-6201.
40. J. Gorham, B. Smith and D. H. Fairbrother, *J. Phys. Chem. C*, 2007, **111**, 374-382.
41. J. M. Gorham, A. K. Stover and D. H. Fairbrother, *J. Phys. Chem. C*, 2007, **111**, 18663-18671.
42. Y. Dubowski, J. Vieceli, D. J. Tobias, A. Gomez, A. Lin, S. A. Nizkorodov, T. M. McIntire and B. J. Finlayson-Pitts, *J. Phys. Chem. A*, 2004, **108**, 10473-10485.
43. T. M. McIntire, A. S. Lea, D. J. Gaspar, N. Jaitly, Y. Dubowski, Q. Q. Li and B. J. Finlayson-Pitts, *Phys. Chem. Chem. Phys.*, 2005, **7**, 3605-3609.
44. T. M. McIntire, O. Ryder and B. J. Finlayson-Pitts, *J. Phys. Chem. C*, 2009, **113**, 11060-11065.
45. B. J. Finlayson-Pitts, *Phys. Chem. Chem. Phys.*, 2009, **11**, 7760-7779.
46. X. Qin, T. Tzvetkov and D. C. Jacobs, *Nucl. Instrum. Methods Phys. Res. Sect. B-Beam Interact. Mater. Atoms*, 2003, **203**, 130-135.
47. X. D. Qin, T. Tzvetkov, X. Liu, D. C. Lee, L. P. Yu and D. C. Jacobs, *J. Am. Chem. Soc.*, 2004, **126**, 13232-13233.
48. X. D. Qin, T. Tzvetkov and D. C. Jacobs, *J. Phys. Chem. A*, 2006, **110**, 1408-1415.
49. Y. Paz, S. Trakhtenberg and R. Naaman, *J. Phys. Chem.*, 1992, **96**, 10964-10967.
50. Y. Paz, S. Trakhtenberg and R. Naaman, *J. Phys. Chem.*, 1994, **98**, 13517-13523.
51. C. Waring, P. A. J. Bagot, M. T. Raisanen, M. L. Costen and K. G. McKendrick, *J. Phys. Chem. A*, 2009, **113**, 4320-4329.
52. C. Waring, P. A. J. Bagot, M. W. P. Bebbington, M. T. Raisanen, M. Buck, M. L. Costen and K. G. McKendrick, *J. Phys. Chem. Letts.*, 2010, **1**, 1917-1921.
53. J. Torres, C. C. Perry, S. J. Bransfield and D. H. Fairbrother, *J. Phys. Chem. B*, 2002, **106**, 6265-6272.
54. A. J. Wagner, G. M. Wolfe and D. H. Fairbrother, *J. Chem. Phys.*, 2004, **120**, 3799-3810.
55. A. K. Bertram, A. V. Ivanov, M. Hunter, L. T. Molina and M. J. Molina, *J. Phys. Chem. A*, 2001, **105**, 9415-9421.
56. S. G. Moussa and B. J. Finlayson-Pitts, *Phys. Chem. Chem. Phys.*, 2010, **12**, 9419-9428.
57. A. J. Kenyon, A. J. McCaffery, C. M. Quintella and M. D. Zidan, *Journal of the Chemical Society-Faraday Transactions*, 1993, **89**, 3877-3884.
58. A. J. Kenyon, A. J. McCaffery, C. M. Quintella and M. D. Zidan, *Faraday Discuss.*, 1993, **96**, 245-254.
59. M. E. Saecker, S. T. Govoni, D. V. Kowalski, M. E. King and G. M. Nathanson, *Science*, 1991, **252**, 1421-1424.
60. M. E. King, G. M. Nathanson, M. A. Hanninglee and T. K. Minton, *Phys. Rev. Lett.*, 1993, **70**, 1026-1029.
61. M. E. Saecker and G. M. Nathanson, *J. Chem. Phys.*, 1993, **99**, 7056-7075.
62. M. E. King, M. E. Saecker and G. M. Nathanson, *J. Chem. Phys.*, 1994, **101**, 2539-2547.
63. W. R. Ronk, D. V. Kowalski, M. Manning and G. M. Nathanson, *J. Chem. Phys.*, 1996, **104**, 4842-4849.
64. G. M. Nathanson, P. Davidovits, D. R. Worsnop and C. E. Kolb, *J. Phys. Chem.*, 1996, **100**, 13007-13020.
65. M. E. King, K. M. Fiehrer, G. M. Nathanson and T. K. Minton, *J. Phys. Chem. A*, 1997, **101**, 6556-6561.
66. J. K. Klassen, K. M. Fiehrer and G. M. Nathanson, *J. Phys. Chem. B*, 1997, **101**, 9098-9106.
67. G. M. Nathanson, *Annu. Rev. Phys. Chem.*, 2004, **55**, 231-255.
68. A. H. Muenter, J. L. DeZwaan and G. M. Nathanson, *J. Phys. Chem. B*, 2006, **110**, 4881-4891.
69. B. G. Perkins, T. Haber and D. J. Nesbitt, *J. Phys. Chem. B*, 2005, **109**, 16396-16405.
70. B. G. Perkins and D. J. Nesbitt, *J. Phys. Chem. B*, 2008, **112**, 507-519.

71. B. G. Perkins and D. J. Nesbitt, *J. Phys. Chem. A*, 2010, **114**, 1398-1410.
72. B. G. Perkins and D. J. Nesbitt, *J. Phys. Chem. B*, 2006, **110**, 17126-17137.
73. D. A. Jaeger and M. D. Ward, *J. Org. Chem.*, 1982, **47**, 2223-2225.
74. G. M. Sweeney, A. Watson and K. G. McKendrick, *J. Chem. Phys.*, 1997, **106**, 9172-9181.
75. F. Ausfelder, H. Kelso and K. G. McKendrick, *Phys. Chem. Chem. Phys.*, 2002, **4**, 473-481.
76. H. Tsurumaki, Y. Fujimura and O. Kajimoto, *J. Chem. Phys.*, 2000, **112**, 8338-8346.
77. X. H. Liu, R. L. Gross and A. G. Suits, *J. Chem. Phys.*, 2002, **116**, 5341-5344.
78. X. H. Liu, R. L. Gross, G. E. Hall, J. T. Muckerman and A. G. Suits, *J. Chem. Phys.*, 2002, **117**, 7947-7959.
79. A. M. Zolot, W. W. Harper, B. G. Perkins, P. J. Dagdigian and D. J. Nesbitt, *J. Chem. Phys.*, 2006, **125**, 021101.
80. A. M. Zolot, P. J. Dagdigian and D. J. Nesbitt, *J. Chem. Phys.*, 2008, **129**, 194705.
81. D. J. Garton, T. K. Minton, M. Alagia, N. Balucani, P. Casavecchia and G. G. Volpi, *Faraday Discuss.*, 1997, **108**, 387-399.
82. D. J. Garton, T. K. Minton, M. Alagia, N. Balucani, P. Casavecchia and G. G. Volpi, *J. Chem. Phys.*, 2000, **112**, 5975-5984.
83. D. J. Garton, T. K. Minton, D. Troya, R. Pascual and G. C. Schatz, *J. Phys. Chem. A*, 2003, **107**, 4583-4587.
84. J. M. Zhang, H. P. Upadhyaya, A. L. Brunsvold and T. K. Minton, *J. Phys. Chem. B*, 2006, **110**, 12500-12511.
85. H. Kelso, S. P. K. Kohler, D. A. Henderson and K. G. McKendrick, *J. Chem. Phys.*, 2003, **119**, 9985-9988.
86. S. P. K. Kohler, M. Allan, H. Kelso, D. A. Henderson and K. G. McKendrick, *J. Chem. Phys.*, 2005, **122**, 024712.
87. S. P. K. Kohler, M. Allan, M. L. Costen and K. G. McKendrick, *J. Phys. Chem. B*, 2006, **110**, 2771-2776.
88. M. Allan, P. A. J. Bagot, S. P. K. Kohler, S. K. Reed, R. E. Westacott, M. L. Costen and K. G. McKendrick, *Phys. Scr.*, 2007, **76**, C42-C47.
89. M. Allan, P. A. J. Bagot, M. L. Costen and K. G. McKendrick, *J. Phys. Chem. C*, 2007, **111**, 14833-14842.
90. M. Allan, P. A. J. Bagot, R. E. Westacott, M. L. Costen and K. G. McKendrick, *J. Phys. Chem. C*, 2008, **112**, 1524-1532.
91. J. G. Harris, *J. Phys. Chem.*, 1992, **96**, 5077-5086.
92. T. Shimizu and T. Yamamoto, *J. Chem. Phys.*, 2000, **113**, 3351-3359.
93. H. Z. Li and T. Yamamoto, *J. Chem. Phys.*, 2001, **114**, 5774-5780.
94. E. Sloutskin, X. Z. Wu, T. B. Peterson, O. Gang, B. M. Ocko, E. B. Sirota and M. Deutsch, *Physical Review E*, 2003, **68**.
95. Y. Zhang, Z. C. Ou-Yang and M. Iwamoto, *J. Chem. Phys.*, 2006, **124**.
96. N. D. Zhuravlev and J. I. Siepmann, *Fluid Phase Equilib.*, 1997, **134**, 55-61.
97. N. D. Zhuravlev, M. G. Martin and J. I. Siepmann, *Fluid Phase Equilib.*, 2002, **202**, 307-324.
98. C. D. Wick, J. I. Siepmann and M. R. Schure, *Anal. Chem.*, 2002, **74**, 3518-3524.
99. S. P. K. Kohler, S. K. Reed, R. E. Westacott and K. G. McKendrick, *J. Phys. Chem. B*, 2006, **110**, 11717-11724.
100. J. J. Nogueira, S. A. Vazquez, O. A. Mazyar, W. L. Hase, B. G. Perkins, D. J. Nesbitt and E. Martinez-Nunez, *J. Phys. Chem. A*, 2009, **113**, 3850-3865.
101. G. Li, S. B. M. Bosio and W. L. Hase, *J. Mol. Struct.*, 2000, **556**, 43-57.
102. U. S. Tasic, T. Y. Yan and W. L. Hase, *J. Phys. Chem. B*, 2006, **110**, 11863-11877.
103. D. Troya and G. C. Schatz, *J. Chem. Phys.*, 2004, **120**, 7696-7707.
104. D. Troya, R. Z. Pascual, D. J. Garton, T. K. Minton and G. C. Schatz, *J. Phys. Chem. A*, 2003, **107**, 7161-7169.

105. D. Troya, R. Z. Pascual and G. C. Schatz, *J. Phys. Chem. A*, 2003, **107**, 10497-10506.
106. J. P. Layfield and D. Troya, *J. Chem. Phys.*, 2010, **132**, 134307.
107. N. Lipkin, R. B. Gerber, N. Moiseyev and G. M. Nathanson, *J. Chem. Phys.*, 1994, **100**, 8408-8417.
108. Y. X. Peng, L. Liu, Z. Cao, S. Li, O. A. Mazyar, W. L. Hase and T. Y. Yan, *J. Phys. Chem. C*, 2008, **112**, 20340-20346.
109. D. Kim and G. C. Schatz, *J. Phys. Chem. A*, 2007, **111**, 5019-5031.
110. B. K. Radak, S. Yockel, D. Kim and G. C. Schatz, *J. Phys. Chem. A*, 2009, **113**, 7218-7226.

Chapter 2 - Experimental

This chapter contains information about the instrumentation and experimental techniques used to study the gas-liquid interactions described in subsequent chapters. This work builds on the foundations of that begun by McKendrick and co-workers [1-17] which was first used to study the reaction of $O(^3P)$ molecules with various liquid hydrocarbons.

2.1: Introduction to Laser-induced fluorescence (LIF)

In all the measurements presented here, products of heterogeneous gas-liquid interactions are studied by laser-induced fluorescence (LIF). The LIF technique was first developed by Zare and co-workers [18] and has since been adopted for many applications such as monitoring atomic and molecular reaction products [19].

For a molecule to be detected by LIF, there are basic requirements: the molecule must have an electronic absorption band in a wavelength range which can be reached by tuneable lasers; the fluorescence quantum yield must be non-zero; and the basic spectroscopic and radiative properties of the molecule must have been previously characterised.

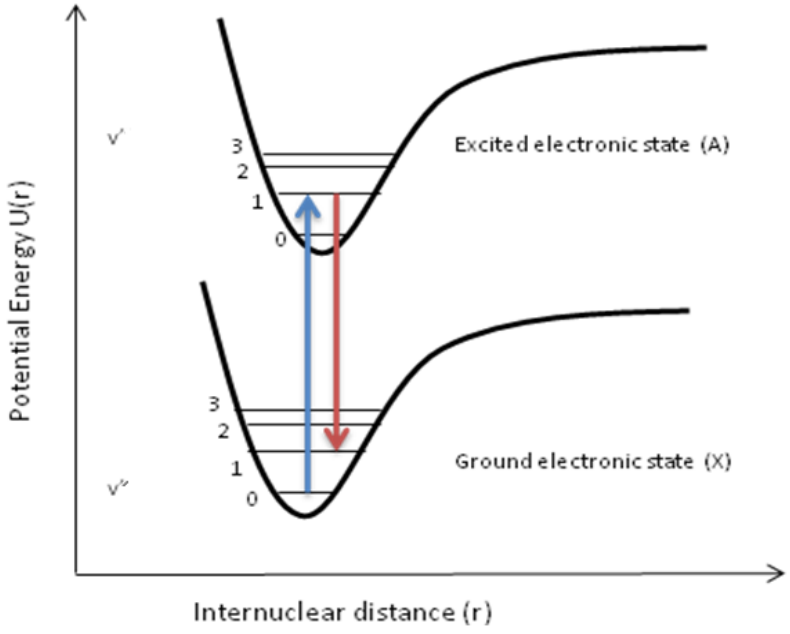

Figure 2.1: Potential energy diagram of a general diatomic molecule showing a basic LIF schematic for an off-diagonal transition. Absorption on the (1,0) band is shown in blue and fluorescence on the (1,1) band is shown in red.

The basic LIF technique involves using a probe laser system. This probe laser is a tuneable laser which can scan across the electronic absorption band. At specific wavelengths during this scan, the laser light will be resonant with a rovibronic transition which means that a small quantity of the molecule of interest will be excited from a ground state to a specific rotational-vibrational level in the upper state. From this upper state spontaneous fluorescence photons are emitted. A specific example of this is illustrated in figure 2.1. For OH absorbance on the (1,0) band occurs at 280 – 286 nm while emission (on the (1,1) band) occurs at 312 – 318 nm. An interference filter with peak absorbance at 315 nm blocks the emission fluorescence. The result is an 'excitation spectrum' of fluorescence intensity which varies with probe wavelength. This is comparable to an absorption spectrum but has the added benefit of a 'dark' or zero background. Information on the internal state distribution of the products can be extracted from this spectrum for the species present in the probe volume.

2.2: The wheel assembly

All experiments presented in this thesis were performed at a continually refreshed liquid surface. This was generated by using a stainless steel wheel which rotated at 0.5 revolutions Hz in a bath of the liquid to ensure even coverage. The use of a rotating wheel was first introduced by Lednovich and Fenn [20] and is central to the experimental set-up.

The liquid under study is placed in a specially manufactured copper bath. This is shown in figure 2.2. Around 5 mL of the liquid is used to fill the bath to three quarters of its total volume. The 5 cm diameter stainless steel wheel is then partially immersed in the liquid and powered by an external motor which rotates the wheel to produce the liquid surface. In practice, there were three identical copper baths which were interchangeable. This enabled each bath to be assigned to a particular liquid which minimised both turnover time between changing liquids and chance of contamination.

It was also possible to vary the liquid temperature by circulating heated water through channels in the copper bath assembly, but all experiments detailed here were performed at room temperature.

The wheel assembly has been designed so that the distance between the laser axes and the liquid surface can be varied to allow optimum conditions to be selected for each experiment. This allows the distance to be set for each set of experiments and adjusted when necessary without removing the whole assembly.

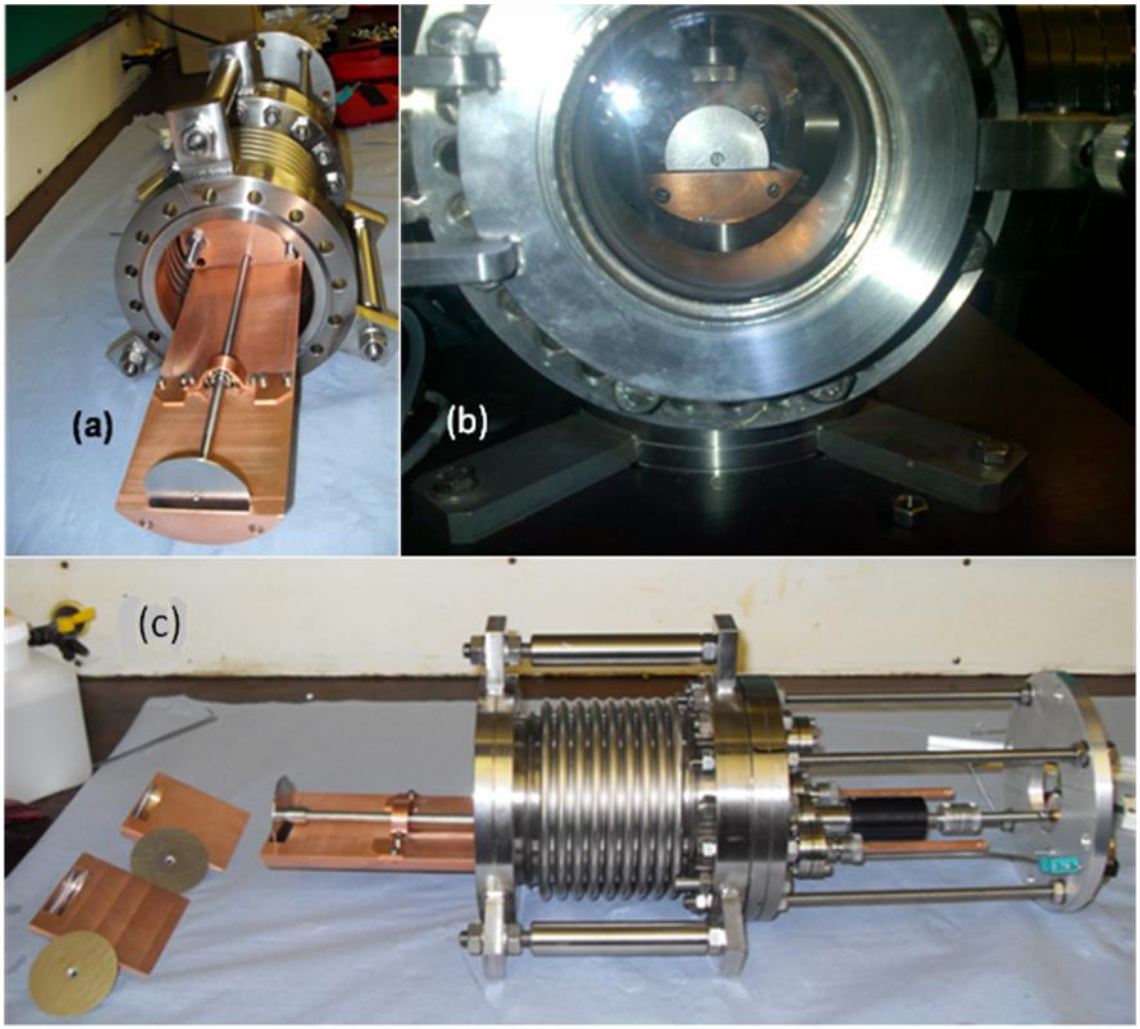

Figure 2.2: The wheel assembly shown from the front (a) and from the side (c). In photograph (c) the axle and external motor can be clearly seen. Photograph (b) shows the wheel in place in the chamber.

2.3: Vacuum system

The wheel assembly was housed in a stainless steel vacuum chamber (Vacuum Generators) with a total volume of ~12 L. The chamber was a six-way cross containing six 10 cm ports. Two of the ports were fitted with elongated arms terminated by fused silica (Spectrosil 2000) windows of 100 mm diameter, 5 mm thickness and λ\4 flatness

(Apex services Ltd). The other two horizontal ports contained the wheel assembly and a viewing port. The vertical ports contained a liquid light guide for detecting fluorescence – this is explained in more detail in section 2.8.1 - and the vacuum pumps for reducing pressure.

The pumping system used varied slightly in each set of experiments. In all cases a rotary pump (Edwards RV8) was used to reduce the pressure in the main chamber to around 1 x 10^{-3} mbar. For the studies using O(^{3}P) (Chapter 6) and O(^{1}D) (Chapter 4) a turbo-molecular pump (Edwards EXT 70) was used to further reduce the pressure to the order of 1 x 10^{-6} mbar. This turbo-molecular pump was backed with another rotary pump (Edwards RV8). In the OH from allyl alcohol study (Chapter 5) only one rotary pump was used in combination with a diffusion pump (Edwards 100/300 M (B34637978)) to achieve the desired pressure of around 1 x 10^{-6} mbar. To measure the pressure in the main chamber in all experiments both a wide-range gauge (Edwards WRG-5145-36UZW) and a Baratron gauge (BOC Edwards 655AB) were used. An additional active Pirani gauge (Edwards APG-L-NW16) was used to monitor the pressure at the entrance to the rotary pump. In the O(^{3}P) study (Chapter 6) and the O(^{1}D) study (Chapter 4) a further convection gauge (Kurt J Lesker 275i) was used to monitor the additional rotary pump.

2.4: Precursors

The potentially reactive species in all experiments was formed by photolysis of a chosen precursor. Many factors come into account when selecting a suitable precursor. Photolytic quantum yields must be reasonably high and a large absorption cross section in the wavelength range of commercially available lasers is also necessary. Further desirable properties include a well-characterised photolytic distribution (such as internal and translational energy), ready availability and a low cost. A summary of the precursors used in this study is given in table 2.1.

Precursor Gas	Reactive species	Photolysis Wavelength (nm)	Absorption cross section (σ /cm^2)	Source
allyl alcohol	OH	193	8 x 10^{-19} [21]	Sigma-Aldrich ≥ 99% purity
N_2O	O(^{1}D)	193	9 x 10^{-20} [22]	BOC ≥ 98% purity
NO_2	O(^{3}P)	355	5 x 10^{-19} [23]	BOC ≥ 98% purity

Table 2.1: Summary of precursors used in experiments

2.4.1 – Single collision conditions

In all experiments the pressure of precursor admitted to the chamber was deliberately low (~1 mTorr) to ensure that all experiments are carried out under single collision (nascent) conditions. This means that most of the molecules detected will have only encountered the surface and not suffered any secondary gas-phase collisions. Which is important in determining the collisional dynamics of the interaction as in cases where secondary encounters occur, the information of the first encounter with the surface is lost. If the majority of molecules have more than one encounter then it is impossible to glean any dynamical information as the system becomes collisionally thermalised.

The average number of collisions per molecule in the gas phase under thermal conditions can be estimated using a typical gas-kinetic collision rate constant of 1 x 10^7 collisions $Torr^{-1}$ s^{-1}. If an average pressure of 1 mTorr and an average delay of 12 µs is used then the typical number of collisions is 0.12. This number is sufficiently low to believe that most of the products detected were from single collisions with the surface only.

One drawback of this method of calculating collisions is that the gas kinetic collisional rate assumes that the products of photolysis have thermal velocity distributions, which is not always the case. We can use another method which does not assume this to confirm the safe working pressure limit. This involves calculating the mean free path, which corresponds to the average distance travelled between collisions. The mean free

path (λ) is calculated from a combination of equations 2.1 and 2.2, treating both species (NO_2 and OH in the following example) as hard spheres. For the purposes of this calculation, OH has an assumed radius of 0.48 Å [24] and NO_2 has a radius of 1.46 Å [25]. These are used to calculate the collisional cross section (equation 2.1) σ, for the typical case of NO_2 being the precursor and OH the product (more detailed in Chapter 6). In this case σ is 1.18 x 10^{-19} m^2. At a pressure of 1 mTorr, this implies that the mean free path is ~19 cm. In comparison, the typical average minimum distance travelled by a molecule is ~1.8 cm which is the distance to the wheel and back with a 9 mm laser-axes-to-wheel distance. Due to the large difference between the mean free path and the distance travelled, it is again likely that only single collisions at the liquid surface are significant.

$$\sigma = \pi(r_1 + r_2)^2$$ - Equation 2.1

$$\lambda = \frac{k_B T}{\sqrt{2}\sigma P}$$ - Equation 2.2

In fact when analysing scattered species, all those present after 30 μs are discounted to ensure that the single-collision condition is enforced. Empirical measurements show that profiles are indistinguishable to those recorded at lower pressures up to around this delay of 30 μs. This type of investigation was carried out by McKendrick and co-workers [12].

For each reactive species studied and hence precursor selected, a different process occurred during photolysis. These are listed below for allyl alcohol, N_2O and NO_2 in equations 2.3, 2.4 and 2.5.

$CH_2CHCH_2OH + h\nu\ (193\ nm) \rightarrow CH_2CHCH_2\cdot + OH\cdot$ Equation 2.3

$N_2O + h\nu\ (193\ nm) \rightarrow N_2 + O(^1D)$ Equation 2.4

$NO_2 + h\nu\ (355\ nm) \rightarrow NO + O(^3P)$ Equation 2.5

2.5: Liquid properties and structure

It is possible to use many different types of liquids with this experimental set-up as long as they have a reasonable melting point and a suitably low vapour pressure. Only three main liquids were used in the work presented in this thesis. PFPE (perfluoropolyether, (Krytox 1506) was used as a reference as it contains no hydrogen, therefore no H-abstraction (or competing addition) reactions can take place with the reactive species of interest. Squalane (2,6,10,15,19,23-hexamethyltetradodecane) and squalene (2,6,10,15,19,23–hexamethyltetracosa-2,6,10,14,18,22-hexaene) were used as potentially reactive liquids. They were chosen as they can both be considered as proxies for atmospheric aerosols and therefore can be used as a pseudo-representative of the differences between saturated and unsaturated species in the atmosphere. Table 2.2 includes a summary the relevant properties of the three liquids studied while figure 2.3 shows the structures.

Liquid	Source	Purity /%	Chemical Formula	Vapour Pressure / Torr @ 298 K	Melting point / K
PFPE	DuPont	-	F-[CF(CF_3)-CF_2O]-CF_2CF_3	~ 1 x 10^{-7}	213 (pour point)
Squalane	Sigma-Aldrich	≥ 99	$C_{30}H_{62}$	~ 1 x 10^{-7}	235
Squalene	Sigma-Aldrich	≥ 98	$C_{30}H_{50}$	~ 1 x 10^{-7}	198

Table 2.2: Summary of the relevant properties of the three liquids used across all studies.

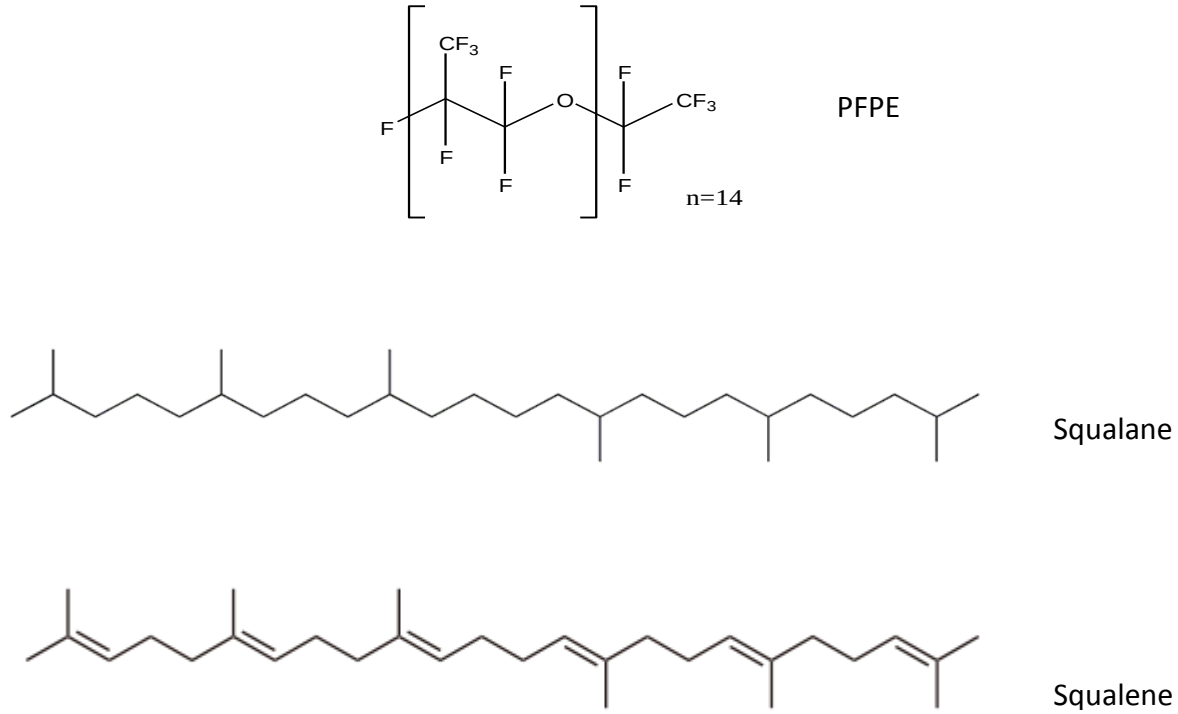

Figure 2.3: Chemical structures of the three liquids studied.

2.6: Optical system - Photolysis lasers

The precursors were summarised in table 2.1. As can be seen from this, two different photolysis wavelengths were used in the photolysis of these three species. Correspondingly, two different photolysis lasers were used. As indicated in the experimental schematic in figure 2.4, these were either an ArF excimer laser (GAM EX350) at 193 nm or the third harmonic of a Nd:YAG (Continuum Surelight SL-II- 10) at 355 nm.

2.6.1- Excimer laser

The excimer laser was used in two studies in the course of this work: the OH study (Chapter 5) and the $O(^1D)$ study (Chapter 4). In both cases the photolysis wavelength used was 193 nm. This was achieved by using a pre-mixed gas cylinder to generate ArF during discharge (Spectra Gases).This mixture consists of 0.17 % F_2, 6.0 % Argon, 1 % Helium, 10 ppm Xe, 15 ppm O_2, and finally Neon to make the pressure up to 2375 Torr.

The laser was triggered by a four channel delay and pulse generator (Stanford research systems, DG535) and the repetition rate was set to 10 Hz. The excimer laser was set to run in constant energy mode and typically produced an un-polarised pulse of 2-5 ns long with average energy of ~100 mJ pulse^{-1}. In cases where the energy dropped and the laser began to miss shots, the thyratron reservoir voltage could be increased to alleviate this problem. The excimer laser beam was collimated through a series of lenses to reduce it to an approximately rectangular 4 mm by 2 mm spot-size, with the longer axis being vertical in the laboratory frame. The energies at the centre of the chamber were typically 70 mJ per pulse^{-1}.

2.6.2 - Nd:YAG laser

To generate the desired wavelength of 355 nm, the third harmonic output of the Nd:YAG laser was employed. This was achieved by sum-frequency mixing of the fundamental wavelength (1064 nm) and the frequency doubled second harmonic (532 nm) in a KDP crystal. The flashlamp was triggered externally using the same delay and pulse generator as for the excimer laser. The Q-Switch trigger pulse was typically sent 170 μs after the flashlamp pulse to optimise energy output. Again, the laser was run at a repetition rate of 10 Hz and produced horizontally polarised 355 nm pulses of length 5-6 ns with a resulting energy of ~ 100 mJ pulse^{-1}.

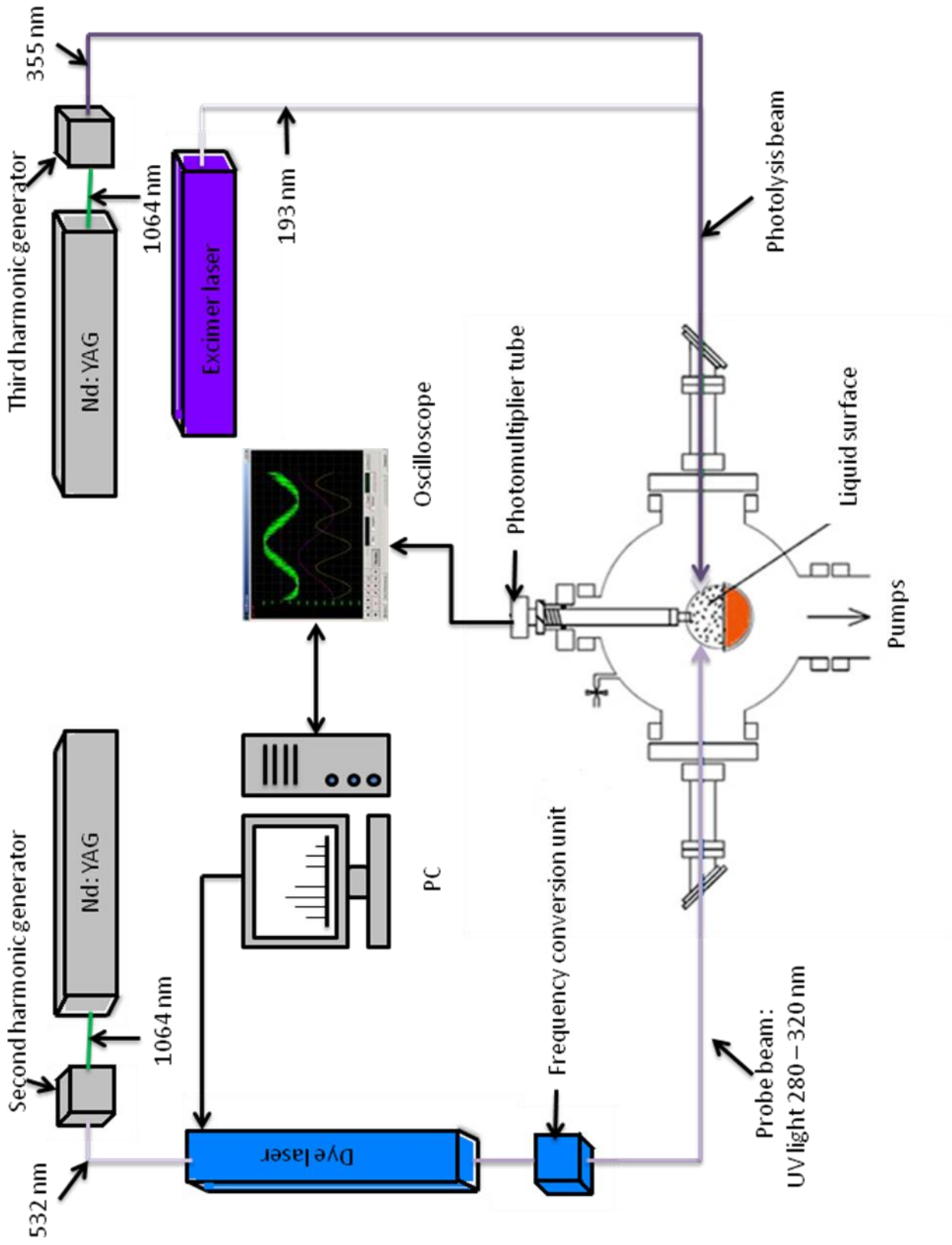

Figure 2.4: Schematic of the experimental set-up.

The beam size was reduced by an iris to form a circular beam with a diameter of 5 mm which resulted in energies of the order of 90 mJ pulse^{-1} in the centre of the chamber. In the cases of both lasers, they were admitted to the chamber through the fused silica windows (discussed in section 2.3.). These windows were set to Brewster's angle to minimise reflection at the entry window. Scattered light from the photolysis beam was reduced by a series of black – painted stainless-steel baffles with a central diameter of 5 – 7.5 mm placed in the elongated arm at the photolysis side of the reaction chamber.

2.6.3- Anisotropy considerations in the Nd:YAG laser

In the gas-phase at thermal equilibrium, molecules are randomly oriented which means that they have an isotropic distribution of rotation or molecular axes. When irradiated with light from a laser source, the electrons in a bond can move either along the transition dipole or perpendicular to it [26]. As the transition dipole moment can only be present along the axis of symmetry of the molecule or directly perpendicular to it, the resulting recoil of photo-fragments is anisotropic. The best case for optical absorption occurs when the transition dipole moment is aligned with the electric vector of the light. Therefore when using linear polarisation, either horizontal or vertical polarisation can be selected, as appropriate to the precursor and wavelength, to ensure that the majority of fragments recoil in the desired direction. The extent of recoil anisotropy is defined by the anisotropy parameter, β, which is defined via equation 2.6. Here, P_2 is the second-order Legendre polynomial (expanded in equation 2.7) and θ is the angle between the recoil direction of the photofragments and the electric vector of the light. It is important to note that these cases only apply when the Nd:YAG laser is used as a source for photolysis as the excimer laser is un-polarised which means the fraction of generated species travelling towards the liquid wheel cannot be optimised. It is important to note that while the excimer laser is unpolarised, it will still produce an anisotropic distribution of photofragments due to the non-zero value of the beta parameter for N_2O and allyl alcohol. There will be equal numbers of fragments recoiling in all directions perpendicular to the propagation direction of the electric light vector but these numbers will not be the same as the fragments produced along the propagation direction of the electric light vector.

$$I(\theta) = \frac{[1 + \beta P_2(\cos\theta)]}{4\pi}$$ Equation 2.6

$$P_2(\cos\theta) = \frac{(3\cos^2\theta - 1)}{2}$$ Equation 2.7

The most favourable experimental conditions occur when β is equal to either of its limits which are +2 or -1 respectively. When β = +2, the intensity for a given θ is proportional to $\cos^2\theta$ and is an example of a parallel transition. The opposite occurs when θ = -1 as the intensity is proportional to $\sin^2\theta$ and is an example of a perpendicular transition. A value of 0 corresponds to an isotropic distribution which means that neither linear polarisation is more favourable. The limiting β = +2 case is shown in figure 2.5 along with the opposing case of vertical polarisation where β = -1 in the laboratory frame which was not used in any of the studies presented here, it is merely included for reference.

The only study in which this information was used was used directly was the study on $O(^3P)$ generated from NO_2 (Chapter 6) where the Nd:YAG laser was utilised. The β parameter for NO_2 is +0.7 which meant that the horizontal polarisation in the laboratory frame ensured that a higher proportion of the photofragments were directed towards the liquid surface.

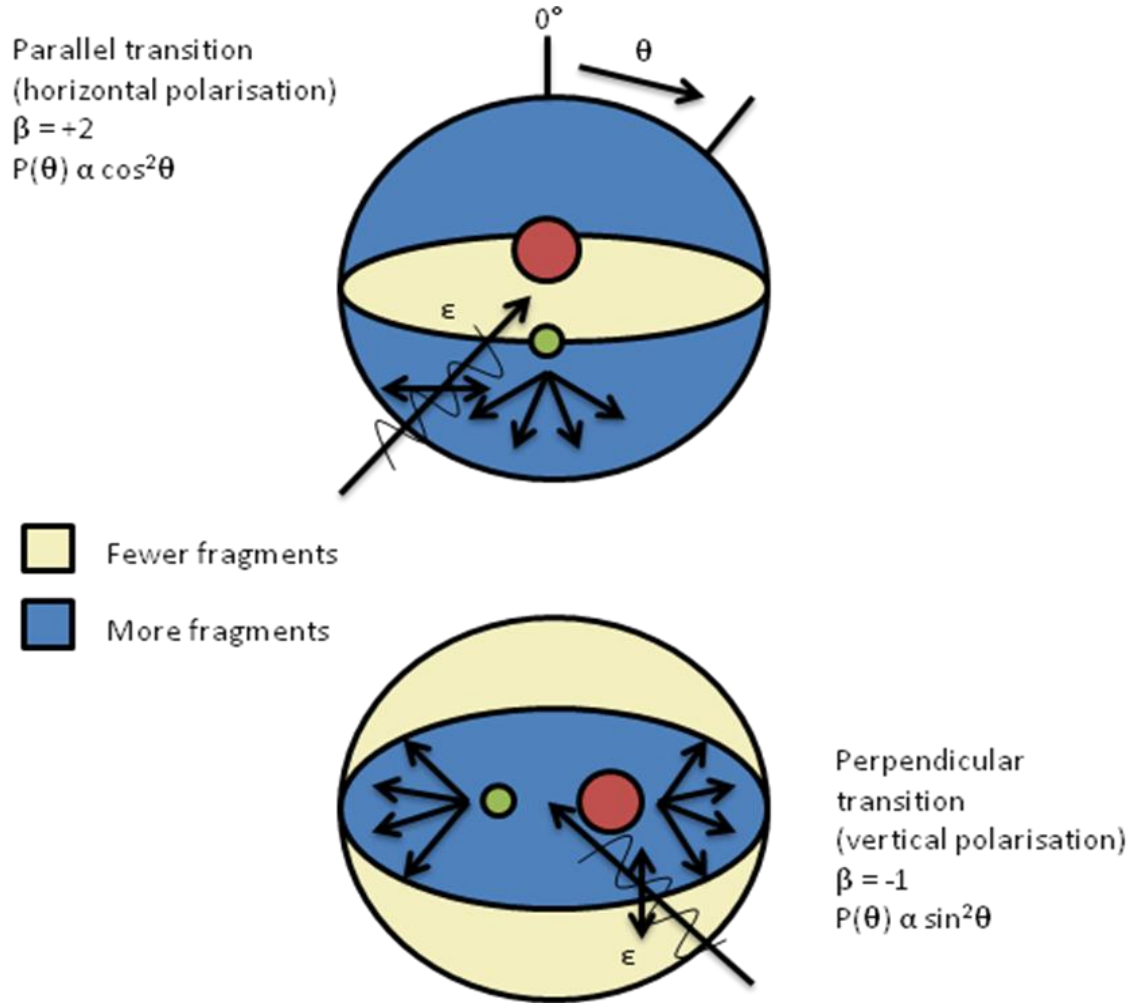

Figure 2.5: schematic of the limiting cases of anisotropy parameter on preferential directional scattering. For NO_2 scattering where β = +0.7, the closest example is the parallel example.

2.7: Probe laser

The probe laser was used to detect the products of the photofragment interaction with the liquid surface. For all experimental studies, the species being detected was OH. To enable different bands of the OH molecule to be accessed (discussed in more depth in Chapter 3) it was important to have a tunable laser which could access a variety of wavelengths. Dye lasers are ideal for this application and an Nd:YAG (Continuum Surelite II-10)-pumped dye laser (Sirah pulsed dye laser, CSTR-LG-24) was used in all of the work described here (shown in experimental schematic, figure 2.4).

The dye laser system is a fairly complex one. The four main components are a resonator, pre-amplifier, amplifier and frequency conversion unit (FCU). A fraction of

the pump beam (generated from the vertically polarised second harmonic wavelength, 532 nm, of the Nd:YAG laser which had a typical output of 250 mJ per pulse^{-1}), is separated by a beam-splitter and guided through the resonator and used to excite dye molecules to the upper state, creating gain from a continually refreshed dye solution in the oscillator cavity. The dye is refreshed as it is circulated by a pump driven by an electric motor. The spontaneous emission is guided on to a grating which is responsible for wavelength selection. The beam then returns through the oscillator cuvette via a different path and is then amplified by both the pre-amplifier and the amplifier to create stimulated emission. In the main amplifier the pre-amplified beam is passed through a further dye cuvette which is pumped by the remaining pump beam. The beam is then directed through the FCU where second harmonic generation is carried out on the laser beam to give the required wavelength.

The grating in the resonator of the dye laser had a groove density of 2400 lines/mm which provides a wavelength tuning range of between 350 and 740 nm. In all cases the off-diagonal transition of the OH molecule was used. In this case, absorption occurs in the 281 – 285 nm range (A-X (1,0) band) and emission occurs in the 312 – 318 nm range (A-X (1,1) band). Further information on OH spectroscopy is detailed in Chapter 3. The dye solutions used in both the oscillator and amplifier contained Rhodamine 6G.

Second harmonic generation was achieved by passing the beam through a KDP doubling crystal, a quartz compensator and a PellinBroca prism unit for wavelength separation, resulting in horizontally polarised laser light in the wavelength range of 260 – 380 nm with a laser linewidth of 1 cm^{-1}. The beam was passed through an iris to produce a smaller beam with a diameter of 3 mm. The typical energies of this beam were 500 μJ – 1 mJ per pulse. A set of black-coated baffles were placed inside the chamber arm to reduce scatter from the probe beam. A small quantity of scatter transforms into a substantial detection signal.

To give linear probe-pulse energies across a wavelength range a calibration curve was constructed by placing a power meter in the beam path and choosing a desired energy for example, 750 μJ, and the position of the FCU motor was set at each individual point on the curve to ensure this energy was achieved. This set of motor positions was then

saved to a file which could be read by the laser. The laser was controlled by custom-written LABVIEW programme, described further in section 2.8.2.

2.8: Detection and acquisition

2.8.1- Fluorescence detection

The OH molecules were probed on the A-X band and the subsequent fluorescence was detected. The molecules are probed on the off-diagonal band ($\Delta\upsilon = +1$) in all experiments. The off-diagonal band was used because the probe laser wavelength and the strongest fluorescence wavelengths are co-incident when using the diagonal band, meaning that the scattered probe laser light cannot be blocked with a filter. In using the off-diagonal transition it was possible to mostly discriminate against laser scatter with two spectral interference filters centred at 311 nm.

The fluorescence was collected perpendicular to the laser axes at a distance of 20 mm from the laser axes with a liquid light guide (Ultrafine technology Ltd, series 300, length 500 mm and active diameter 8 mm). The fluorescence was guided through the filters to the photomultiplier tube PMT (Thorn EMI 9813QB) operating at a typical gain voltage of 1.5 kV.

2.8.2 – Timing and data acquisition software

Experimental control was performed using custom-written data acquisition LABVIEW software [27]. The timing of the lasers were all controlled by a 4 channel delay generator (SRS DG535). The primary trigger was generated from this device for all three lasers, with a frequency of 10 Hz. The flashlamps and Q-switch delays were independently triggered for both the Nd:YAG lasers. A digital oscilloscope (LeCroy Wavesurfer WS434) received the fluorescence signal from the PMT and was triggered simultaneously with the Q-switch of the probe laser to ensure the probe signal always appeared at time zero.

A fluorescence waveform was captured from the PMT output by the oscilloscope for each laser shot. The waveform was acquired over a time-base of 10 µs which included 5 µs sample before the probe was fired. The oscilloscope was operated at a rate of

1 G samples s^{-1}. The waveforms were averaged for a pre-set number of shots (typically 20) and then subsequently passed to the data-acquisition computer via an Ethernet connection (TCP/IP) where they were further processed.

The digital set-up for extracting signals from waveforms was as follows. There were two individual gates for integrating signal. Each was ~1 μs long: one was a signal gate situated directly after the probe scattered-light spike to collect any probe-induced fluorescence. The other was a background gate located before the probe signal to collect a background measurement. The background gate data were subtracted from the signal gate data to produce average integrated signals at each data point. They were all stored on the hard drive in a specified directory and file name. Two main custom LABVIEW [27] programmes were written for the collection of data presented in this thesis. One programme allows the integrated signal as a function of photolysis-probe delay to be captured. The second allows the integrated signal as a function of probe wavelength to be recorded for a fixed photolysis-probe delay. Each experimental output is described further in the following section.

2.9: Experimental Outputs

2.9.1 – Appearance profiles

One of the two main experimental outputs collected were OH appearance profiles. An example appearance profile is shown in figure 2.6 where the appearance of OH (from $O(^3P)$) is shown after reaction with a squalane surface. This was collected by custom-built LABVIEW software as described in section 2.8.2. This type of output gives information on the translational distribution of scattered OH radicals. The probe laser is fixed on a chosen transition of the type OH $A^2\Sigma - X^2\Pi$ rovibrational transition while the delay between the photolysis and probe lasers firing is varied in 1 μs steps. The results collected are typical of those seen previously by McKendrick and co-workers [1-17] where the signal increases quickly to a maximum and decays more slowly. The OH appearance is consistent with detection of molecules which have interacted with the liquid surface and returned to the probe volume. The peak of the returning speed distribution can be loosely correlated to the most probable average speed of returning OH and the known in-going speed of the $O(^3P)$.

The need to ensure single-collision conditions and the steps taken to ensure these were enforced were mentioned in section 2.4.1. It was also noted that results for delays longer than 30 μs were discarded. This is because in a previous study [28] it was found that with increasing pressure signals in low rotational levels (which were not well populated in the thermal distribution) increase linearly with precursor pressure at the peak of the distribution but at the tail end signals increase much faster than linearly. This is due to secondary gas-phase collisions whereby OH molecules have interacted with other gas-phase molecules and become thermalized. These are then present in the probe volume and become more prevalent with increasing pressure. In this previous study [28] it was found that the differences between a theoretical 'zero pressure' appearance profile and having 1 mTorr of gas present was negligible for delays less than 30 μs.

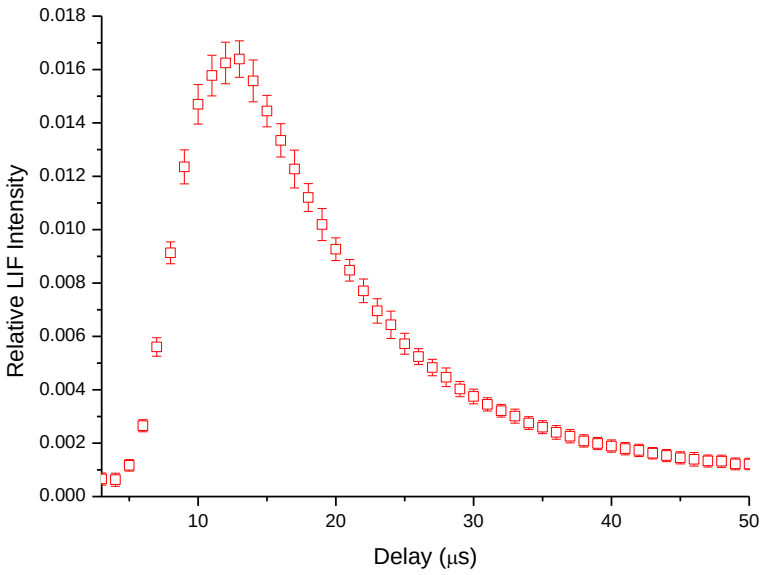

Figure 2.6: An example appearance profile showing the sharp rise to a peak and slow fall of LIF intensity with photolysis-probe delay. The reference shown is an example of OH generated from $O(^3P)$ after reaction with squalane. The trace shown is an average of ten separate scans and the error bars represent a standard 1σ error in the mean.

2.9.2 – LIF Excitation Spectra

LIF excitation spectra were the second main type of experimental output. They were recorded by scanning across a selected wavelength range while keeping the delay between the photolysis and probe lasers constant. An example spectrum is shown in figure 2.7. The rotational populations can be extracted from such spectra. The method selected for this involved recording a thermal spectrum alongside a nascent one. The thermal spectrum is recorded at a higher gas pressure and a longer delay to allow collisional relaxation to occur. The experimental thermal spectrum can then be compared to the theoretical thermal spectrum (from the spectrum-simulation program, LIFBASE [29]). The ratio between the two is calculated for each rotational line, according to equation 2.8, and is referred to as a calibration factor. This factor is then applied to the recorded nascent signals to yield a population corrected for the effective detection sensitivity on that line. The calibration factor accounts for factors such as: the variation of probe energy with wavelength; variation of detection sensitivity with wavelength of the emitted fluorescence and optical saturation.

$$\frac{PN'_{thermal}}{PN'_{theoretical}} = calibration\ factor \qquad \text{Equation 2.8}$$

The data from excitation spectra are further processed by first extracting several relative rotational populations from individual spectra and then averaging these to ensure day-to-day variations were minimised.

These populations were then often conveniently presented as a Boltzmann plot, where the Boltzmann equation (2.9) is used to define the linear relationship of the natural log of the population divided by the degeneracy of each level versus the energy of that level. The gradient in this type of plot is equal to $\frac{-1}{k_B T}$ meaning that the rotational temperature, T can be abstracted.

$$P \alpha g \exp [E/K_b T] \qquad \text{Equation 2.9}$$

The rotational temperature is a useful number for describing the rotational distribution and is convenient for example comparing different liquids. The one drawback of this method is that it assumes the rotational distribution is described by a thermal temperature, which is not always the case. There is no intrinsic reason why a

dynamical process should be described by a single temperature at all and it may be better described by a combination of two or more temperatures. This is discussed further in subsequent chapters.

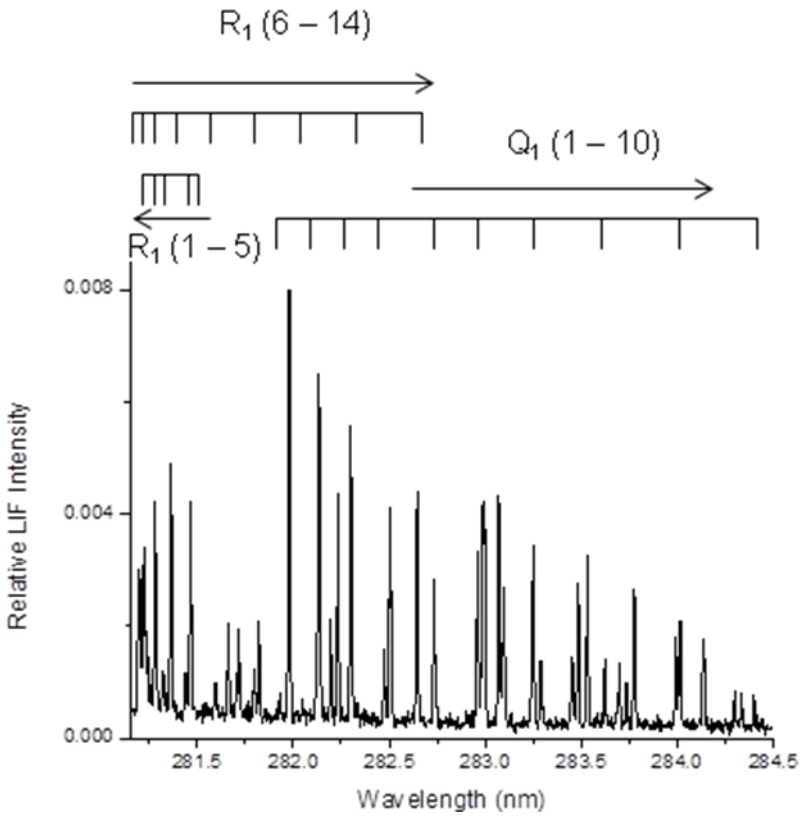

Figure 2.7: A representative LIF excitation spectrum showing a variety of lines originating from different N. The example shown is a spectrum of OH generated from allyl alcohol after interaction with a squalane surface. The spectrum was recorded at a delay of 21 μs. The laser bandwith at 282 nm is 1 cm^{-1}. The laser step size is 0.1 nm.

2.10: References

1. F. Ausfelder and K. G. McKendrick, *Prog. React. Kinet. Mech.*, 2000, **25**, 299-370.
2. F. Ausfelder, H. Kelso and K. G. McKendrick, *Phys. Chem. Chem. Phys.*, 2002, **4**, 473-481.
3. H. Kelso, S. P. K. Kohler, D. A. Henderson and K. G. McKendrick, *J. Chem. Phys.*, 2003, **119**, 9985-9988.
4. S. P. K. Kohler, M. Allan, H. Kelso, D. A. Henderson and K. G. McKendrick, *J. Chem. Phys.*, 2005, **122**, 024712.
5. S. P. K. Kohler, M. Allan, M. L. Costen and K. G. McKendrick, *J. Phys. Chem. B*, 2006, **110**, 2771-2776.
6. S. P. K. Kohler, S. K. Reed, R. E. Westacott and K. G. McKendrick, *J. Phys. Chem. B*, 2006, **110**, 11717-11724.
7. M. Allan, P. A. J. Bagot, S. P. K. Kohler, S. K. Reed, R. E. Westacott, M. L. Costen and K. G. McKendrick, *Phys. Scr.*, 2007, **76**, C42-C47.
8. M. Allan, P. A. J. Bagot, M. L. Costen and K. G. McKendrick, *J. Phys. Chem. C*, 2007, **111**, 14833-14842.
9. M. Allan, P. A. J. Bagot, R. E. Westacott, M. L. Costen and K. G. McKendrick, *J. Phys. Chem. C*, 2008, **112**, 1524-1532.
10. P. A. J. Bagot, C. Waring, M. L. Costen and K. G. McKendrick, *J. Phys. Chem. C*, 2008, **112**, 10868-10877.
11. C. Waring, P. A. J. Bagot, M. T. Raisanen, M. L. Costen and K. G. McKendrick, *J. Phys. Chem. A*, 2009, **113**, 4320-4329.
12. C. Waring, P. A. J. Bagot, J. M. Slattery, M. L. Costen and K. G. McKendrick, *J. Phys. Chem. A*, 2010, **114**, 4896-4904.
13. C. Waring, P. A. J. Bagot, J. M. Slattery, M. L. Costen and K. G. McKendrick, *J. Phys. Chem. Letts.*, 2010, **1**, 429-433.
14. C. Waring, P. A. J. Bagot, M. W. P. Bebbington, M. T. Raisanen, M. Buck, M. L. Costen and K. G. McKendrick, *J. Phys. Chem. Letts.*, 2010, **1**, 1917-1921.
15. C. Waring, K. L. King, P. A. J. Bagot, M. L. Costen and K. G. McKendrick, *Phys. Chem. Chem. Phys.*, 2011, **13**, 8457-8469.
16. C. Waring, K. L. King, M. L. Costen and K. G. McKendrick, *J. Phys. Chem. A*, 2011, **115**, 7210-7219.
17. C. Waring, P. A. J. Bagot, M. L. Costen and K. G. McKendrick, *J. Phys. Chem. Letts.*, 2011, **2**, 12-18.
18. A. Schultz, R. N. Zare and H. W. Cruse, *J. Chem. Phys.*, 1972, **57**, 1354-&.
19. D. L. Andrews, *Applied Laser Spectroscopy*, VCH Publishers Inc., 1992.
20. S. L. Lednovich and J. B. Fenn, *AIChE J.*, 1977, **23**, 454-459.
21. B. F. Parsons, D. E. Szpunar and L. J. Butler, *J. Phys. Chem. A*, 2000, **104**, 10669-10674.
22. F. Turatti, D. W. T. Griffith, S. R. Wilson, M. B. Esler, T. Rahn, H. Zhang and G. A. Blake, *Geophys. Res. Lett.*, 2000, **27**, 2489-2492.
23. H. Okabe, *Photochemistry of Small Molecules*, John Wiley & Sons, 1987.
24. V. Szalay, L. Kovacs, M. Wohlecke and E. Libowitzky, *Chem. Phys. Lett.*, 2002, **354**, 56-61.
25. R. A. W. Johnstone, R. M. S. Loureiro, M. L. S. Cristiano and G. Labat, *Arkivoc*, 2010, 142-169.
26. R. D. Levine, *Molecular Reaction Dynamics*, Cambridge University Press, 2005.
27. G. Paterson, Heriot-Watt University, 2010-2012.
28. C. Waring, Thesis publication, Heriot-Watt University, 2011.
29. J. C. Luque and D. R. Crossley, SRI International, 1999.

Chapter 3: Spectroscopy of the OH radical

This chapter will concentrate on the spectroscopy of the OH radical. The information described below is extremely important as it is used to infer internal state distributions of scattered OH and therefore directly underpins almost all of the experimental results.

3.1: Introduction to OH spectroscopy

The OH radical is crucial to many fields of chemistry including combustion, atmospheric, and space chemistry. As a result of this, the spectroscopy of the OH radical has been well studied both theoretically and experimentally [1-3]. All work presented in this thesis (Chapters 4 – 6) is concerning the $A^2\Sigma^+ - X^2\Pi_i$ band system. This means that energy-level structure of both the ground electronic state ($X^2\Pi_i$) and the first excited electronic state ($A^2\Sigma^+$) must be considered for the transition to be fully understood. These states are described regularly by Hund's coupling cases (section 3.2). Rotational and vibrational population distributions can be extracted from spectra when both rotational line strengths (Hönl-London factors) and vibrational overlap integrals (Franck-Condon factors) are known.

3.2 Electron configuration and term symbols

Within the linear combination of atomic orbitals (LCAO) approximation, the molecular orbitals of the OH radical can be viewed as being formed from the atomic orbitals: the *1s* from hydrogen and the $2p_x$, $2p_y$ and $2p_z$ of oxygen. The resulting molecular orbitals are created: (1σ) (2σ) (3σ) and (1π). In OH most orbitals result from oxygen while the (3) orbital has mixed character. When the nine available electrons are added the following configuration describes the ground state: $(1\sigma)^2\,(2\sigma)^2\,(3\sigma)^2\,(1\pi)^3$. The angular momentum quantum numbers, along with their projections (used in Hund's cases – section 3.3) are listed in table 3.1.

The unpaired electron in the (1π) orbital leads to the ground state being a Π state with a multiplicity of two ($\Lambda = 1$). Σ is +½ or –½ depending on the direction of the projection

of the spin of the unpaired electron. This means that Ω = ½ or 3/2. The overall term symbol is $X^2\Pi_{1/2}$ or $X^2\Pi_{3/2}$.

When an electron is promoted into the first excited state, the electronic configuration becomes $(1\sigma)^2\ (2\sigma)^2\ (3\sigma)^1\ (1\pi)^4$. As there is still an unpaired electron, the multiplicity is still two but this time all electrons are cylindrically symmetrically distributed around the internuclear axis, resulting in a Σ state[1]. Finally a superscript '+' is added to this state to denote that the sign of the electronic eigenfunction is unchanged when reflected in a plane passing through both nuclei. This makes the complete term symbol $A^2\Sigma^+$.

symbol	meaning	allowed values
L	electronic orbital angular momentum	integer to the value of n-1 where n is the principal quantum number
Λ	projection of L, on the internuclear axis	any integer to L
S	electronic spin angular momentum	Each electron = +1/2 or -1/2 therefore any positive half integer value is possible dependent of no of electrons.
Σ	projection of S, on the internuclear axis	Any value from S to -S
J	total angular momentum (excluding nuclear spin)	J = L + S
Ω	projection of J along the internuclear axis (in a non-rotating molecule)	Ω = Λ + Σ
N	total angular momentum excluding electronic spin	N = J - S
R	nuclear rotational angular momentum	R = N - L

Table 3.1: List of angular momentum quantum numbers used for Hund's coupling cases. Note nuclear spin angular momentum, I, is excluded as it has a very weak effect.

3.3: Hund's coupling cases

Hund's cases are used to describe the different modes of coupling of angular momentum due to rotation of the nuclei and electron spin and orbital motion in a diatomic molecule [4]. There are five extreme coupling cases (a) to (e). Only (a) and (b) are required to describe the ground and first-excited electronic state of the OH radical.

3.3.1: Hund's case (a)

Hund's case (a) (vector diagram shown in figure 3.1) illustrates a case of low rotation where L the projection of this onto the nuclear axis is labelled Λ, is "tied" to the internuclear axis by strong electrostatic forces. These forces also decouple L from S. S is also coupled to the internuclear axis but this time it is due to a magnetic field along the axis due to orbital motion of the electrons. The projection of S onto the nuclear axis is labelled Σ. These projections together give the symbol Ω. The coupling between angular momentum of the rotating nuclei, R, and the combined projections of electronic motions, Ω, produces the resulting total angular momentum, J.

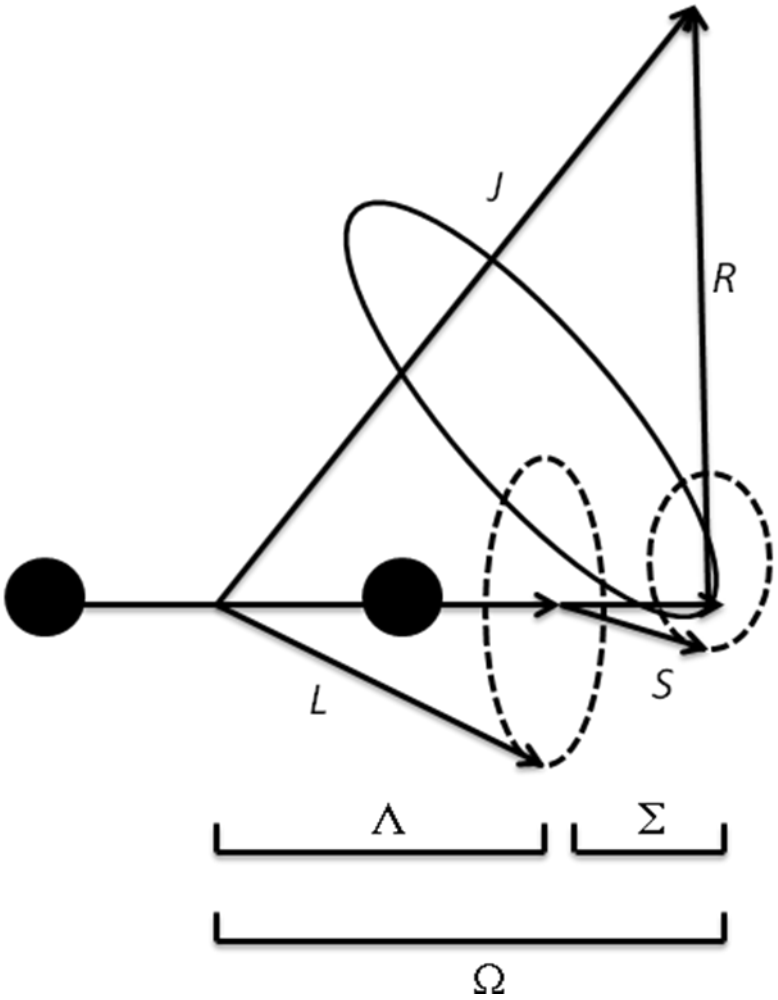

Figure 3.1: Vector coupling diagram for Hund's case (a).

3.3.2: Hund's case (b)

Hund's case (b) applies either when no magnetic field exists (when $\Lambda = 0$) or when there is a weak coupling of S to the internuclear axis (shown in figures 3.2). In the example shown, $\Lambda \neq 0$ but the projection of electronic orbital angular momentum Λ, couples to the moment of nuclear rotation, R to form, N, the total angular momentum excluding spin [5]. The strength of this coupling is dependent on speed (as S is coupling to the magnetic field caused by the rotation of the nuclei) and as the speed of molecular rotation is high in this case, more favourable coupling results. As with case (a), L is strongly bound to the internuclear axis with a well-defined projection, Λ. The angular momentum of the rotating nuclei, R, and, Λ projected onto the nuclear axis give N. N then couples with S to give J.

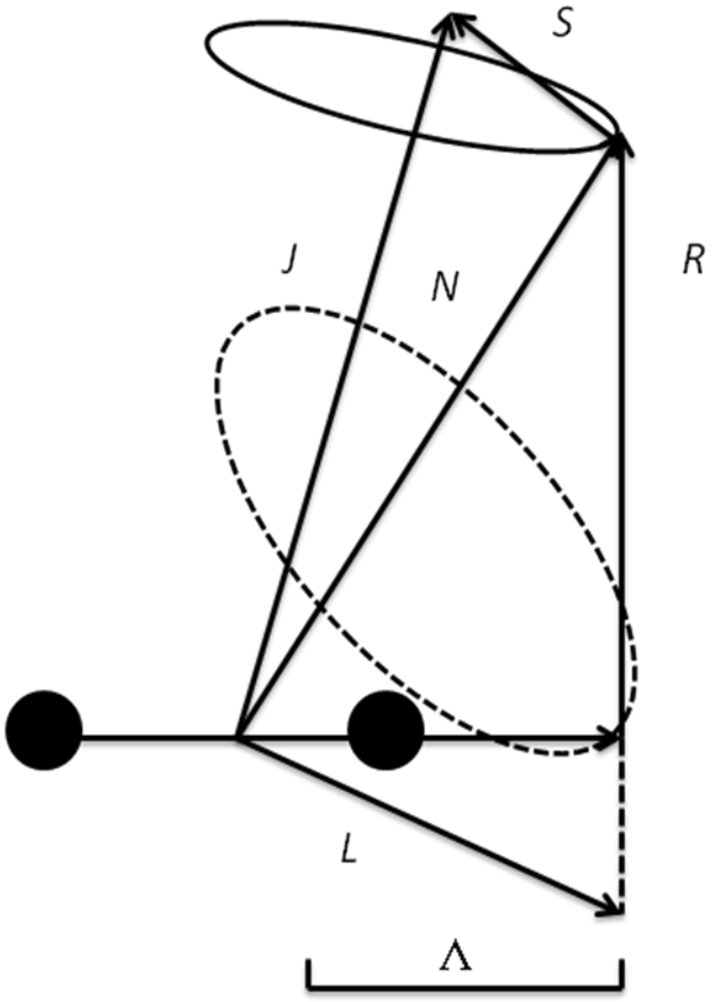

Figure 3.2: Vector coupling diagram for Hund's coupling case (b).

When there is no magnetic field, $\Lambda = 0$, and $S \neq 0$, Hund's case (b) applies automatically. The spin vector, S, does not couple to the internuclear axis. Ω cannot be defined and Hund's case (a) cannot apply. The resulting case is a much simplified version of Hund's case (b) (see figure 3.3).

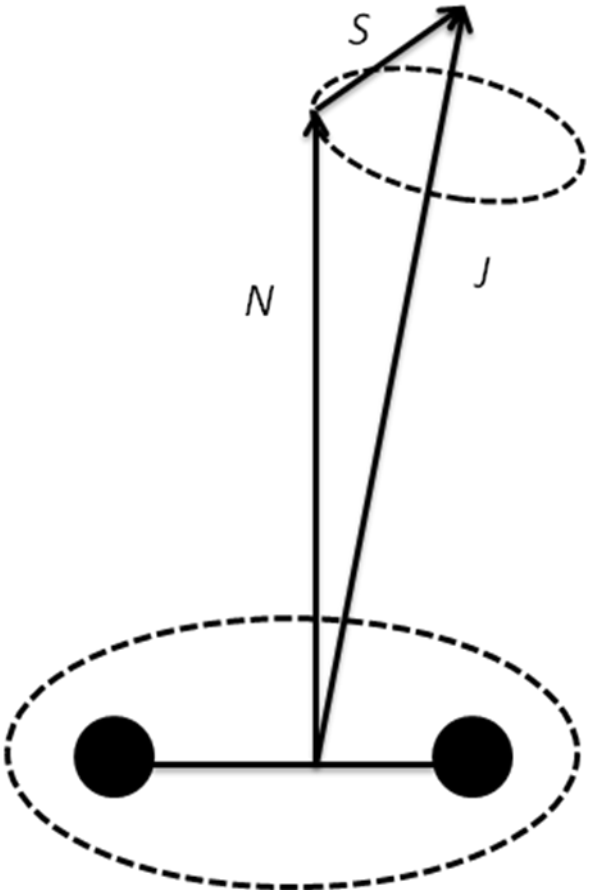

Figure 3.3: Vector coupling diagram of Hund's coupling case (b) in the absence of orbital angular momentum.

3.3.3: Application of Hund's cases to OH ground and excited states and splitting of energy levels

As mentioned in section 3.2, the term symbol for the ground state, X state, is a $^2\Pi$ state. This means that the orbital angular momentum quantum number, $\Lambda = \pm 1$. The high rotational levels can be well described by Hund's case (b) where the high rotational speeds form a favourable R to Λ coupling. For the lower rotational levels, this is not always the entire case but is still present. As $\Lambda \neq 0$ Hund's case (a) must be considered as well as Hund's case (b) and the lower levels are considered to be intermediate between the two cases.

As mentioned in section 3.2., the full term symbol for the ground state of the OH radical is $X^2\Pi_{1/2}$ or $X^2\Pi_{3/2}$. This means that low, more case (a)-like rotational levels are split into two well-separated spin-orbit manifolds for the two differing Ω values. In OH the $X^2\Pi_{3/2}$ lies around 125 cm^{-1} lower in energy than the $X^2\Pi_{1/2}$. This splitting means that there are equivalent transitions originating from each manifold. Due to the $X^2\Pi_{3/2}$

being lower in energy, transitions originating from this manifold for a given N at thermal equilibrium will be more intense that the equivalent $X^2\Pi_{1/2}$ counterpart transition. These manifolds are presented in figure 3.4 and are labelled F_1 for the $X^2\Pi_{3/2}$ manifold and F_2 for the $X^2\Pi_{1/2}$ manifold. The lower energy F_1 state is more populated at 300 K in the ratio 70:30 [6].

A further splitting occurs in the $^2\Pi_i$ state; this is due to the coupling of orbital angular momentum to molecular rotation and is called *Λ* doubling. This results in each rotational level splitting into two very close sub-levels (called *Λ* doublets). The energy gap between these two levels increases with increasing N (shown in figure 2.4 where the gaps between energy levels are exaggerated for clarity). In higher N levels, where Hund's case (b) applies more closely, the *Λ* doublets represent the orientation of the unpaired electron in its orbital lobe. The lobe can either be parallel (in-plane) to the rotation or perpendicular (out of plane) to the rotation. These are labelled A' (symmetric) and A'' (anti-symmetric) respectively corresponding to the lobe position relevant to the plane of rotation. Each Λ doublet is given a parity label either +/f or -/e. This indicates the total parity (symmetric or anti-symmetric) with respect to an inversion operation on the molecular wave-function. This label alternates with N and the lambda doublets of the same N have opposite parity. Levels are labelled e if total parity is $+(-1)^{j-1/2}$ and f if the total parity is $-(-1)^{j-1/2}$ [7]. Only transitions between states of opposite parity are allowed according to spectroscopic selection rules.

For the first electronically excited state of OH, (the A state) the term symbol is $A^2\Sigma^+$ as stated in section 3.2. Because the *Σ* state has no orbital angular momentum projection along the internuclear axis (*Λ* = 0), the simplified Hund's case (b) applies. As the electronic spin is coupled to the rotating nuclei momentum each level is split into two spin-rotation doublets – known as p-type doubling. J = N+½ is used to describe levels from the F_1 manifold ($X^2\Pi_{3/2}$). While J = N-½ is used to describe levels from the F_2 ($X^2\Pi_{1/2}$) manifold.

3.4: Selection Rules

The allowed transitions between two different electronic states are governed by a set of selection rules. The rules specific to the spectroscopy of a molecule composed of light atoms such as OH are outlined in table 3.2. Using these rules it is possible to account for the formation of the six main branches. The Q_1 branch arises from the F_1 manifold where $\Delta J/\Delta N = 0$. Similarly, the Q_2 branch arises from the $\Delta J/\Delta N = 0$ transition but from the F_2 manifold. P_1 is generated from the F_1 manifold from the $\Delta J/\Delta N = -1$ transition, while P_2 is from the $\Delta J/\Delta N = -1$ transition in the F_2 manifold. R_1 is generated from the $\Delta J/\Delta N = +1$ F_1 manifold transition, while R_2 is generated from the $\Delta J/\Delta N = +1$ transition originating from the F_2 manifold.

ΔJ	ΔN	ΔΛ	ΔΣ	ΔΩ	Parity
0, ± 1	0, ± 1	0, ± 1	0	0, ± 1	+ ↔ - - ↔ +

Table 3.2: Selection rules, both general and specific, which are applicable to OH spectroscopy.

In addition to these six branches, there is a possibility for 6 other branches, named satellite branches. Transitions from these are generally much weaker. Satellite branches occur from the fact that OH is intermediate between Hund's coupling cases (a) and (b) in the ground state. This means the selection rule $\Delta J/\Delta N = 0 \pm 1$ is no longer the only option and transitions can occur either where $\Delta N \neq \Delta J$ or where $\Delta N = \pm 2$. These transitions are strongest at low N where the molecule is most like Hund's case (a) but begin to lose intensity on progression to higher N (as the molecule becomes more like Hund's case (b)). These transitions are shown in figure 3.4 and are labelled according to convention, ${}^{\Delta N}\Delta J_{f'f''}$[8]. This label corresponds to the superscript showing the change in N, the main label showing the change in J and the subscript f' describing the spin-rotation state in the upper state and the f'' the spin-orbit manifold in the lower state. For the main branches where $\Delta N = \Delta J$ and f' = f'', this is simplified to $\Delta J_{f'}$.

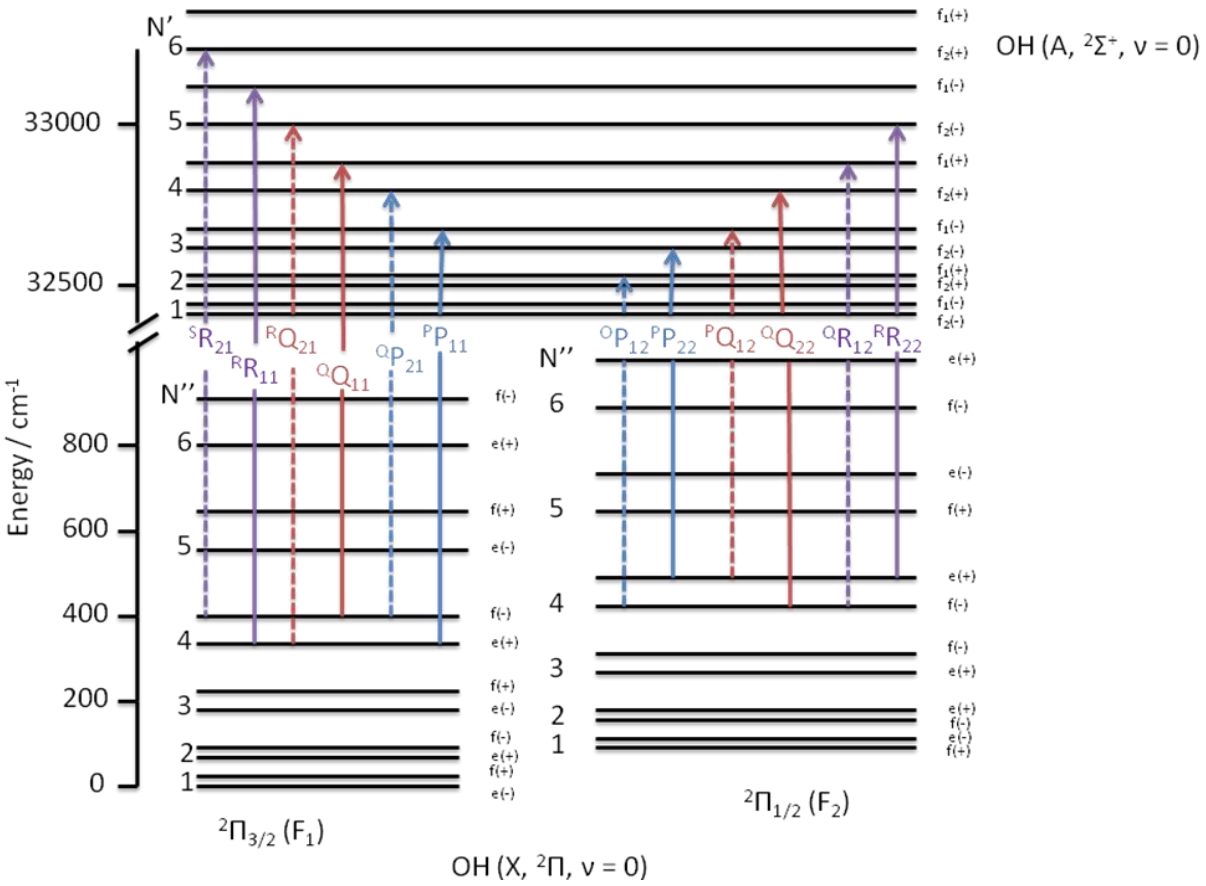

Figure 3.4: Energy level diagram for the OH A-X band showing the six main branches (solid lines) and the additional six satellite branches (dashed lines). The Λ- doublet and spin orbit splitting has been exaggerated for clarity.

3.5: References

1. G. Herzberg, *Molecular Spectra and Molecular Structure*, Van Nostrand Reinhold Company, 1950.
2. G. H. Dieke and H. M. Crosswhite, *J. Quant. Spectrosc. Radiat. Trans.*, 1962, **2**.
3. R. Schinke and P. Andresen, *J. Chem. Phys.*, 1984, **81**, 5644-5648.
4. A. G. Gaydon, *Dissociation Energies and Spectra of Diatomic Molecules*, Chapman and Hall Ltd., 1968.
5. R. N. Zare, *Angular Momentum Understanding Spatial Aspects in Chemistry and Physics*, John Wiley & Sons., 1988.
6. J. C. Luque and D. R. Crossley, SRI International, 1999.
7. M. H. Alexander, P. Andresen, R. Bacis, R. Bersohn, F. J. Comes, P. J. Dagdigian, R. N. Dixon, R. W. Field, G. W. Flynn, K. H. Gericke, E. R. Grant, B. J. Howard, J. R. Huber, D. S. King, J. L. Kinsey, K. Kleinermanns, K. Kuchitsu, A. C. Luntz, A. J. McCaffery, B. Pouilly, H. Reisler, S. Rosenwaks, E. W. Rothe, M. Shapiro, J. P. Simons, R. Vasudev, J. R. Wiesenfeld, C. Wittig and R. N. Zare, *J. Chem. Phys.*, 1988, **89**, 1749-1753.
8. H. Okabe, *Photochemistry of Small Molecules*, John Wiley & Sons, 1987.

Chapter 4: Reaction of O(^{1}D) with a liquid hydrocarbon

This chapter will describe an experimental study of the gas-liquid interfacial reaction of excited state singlet oxygen, O(^{1}D), with the standard liquid hydrocarbon squalane. The aim is to contrast the behaviour with previous experimental work within the McKendrick group on the triplet ground state of oxygen, O(^{3}P) [1-12]. This is the first measurement for heterogeneous gas-liquid O(^{1}D) reactions and therefore no exact comparisons with previous work can be made. Studies completed on O(^{1}D) with hydrocarbons in the pure gas phase will be reviewed and used to help interpret the results collected here.

4.1: Introduction to O(^{1}D): its formation and role in the atmosphere

O(^{1}D) is formed in the atmosphere from ozone or O_2 [13] (equation 4.1 and 4.2). The formation of O(^{1}D) is highly wavelength dependent as other forms of oxygen, such as O(^{3}P), can be formed if different wavelengths of light are used [14].

$$O_3 + hv\ (\lambda < 340\ nm) \rightarrow O(^1D) + O_2 \qquad \text{Equation 4.1}$$

$$O_2 + hv \rightarrow 2O \qquad \text{Equation 4.2}$$

O(^{1}D) is usually formed as a product during reactions such as 4.1 and used up relatively quickly, such as in the process shown in equation 4.3 where OH is formed. When O(^{1}D) is present alongside gaseous hydrocarbons, the reaction shown in equation 4.4 is known to occur. The metastable, energised hydrocarbon complex can then undergo further reactions which will be discussed in section 5.2. The decomposition products of this hydrocarbon complex are those which have been studied in depth in the gas phase but have not yet been observed heterogeneously where the hydrocarbon is a liquid.

$$O(^1D) + H_2O \rightarrow OH + OH \qquad \text{Equation 4.3}$$

$$O(^1D) + RCH_2H \rightarrow RCH_2OH\cdot \qquad \text{Equation 4.4}$$

4.2: Previous O(^{1}D) + hydrocarbon gas phase measurements

The reaction of O(^{1}D) with gaseous hydrocarbons has been extensively studied. The most commonly studied hydrocarbon is methane [15-20] with a few studies including larger gas-phase molecules [21-24]. Only those most relevant to the results presented in section 4.4. will be discussed further.

The most commonly observed occurrence (in experiments) when O(^{1}D) forms the complex shown in equation 4.4 is the collapse of the complex to give a ground state OH molecule and an organic radical as shown in equation 4.5. This outcome is favourable as it is highly exothermic for methane (180 kJ mol^{-1}) and less exothermic but still favourable for larger molecules (~ 40 kJ mol^{-1}). In molecules larger than methane, a second channel becomes available where the C-C bond breaks producing alkyl and O-containing radicals (equation 4.6). As the hydrocarbon molecule gets larger, this channel is more likely to be present. This was discovered in the most early work on O(^{1}D) [25].

$$O(^1D) + HR \rightarrow OH\ (X^2\Pi) + R \qquad \text{Equation 4.5}$$

$$O(^1D) + HR \rightarrow R'HO + R'' \qquad \text{Equation 4.6}$$

The OH which has been generated from O(^{1}D) reacting with methane was generally found to be both rotationally and vibrationally excited with vibrational levels up to the limit of v' = 4 being populated. There was a minor rotationally cold component present but this was confined to the lower vibrational levels. For larger hydrocarbons, the cold component became more dominant where v' = 0 was the most populated level and exhibited a bi-modal rotational temperature over the individual rotational levels. The total yield of OH detected decreased with the size of the hydrocarbon molecule as the mechanism shown in equation 4.6 became more prevalent [26]. The main detection method used in these studies is LIF. Doppler-resolved LIF has been utilised in measuring the polarisation-dependent differential scattering for a few select product levels [27, 28]. There has also been limited characterisation by resonance enhanced multi photon ionisation (REMPI) of energy dispersion in the CH_3 co-product of the reaction with methane [16, 29].

Stephenson and co-workers [20] collected real-time appearance of the OH products from the reaction initiated in a van der Waals complex using ultrafast photolysis and probe pulses. Using results collected in the course of their investigation alongside previous data recorded on the subject proposed that four distinct mechanisms were possible for the reaction of $O(^1D)$ with hydrocarbons.

The first possible mechanism is named *statistical insertion* and occurs where the lifetime of the ROH* complex is long enough for complete internal vibrational energy distribution (IVR) to occur. As a result, products formed in this manner would take longer to appear in an OH spectrum. Any OH product state distribution should be relatively cold, non-inverted and predictable on statistical grounds. The angular distribution should be forward-backward symmetric.

The second mechanism is known as *non-statistical insertion* and is closely related to but distinct from the first mechanism. As before, the $O(^1D)$ inserts into the hydrocarbon to form an excited complex ROH*. In this case the complex only lives for a short time which is sufficient for only a small number of vibrational periods. This means that total IVR does not occur. The OH product state distributions can be expected to be vibrationally inverted and rotationally hot. The angular distribution is harder to define in this case but is expected no longer be forward-backward symmetric. The angular distribution may also be dependent on product level. Any OH formed by this mechanism will appear much sooner on an OH spectrum than with statistical insertion but still takes longer to occur than a single, direct encounter.

The third mechanism is known as *stripping* and occurs when the $O(^1D)$ abstracts a hydrogen in a single, direct encounter. This occurs as the $O(^1D)$ hits the hydrocarbon with a large enough impact parameter to avoid insertion and the formation of the activated complex ROH*. It is hypothesised that the approach of the $O(^1D)$ molecule to the C-H bond which is attacked is perpendicular. The product state distributions which emanate from this type of mechanism are expected to be hot and may be difficult to distinguish from those created by a non-statistical insertion mechanism. The angular distribution of the OH created by this mechanism would be strongly forward scattered which is characteristic of this type of stripping abstraction process. The simplest way to distinguish OH created in this mechanism from OH created from the non-statistical

mechanism is by the time the formed OH takes to appear in the OH spectrum. OH from the stripping mechanism appears very early in time as the mechanism is a “fly-by” mechanism and occurs with minimal loss of initial translational energy.

The final proposed mechanism for the reaction of $O(^1D)$ with hydrocarbons is the *abstraction* mechanism. Reactions of this type occur at a relatively low impact parameter and similarly to the stripping mechanism proceed via a single, direct encounter but conversely to the stripping mechanism, the approach of the $O(^1D)$ molecule is parallel to the C-H bond under attack. The OH formed from this type of mechanism is proposed to be rotationally and vibrationally cold which is contrary to the stripping mechanism. This is due to how the $O(^1D)$ approaches the C-H bond. This approach occurs in a much greater loss of rotational energy to the hydrocarbon. The OH formed in this manner would also be strongly backscattered but would still appear fairly early in the OH real-time spectrum as the whole process is direct and therefore occurs rapidly.

For their work, Stephenson and co-workers assigned the abstraction mechanism to the earliest visible OH and the statistical insertion mechanism to the slowest moving OH. They postulated that intermediate OH must occur as a result of non-statistical insertion, as opposed to stripping, mainly due to appearance time in the OH spectrum. They consequently excluded the stripping mechanism as providing a significant contribution to observable OH.

Yang and co-workers performed a number of crossed molecular beam type studies [30] using methane, ethane, propane and cyclopropane as hydrocarbon sources. They used the angular distributions to assign the OH products to respective mechanisms. They noted a strongly forward scattered component which was assigned as a direct “pick-up” mechanism. This could correspond to either a non-statistical insertion or a stripping mechanism using the terminology detailed above. It could not be assigned to the abstraction mechanism detailed as that mechanism exhibits a backscattered angular distribution. The second observed mechanism was associated with an intermediate which had a long lifetime and produced forward and backwards scattered components. This mechanism is definitely comparable to the statistical insertion described previously. Yang and co-workers saw no OH which could be

assigned to the aforementioned abstraction mechanism proposed by Stephenson and co-workers.

It is important to note that all of the studies summarised previously occur in the gas phase while the experiments detailed in this chapter occur at the heterogeneous gas-liquid interface. This means that some of the mechanisms observed in the gas phase may be applicable but due to the different phases some may not be possible. Nevertheless, assuming a measurable yield of OH is produced, the mechanisms described are a useful starting point to try and assign any product OH that might be observed. As this is the first study which has been completed in the reaction of $O(^1D)$ with hydrocarbons in the gas-liquid phase which means that no direct comparisons to other results are possible and the closest comparisons available are those which have arisen from the gas-phase studies summarised.

4.3: Experimental summary

The broad experimental set-up for this series of experiments is detailed in Chapter 2. In this section details will be presented which are relevant to only this series of experiments. Only the liquid hydrocarbon squalane is used here and all experiments were performed at room temperature (297 ± 3 K).

In this case $O(^1D)$ atoms were generated from a low pressure of N_2O (1 mTorr) photolysed at 193 nm by an ArF excimer lased (GAM EX350) as shown in equation 4.7. The photolysis laser beam was approximately 4 mm by 2 mm with the longer axis vertical in the laboratory frame (parallel with the liquid surface) situated 6 mm from the liquid surface. Typical pulses were ~ 20 ns in length with energies in the range of 50 – 70 mJ in the centre of the experimental chamber. The photolysis beam was effectively unpolarised leading to minor anisotropy in the $O(^1D)$ recoil-velocity distribution. Despite this, a significant portion of the $O(^1D)$ generated will travel towards the liquid surface. The OH returning from the liquid surface was probed by the dye laser pumped by the second harmonic of an Nd:YAG (beam also at 6 mm distance, 3 mm diameter, pulse energies ~ 1 mJ) on the $A^2\Sigma^+ - X^2\Pi_i$ (1,0) band which occurs at

around 280 nm. The returning fluorescence was detected by a liquid light guide as described in section 2.8.1.

$$N_2O + h\nu \rightarrow O(^1D) + N_2 \qquad \text{Equation 4.7}$$

The $O(^1D)$ generated by photolysis of N_2O has been well characterised by other groups [31, 32]. The speed distribution is approximately Gaussian with the properties detailed in table 4.2.

Average lab-frame E_k (kJ mol^{-1})	Average collision speed (ms^{-1})	Energy available to products (kJ mol^{-1})
109	3690	290 -330

Table 4.2: Summary of properties of $O(^1D)$ generated from the photolysis of N_2O. The energy available to products (relative to the OH product channel) in reaction with a hydrocarbon varies with the nature of the C-H bond type.

4.4: Experimental results

Obtaining results from the reaction of $O(^1D)$ with liquid squalane is in some respects much simpler than the experiments detailed in Chapter 5 where OH is present before and after collision. In this case any OH signal which is seen must be from $O(^1D)$ which has reacted with the liquid surface to abstract a hydrogen. On return to the probe volume, the OH is detected by LIF and no subtractions are necessary.

4.4.1: Appearance profiles

This study provides the first conclusive proof that OH can escape the surface of a liquid hydrocarbon after the reaction with $O(^1D)$. It was found that OH could be observed in a wide variety of rotational levels in the ground state vibrational level v'' = 0. There may also be vibrationally excited products present but this point cannot be confirmed or denied here as the study is limited to vibrational ground state products.

A general description of appearance profiles was provided in section 2.9.1. The description given here will be more detailed and in some ways specific to this set of experiments. As a reminder, an appearance profile is collected while increasing the

delay between the photolysis and probe lasers. During these measurements the probe laser is set at a fixed wavelength of a selected transition.

The day-to-day collection of these appearance profiles followed a set procedure to ensure reproducibility. First a transition was selected (three were studied in this section of work $Q_1(1)$, $Q_1(5)$ and $Q_1(10)$) and the probe laser was set to the approximate wavelength; using the theoretical wavelength from LIFBASE [33] as a guide. The probe laser was slowly scanned in both wavelength directions at a photolysis-probe delay of 10 μs (this is a reasonable delay to assume that sufficient OH will be present in the probe volume to be detected). The intensity of the LIF signal was recorded and monitored regularly to check stability. A set of appearance profiles was then collected at this desired wavelength. Each set comprised of ~10 scans which were then averaged.

After collecting each set of 10 scans, four further scans were taken. Two were under the same experimental conditions except with the probe laser blocked – known as 'photolysis only'. A further two were with all the same experimental conditions but with the photolysis laser blocked – known as 'probe only'. The photolysis-only and probe-only profiles were both subtracted from the primary data to remove any background contributions to the signal generated by either laser alone. Including these extra scans, each set took just over an hour to collect. All results presented in graphical form below were collected on at least three separate occasions and are therefore an average of at least thirty separate appearance profiles. The raw data collected in this manner are presented in figure 4.1. In figure 4.2 the data are presented again where they have been transformed into approximate flux densities.

It is not straightforward to do a rigorous density-flux transformation on the appearance profiles because of the experimental broadening effects. Nevertheless, an approximate one can be achieved quite simply by defining a fixed flight time for the $O(^1D)$ to the surface. This is taken to be 1.68 μs, calculated simply from the average speed of the $O(^1D)$ and the mean distance of 6 mm to the surface. It is likely that this is a slight underestimate, because the $O(^1D)$ will, on average, have travelled at some angle to the surface normal.

Approximate flight times of the OH back from the surface result from subtracting this time from the observed appearance time. Relative fluxes are then obtained by dividing the observed densities by the OH flight time, which is equivalent to weighting by the OH speed.

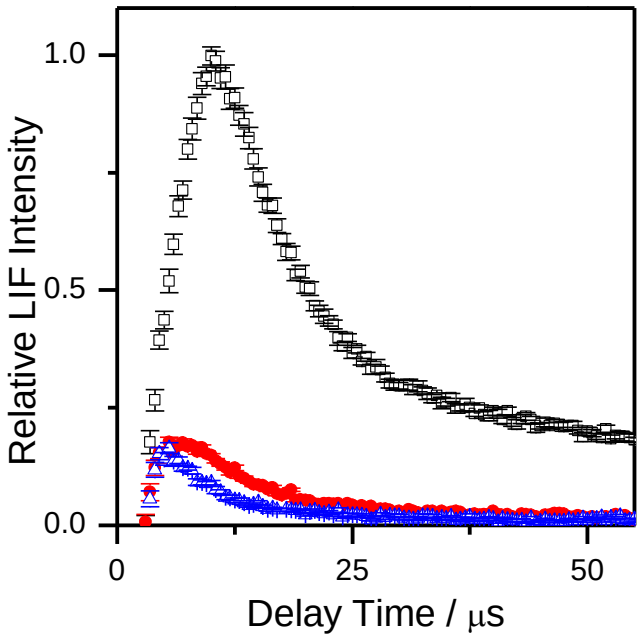

Figure 4.1: Appearance profiles recorded on the OH *A-X* (1,0) band. Probe transitions: $Q_1(1)$ (black open squares); $Q_1(5)$ (red closed circles); and $Q_1(10)$ (blue open triangles). Photolysis and probe laser backgrounds have been subtracted, as described in the text. Error bars are the 1σ standard error in the mean of the measured data points. $P(N_2O)$ ~1 mTorr, wheel-laser axes distance = 6 mm. The $Q_1(1)$ data are normalised to 1 with the other lines appearing in their correct relative sizes.

The shapes of the appearance profiles are very different for each individual *N* level. For *N* = 10, the peak of the appearance profiles is very early and occurs between 5 and 6 μs. For *N* = 1, the peak is later and occurs at 10 – 11 μs. The peak for *N* = 5 occurs intermediate between the two at 7 – 9 μs. Also in *N* = 1, the signal is still very high when the graph ends at 45 μs. It can be observed that signals do not decay to zero at long delays and are *N* dependent and correlate with peak signal intensity. It is believed that this is due to thermalised gas-phase OH which is initially formed through secondary gas-phase collisions of OH generated initially at the liquid surface.

There is a pronounced translational-rotational correlation with the fastest molecules also being the most rotationally excited.

The peak flux for each level differs in size also, where $N = 1$ is over three times larger than the peak for $N = 5$ and 10; this is probably largely due to the fact that the $N = 1$ level is lower in energy, and in a reaction where it is possible to lose a large quantity of energy to the liquid surface, a larger population of OH would be expected to scatter with low energy.

The results of the flux density transformation shown in figure 4.2 shows that the faster contributions at shorter delays become amplified relative to the measured density profiles. Since the higher N profiles peak at earlier times, they also gain successively in terms of either peak flux or integral area relative to $N = 1$. Nevertheless, the transformation is not sufficient to suppress the overall dominance of $N = 1$, which remains clearly the majority product in terms of flux.

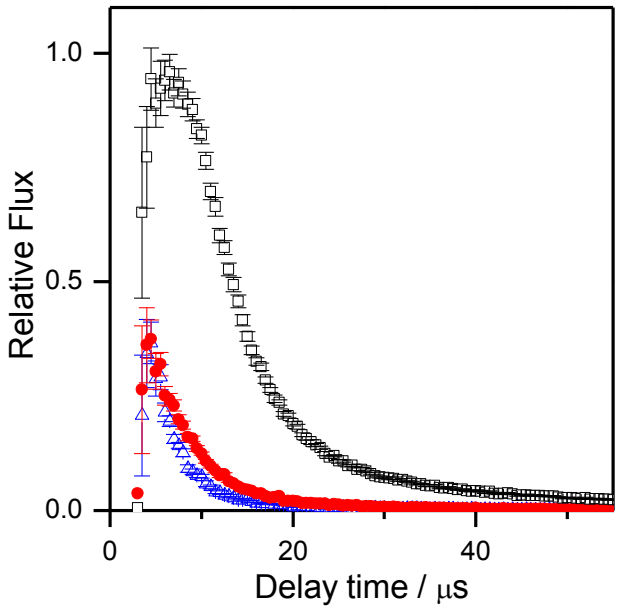

Figure 4.2: Representative OH appearance profiles, inversely time-weighted to reflect fluxes (see text). $Q_1(1)$ (open black squares), $Q_1(5)$ (red closed circles), $Q_1(10)$ (blue open triangles).

Unusually, it appears that the OH which returns in each rotational level is travelling at very different speeds. To enable an easier comparison the profiles have been normalised at their respective peaks and re-presented in figure 4.3. Also included in the figure is a series of Monte Carlo simulations of the type used in previous work (this procedure is described in appendix 1) completed by the McKendrick group [4, 10, 11, 34]. These simulations allow the quantitative variations in the absolute OH speed distributions to be assessed more easily. The simulations average correctly over the known distribution of initial O(^{1}D) velocities from N_2O photolysis [31, 32], including the modest effects of translational anisotropy (neglecting any speed dependence) with $\beta = 0.5$. Also modeled are the experimental geometric broadening factors. These include the finite dimensions of the photolysis beam; the region of the surface from which recoiling molecules are produced; and the restricted probe volume from which LIF is detected. Account is taken of the time spent in the probe volume by OH molecules with different speeds, so the predicted profile represents number density, as shown in figure 4.2.

The predicted profiles shown in figures 4.3 and 4.4 for OH are assumed to have thermally desorbed (TD) from the surface, following a negligible residence time, at different Boltzmann temperatures. The distribution of flight times to the surface is a fixed characteristic of the N_2O photolysis and as a result of this is independent of the assumed temperature in the desorption step.

The thermal-desorption-only simulations are not used because it is expected that the observed profiles to be well described by TD distributions, but because this avoids the need for any dynamical assumptions about the scattering process and represents the least-biased assumption of the angular distributions (which follow a simple $cos\ \vartheta$ distribution, where ϑ is the scattering angle measured from the surface normal, for thermal desorption). The method for generating this TD simulation is discussed in appendix 1.

Similarly, a speed scale has been added to figures 4.3 and 4.4. This was generated by running simulations at a number of temperatures and recording the average speed at the peak of the simulated signal. Smooth interpolation then provided the equivalently defined speed markers in figures 4.3 and 4.4.

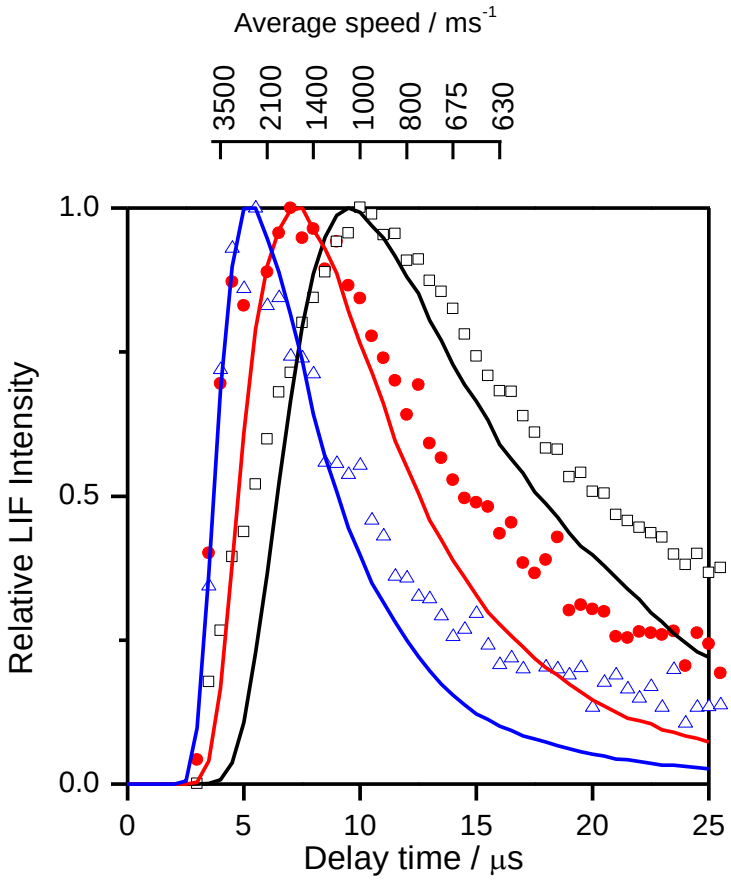

Figure 4.3: Representative peak-normalized appearance profiles, together with Monte-Carlo simulations, as described in the text. Experimental data: $Q_1(1)$ (black open squares); $Q_1(5)$ (red closed circles); $Q_1(10)$ (blue open triangles). TD Boltzmann simulations: 800 K (solid black line); 2000 K (solid red line); 5000 K (solid blue line).

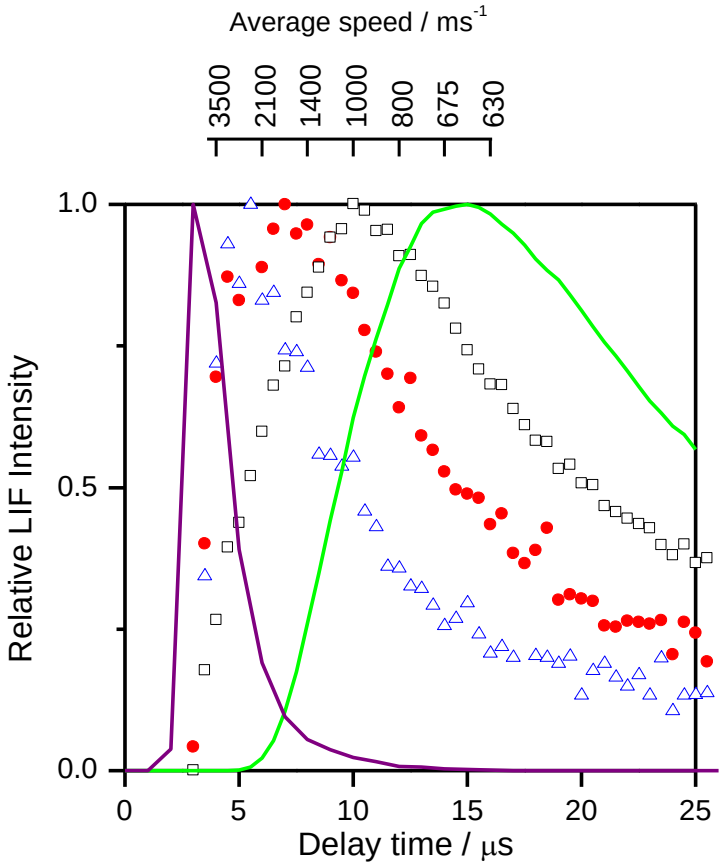

Figure 4.4: Representative peak-normalized appearance profiles, together with Monte-Carlo simulations, as described in the text. Experimental data: $Q_1(1)$ (black open squares); $Q_1(5)$ (red closed circles); $Q_1(10)$ (blue open triangles). TD Boltzmann simulation: 300 K (solid green line). Also included is a simulation of the directly scattered (IS) OH from hyperthermal $O(^3P)$ (solid purple line).

It is clear from figure 4.4 that even for N = 1 a significant proportion of the translational distribution is hotter than the room temperature of the liquid: the observed profile rises much more rapidly and peaks at ~10 μs, whereas the 300 K TD simulation peaks at ~15 μs.

A TD distribution peaking at 10 μs would have a temperature nearer 800 K and a corresponding peak speed of around 1000 m s^{-1} (figure 4.3). Even this hotter TD simulation fails to reproduce the much prompter rising edge of the observed profile for N = 1. The higher rotational levels are substantially faster, rising very sharply and peaking in the region where the synthetic speed scale is becoming compressed. Small changes in the peak position, which is not precisely determined due to some scatter in the experimental data, therefore correspond to large changes in speed. Although they

should not therefore be taken too literally, N = 5 peaks no later than ~7 μs, implying a peak speed in excess of 1600 m s^{-1} or a translational temperature of order 2000 K, and N = 10 around 5.5 μs, corresponding to 2300 m s^{-1} or nominally as hot as 5000 K. It is important to remember that the simulations with single TD temperatures optimised to the observed peaks are not particularly good representations of the whole profiles, implying non-Boltzmann and potentially multi-component translational energy distributions. They are merely being used to illustrate the vast speed and possible temperature differences over the three rotational levels.

4.4.2: LIF excitation spectra

LIF excitation spectra were collected by varying the wavelength of the probe laser while keeping the delay between the photolysis and probe laser pulses constant. This resulted in a rotationally resolved excitation spectrum collected across a designated wavelength range.

The LIF excitation spectra were collected following the appearance profiles. Guided by the appearance profiles it was decided to collect excitation spectra at 4, 8, and 12 μs. These delays were chosen as they correspond to the rising edge, peak and falling edge of the N = 1 transition. A thermalised spectrum was also collected by photolysing 1 mTorr N_2O in the presence of 20 mTorr of gas-phase cyclohexane and 80 mTorr of N_2. The spectrum was recorded at a delay of 100 μs. The large pressures of gas and long delays were specifically chosen to ensure that the OH produced had become thermally accommodated before the spectrum was collected.

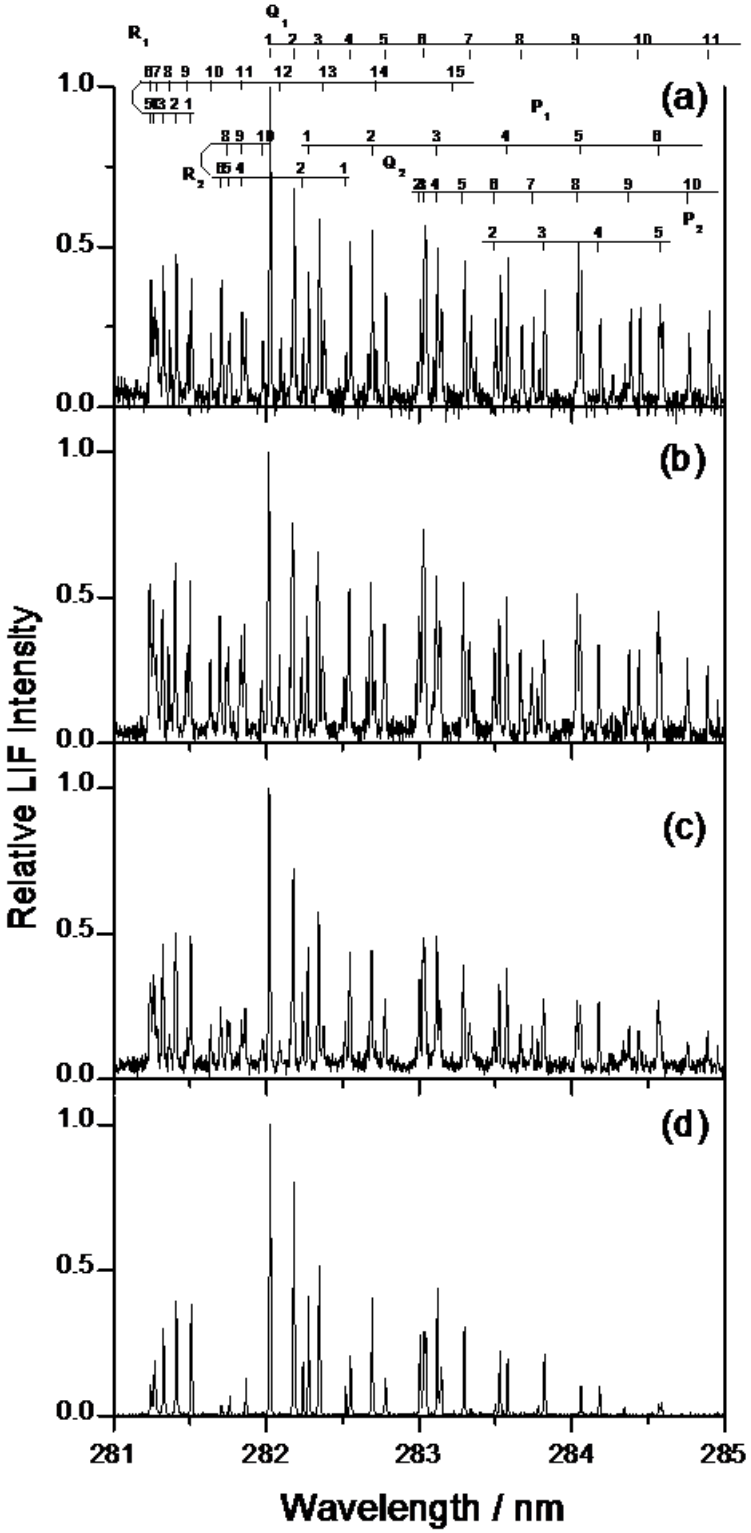

Figure 4.4: LIF excitation spectra on the OH *A-X* (1,0) band at photolysis-probe delays of (a) 4 μs , (b) 8 μs , (c) 12 μs and (d) the thermalised spectrum. All spectra have been normalized to the intensity of the strongest line ($Q_1(1)$). Bath temperature ~297 K, $p(N_2O)$ ~1 mTorr, wheel-laser axes distance = 6 mm. Laser linewidth 1 cm^{-1}, laser step size 0.1 nm.

When comparing the spectra for squalane at different delays, clear differences can be observed. In Fig. 4.4(a) it can clearly be seen that many lines are present up to a high *N.* Within a chosen branch, such as the R_1 branch on the left hand side of the spectrum, the low and high *N* lines are a similar size indicating a high temperature. As time progresses, the ratio between the intensities of the low *N* to high *N* lines increases as well as there being a reduction in the sheer number of higher *N* lines, both of which indicate cooling. However, it is important to note that the high *N* lines are still present even at long delays. This is indicative of the fact that these distributions may not conform to a single temperature.

4.5: Analysis of Results

To extract any further information from the results presented in section 4.4, further processing must take place. The excitation spectra are the most complex, where several steps are required to extract populations and subsequently infer other properties such as rotational temperatures.

4.5.1: Extraction of populations

To confirm whether or not the scattered OH conforms to a single temperature, a Boltzmann plot must be constructed where the population of each, individual *N* level divided by degeneracy is plotted against the energy for each level. If the plot is linear, then only a single temperature is present and extraction of the temperature is simple as it is contained within the slope of the graph. The first step in completing this process is to extract populations from the collected excitation spectra presented in figure 4.4.

To extract the populations from an excitation spectrum the simulation programme LIFBASE has been used [33]. The collected excitation spectrum is imported into the simulation programme and settings are adjusted so that the transitions line-up. For each branch in turn, the heights of the simulated spectrum are matched to the heights of the experimental data collected. The programme then transforms the heights into relative populations. These relative populations can be turned in to absolute populations if required by measuring the intensity of the LIF signal at one particular

transition and multiplying the relative populations by this number. In the excitation spectra, it may not be possible to extract populations from all lines as they may be overlapped with another from a different branch. In this case, these lines will be absent from the population data collected. The population data extracted are shown in figure 4.5.

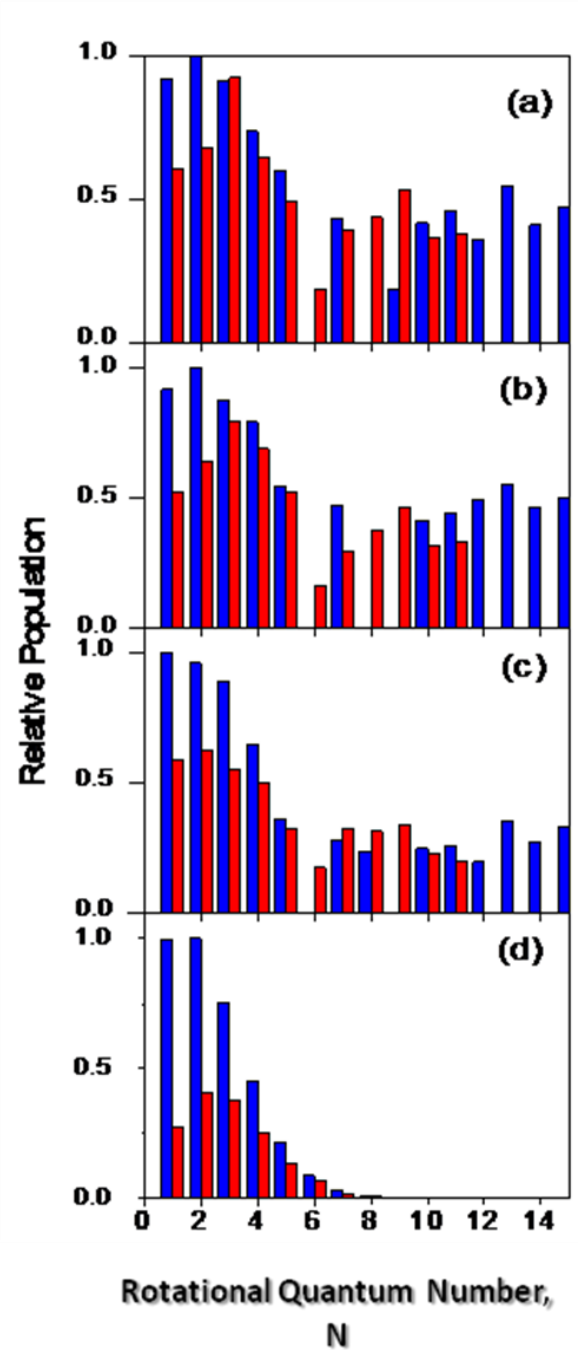

Figure 4.5: Relative populations as a function of rotational quantum number, *N*, and spin-orbit state, F_1 (blue bars) and F_2 (red bars), for different photolysis probe-delays: (a) 4 μs; (b) 8 μs; (c) 12 μs; (d) 300 K Boltzmann distribution. The F_2 branch is normalized to unity at its largest population. The F_1 branch is shown in the correct relative ratio.

Looking at panels, a, b and c of Fig. 4.5, it can be seen that the degree of rotational excitation clearly decreases with time. This is apparent as a decrease in the ratio of the higher *N* levels to the lower *N* levels.

The effect of cooling is also noticeable in the lower *N* lines, where at 4 μs the highest low *N* line is *N* = 3 but at 12 μs, this has changed to *N* = 2. This indicates a trend towards more ambient temperatures.

Indeed, comparison with the thermal (300 K) simulation shown in Fig. 4.5(d) can also provide further insight. It can be seen that the thermal simulation looks fairly similar to the scattered signals over all delays for low *N* (1-5). This is the strongest evidence thus far that a cold component is present in the scattered OH. It is already obvious that a hotter component is present due to the fact that any population is present in higher *N* levels as populations would not be observed above ~ N = 6 for thermal OH.

Once the LIF excitation spectra have been transformed into populations, further steps can be taken to present the populations in the form of Boltzmann plots from which the rotational temperatures can be extracted.

The extracted population for each *N* level is divided by the degeneracy of that specific *N* level and then a natural log of this is taken. This value is plotted against the energy of each specific *N* level. This will provide the Boltzmann plot. If the plot is linear, then only a single temperature is present and extraction of the temperature is simple as it is contained within the slope of the graph. If the graph shape is curved or in some other way multimodal, then the data are not well characterised by a single temperature. This is clearly the case here, as shown in Fig. 4.6. The next simplest representation is a two-temperature model, defined by equation 4.8.

$$\frac{P(N')}{g_{J'}} = c\left(\frac{\alpha \exp\left(-E(N')/k_{\mathrm{B}}T_1\right)}{T_1} + \frac{(1-\alpha)\exp\left(-E(N')/k_{\mathrm{B}}T_2\right)}{T_2}\right) \qquad \text{Equation 4.8}$$

where *P(N)* are the populations specific to each *N* level, $g_{J'}$ is the degeneracy at each specific level. *c* is an overall proportionality constant. T_1 is the colder temperature and T_2 is the hotter temperature. α is the proportion of molecules in the colder temperature T_1. *E(N)* is the energy of each specific *N* level and k_B is the Boltzmann constant.

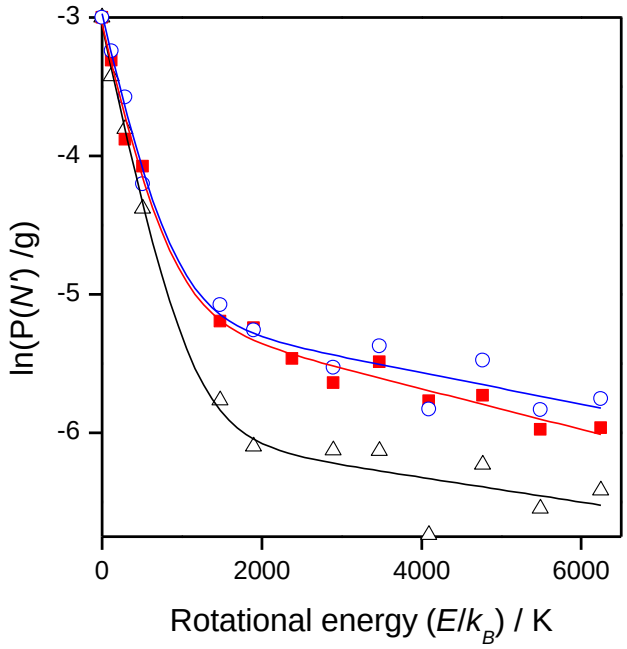

Figure 4.6: Boltzmann plots (natural log of rotational population divided by degeneracy, against rotational energy) for the R_1 branch at the three different delays: 4 μs (blue open circles); 8 μs (red closed squares); 12 μs (black open triangles). The solid lines are the result of fitting a two temperature Boltzmann model (as described in the text) to the respective data sets. Error bars have been omitted for clarity.

Upon examining the data is figure 4.6, a few initial points can be noted. It is immediately obvious that there are definitely at least two temperatures present at all delays. The 4 and 8 μs curves appear very similar to one another, especially at low *N*, while the 12 μs curve is slightly different in both cases, most notably in the proportional contribution at higher *N*. All branches exhibited similar results. The results can be compared more easily in terms of the summary parameters from the two-temperature fit, which are collected in table 4.3.

Delay / μs	T_1 / K	T_2 / K	α
4	300 ± 70	6900 ± 2100	0.30 ± 0.05
8	300 ± 50	4000 ± 1500	0.40 ± 0.08
12	290 ± 20	6800 ± 600	0.44 ± 0.03

Table 4.3: Results of fitting to two temperatures (equation 4.8) for the populations collected at the denoted delays. The results are weighted averages from independent fits to data collected from the four main branches: Q_1, Q_2, R_1 and R_2.

For squalane, the lower temperature is thermal and remains fairly constant at all delays. However, the proportion of molecules present with the lower temperature increases with delay.

The upper temperature is somewhat harder to define than the lower and due to the large error margins it is not sensible to infer a trend which develops over time. However, it can be said that the upper temperature is much hotter than thermal and is likely to lie in the range of 4000 – 8000 K.

4.5.2: OH yield and possible O(^{3}P) contribution

In this section an estimate on the upper limit on the quantum yield of OH per O(^{1}D) atom that reacts at the surface will be made. This upper limit will not be precise, but an order-of-magnitude estimate which will still be useful for the purposes of mechanistic interpretation. In addition to this, it is known that in the photolysis of N_2O at 193 nm, a small quantity of O(^{3}P) is formed [35, 36]. An estimate on the quantity of OH formed from O(^{3}P) created as a by-product of the N_2O photolysis will also be attempted.

Both these estimates rely on the relationship between the OH LIF signal sizes in the current experiments and those in related work performed by the McKendrick group on O(^{3}P) created by photolysis of NO_2 at 355 nm [11].

Using the data presented here in conjunction with the data collected on O(^{3}P) [11], a limit of the fraction of OH generated from O(^{3}P) in the data can be estimated. First, the

ratio of LIF signals in the two experiments, measured on the $Q_1(1)$ line at the peak of the respective appearance profiles is taken. The O(^{3}P) data were collected at a different PMT voltage from the O(^{1}D) data. This difference in gain for the two experiments is 0.1. The relative uncertainty in this value is estimated to be at least a factor of ~2, but this is still smaller than those in some of the other estimated quantities that follow.

An estimate of the OH quantum yield from the O(^{1}D) reaction is necessary to estimate these factors. Assuming all other experimental variables, such as probe-pulse energy, precursor pressure, the optical filtering arrangement, etc, to have been equal (which is known to be the case), the ratio of LIF signals $I(O^1D)_{193}$ / $I(O^3P)_{355}$ will be governed by equation 4.9.

$$\frac{I(O^1D)_{193}}{I(O^3P)_{355}} = \frac{\sigma(N_2O)_{193}}{\sigma(NO_2)_{355}} \times \frac{\phi(O^1D)_{193}}{\phi(O^3P)_{355}} \times \frac{n_{phot,193}}{n_{phot,355}} \times \frac{g(O^1D)_{193}}{g(O^3P)_{355}} \times \frac{p_{N'=1} f_{N'=1}(O^1D)_{193}}{p_{N'=1} f_{N'=1}(O^3P)_{355}} \times \frac{R(O^1D)_{193}}{R(O^3P)_{355}} \times \frac{\Phi(O^1D)_{193}}{\Phi(O^3P)_{355}}$$

- Equation 4.9

The terms in equation 4.9 are defined as: σ is an absorption cross section at the specified wavelength; φ is the quantum yield of the relevant type of O atom; n_{phot} is the number of photons in the photolysis pulse; g is a geometric factor for the proportion of the O atoms that hit the surface; pf is a compound factor, not strictly expressible as a simple product because the appearance profiles are a function of N, describing the fraction (p) of the OH rovibrational product-state distribution that resides in the probed level $N = 1$ and the effects of flux on the peak signal (f) due to the speed at the observed peak and its ratio to the integrated flux of OH, including any bias in the OH angular distribution; R is the fraction of those O atoms that hit the surface that react; and Φ is the quantity of interest, the quantum yield for free OH from the reaction at the surface.

In summary, this gives the values shown in equation 4.10.

$$\frac{I(O^1D)_{193}}{I(O^3P)_{355}} = \frac{1}{5} \times \frac{1}{1} \times \frac{1}{2} \times \frac{1}{1.5} \times \frac{1 \times 1}{2 \times 1.5} \times \frac{1}{< 0.01} \times \frac{\Phi(O^1D)_{193}}{0.7} = 0.1$$

Equation 4.10

These factors are derived as follows: Some quantities are well known and published in literature (σ and ϕ for each molecule at the required wavelengths) [14]. The geometric factors are predicted by the Monte Carlo simulations as detailed in section 4.4.1. This gives a ratio of 1/1.5 which favours $O(^3P)$ due to the use of a polarised beam optimised for a positive β parameter.

The compound factors *pf* are more difficult to estimate. An exact value would require a full set of appearance profiles for all product levels to be analysed, but these are not available. Ideally this factor should include vibrationally excited levels. Excited levels are known to be a relatively minor channel for $O(^3P)$ but this information is not known for $O(^1D)$. The speed-dependent product angular distributions would also be needed, but nothing whatsoever is known for the $O(^1D)$ reaction with liquid as it has never been performed before and only non-state-specific information at higher collision energies is available for $O(^3P)$ [37, 38]. Nevertheless, neglecting the unknown angular dependence, it is estimated by inspection of those profiles that have been measured here for $O(^1D)$ and previously for $O(^3P)$ [4, 5, 8] that overall *pf* factors favour $O(^3P)$ by a factor of around 3. This is a combination of both the colder rotational distribution (p ~1/2) and the lower speeds of the resulting OH (f ~1/1.5).

No other primary product channels are open in $O(^3P)$ experiments at low collision energies. However, secondary loss through reaction to form H_2O is known to be possible. In the most recent work from the McKendrick group on *direct* scattering of OH from liquid squalane, this has been measured to be near 30% [34]. In the absence of other information the quantum yield for OH formation in the $O(^3P)$ reaction is taken to be 0.7. Further information on $O(^3P)$ reactions is provided in Chapter 6.

There is no direct experimental information on R for $O(^1D)$. However, given the near gas-kinetic rate constants for reactions with hydrocarbons in the gas phase, it would be expected that a very high proportion of the $O(^1D)$ that hits the squalane surface will react. It is therefore reasonable to assume R ~1 in this case. For $O(^3P)$, there have been no quantitative measurements of the reaction probability for the photolytically generated distribution. However, only a fraction (~40%) of the $O(^3P)$ laboratory-frame kinetic energy distribution from 355 nm photolysis of NO_2 lies above the typical barrier

of slightly over 20 kJ mol^{-1} for $O(^3P)$ abstraction reactions from the weaker secondary or tertiary H-C bonds [1, 39]. It also known from previous MD simulations that around half of the squalane surface is occupied by primary H-C sites, which have been demonstrated to be considerably less reactive towards these $O(^3P)$ atoms [6, 40]. Even at the very much higher collision energies of ~500 kJ mol^{-1} in the Minton group experiments on $O(^3P)$ + squalane [41, 42], the inelastically scattered O atom channel dominates reactive production of OH by around a factor of 2. The excitation function for $O(^3P)$ + squalane is unknown, but the reactivity would be expected to decline substantially towards threshold from the high energies present in the Minton experiments. In earlier work [37], the un-calibrated OH/O ratio of peak signals in the IS channel at a single, selected combination of initial and final angles was ~0.03 at an average collision energy of 21 kJ mol^{-1}, which happens to coincide with the energy threshold assumed above.

No theoretical predictions have been reported for $O(^3P)$ + squalane itself (the reactivity has been predicted only at 5.0 eV) [43]. The most relevant available prediction is a reactivity of 0.05, also at an energy of 21 kJ mol^{-1}, for the related collisions of $O(^3P)$ atoms with a model self-assembled monolayer of alkyl chains [44]. This value is probably over-estimated because both the barrier height on the optimized potential surface underestimated the experimental value and because the initial conditions for the incoming trajectories were biased towards low-impact parameter collisions with the terminus of the alkyl chain.

Taking account of all factors above, leads to a conclusion that an upper limit on the quantum yield of OH from $O(^1D)$ which reaches the liquid surface of is 3 %. This is comparable to the limit proposed by Park and Wiesenfeld of ~ 3 % in the gas-phase for reaction of $O(^1D)$ with hydrocarbons CH_4, C_2H_6, C_3H_8 and $C(CH_3)_4$ [26]. This amount is not large enough to apply any sort of correction factor and will be thought of as negligible.

Further proof may be necessary given that there are considerable uncertainties in the quantities involved in this estimation and in itself may not be sufficient to exclude $O(^3P)$ entirely. However, the very hot $O(^3P)$ speed distribution may prove even more

decisive. It is known from the molecular-beam experiments of the Minton group that the great majority of the OH produced from O(^{3}P) occurs via a direct, impulsive scattering mechanism [37, 38, 41]. The product speed distributions have been matched to a simple, single-collision model of the scattering dynamics, allowing an effective mass to be deduced that faithfully reproduces momentum transfer to the surface [38, 41]. The sharply-peaked, near-specular angular distributions have also been characterized empirically.

Consequently, it is predicted that the expected appearance profiles for OH produced from O(^{3}P) result from a direct impulsive reaction. This procedure has also been described previously. It includes the geometric averaging and Monte-Carlo sampling from the correct in-going O(^{3}P) speed distribution from N_2O photolysis (as described in appendix 1) [45], but now rather than the Maxwellian product velocity distributions assumed above, the product speed and angular distributions from the Minton kinematic model are imposed.

The results of these simulations have been included in figures 4.3 and 4.4. From this figure, it is very clear that the predicted OH arrival times from O(^{3}P) are much too early to match the observed rising edges and peaks of the OH signals from O(^{1}D) . This is true even for the fastest, higher-*N*′ profiles, which are already unlikely to be the products of O(^{3}P) reactions (as O(^{3}P) produces low rotational products). It is therefore concluded that on dynamical grounds it is very unlikely that O(^{3}P) is responsible for any reasonable quantity of the OH which has been observed.

4.5.3: Assignment of gas-phase mechanisms to collected results

From all the data collected, it may now be possible to assign components of the observed OH in the gas-liquid interfacial reaction to some of the mechanisms proposed previously for the reaction of O(^{1}D) with hydrocarbons in the gas phase. It is important to remember that this assignment is used as an indication as to which mechanisms are possible, which can definitely not occur, and which may be more likely than others based on the data collected.

The bi-modal rotational distributions, (figure 4.6) of OH generated from reaction of $O(^1D)$ with the squalane surface, are certainly similar in appearance to those collected in the gas-phase experiments for small hydrocarbons. Unlike the gas-phase experiments (summarised in section 4.2), the contribution from the colder component is not likely, *a priori*, to occur as a result of statistical insertion. This is due to the fact that squalane has 270 vibrational modes. This would make the lifetime for complete internal vibrational relaxation much too long to reasonably be possible. Stephenson and co-workers calculated the lifetime required in the gas-phase for IVR of methane [18, 20] to be 5 ps. If this were extrapolated from a small molecule the size of methane to one the size of squalane, it is clear that the vibrationally excited alcohol or ether formed by insertion of $O(^1D)$ into squalane would lose energy to the surrounding liquid on a very long timescale as would be required for complete statistical redistribution if energy is randomised over a large number of modes. This means that even if the intermediate lived for this long time, it is unlikely that the OH would manage to escape the liquid surface again.

When trying to identify possible sources of the rotationally cold OH, it must be noted that a significant proportion is translationally hot. The appearance profiles in figure 4.1, or their flux equivalents in figure 4.2, shows that $N' = 1$ is the dominant product level of the three investigated even at the earliest delay of 4 μs.

This is confirmed in the excitation spectra, shown in figure 4.4. The low- N' component of the distribution is found to be ~30% of the total population even at the earliest pump-probe delay of 4 μs (Table 4.3). At this delay, a thermalised (300 K) distribution of speeds would make virtually no contribution and it is predicted that the average speed would be nearer 3000 m s^{-1} as shown in figure 4.3.

The most plausible source of translationally hot, rotationally cold OH is the direct abstraction mechanism. Its proposed backscattered angular distribution would tend to promote direct escape back into the gas phase. However, even if the direct abstraction mechanism progressed and forward-scattered in the frame of the surface and resultingly suffered a secondary collision, we know from our own independent measurements of scattering of translationally hot OH from a squalane surface that the

survival probability is quite high (50-70%) [34, 46]. However, collisions of this type would tend to promote some T-R conversion, which could shift the balance of the rotational distribution towards a higher N'. This point is discussed further in Chapter 6.

The hotter temperature component, which accounts for the majority of the observed OH (~ 70 %) at short delays (Table 4.3), but decreases relatively for slower molecules, is naturally assigned to the non-statistical insertion mechanism as it is a translationally and rotationally hot component. This has been widely discussed in terms of the gas-phase studies presented in section 4.2. The relatively rough surface structure of the squalane predicted in molecular dynamics (MD) simulations [6, 43] makes it quite plausible that some $O(^1D)$ atoms would encounter strands of a squalane protruding into the vacuum which could allow the rapid, non-statistical decay characteristic of the gas-phase to take place. The rotational temperatures of several thousand K that are found here in the hotter component (Table 4.3) are also broadly compatible with those found by others for this component in the gas-phase reactions. This is further evidence for the presence of this mechanism. The stripping mechanism described cannot necessarily be ruled out for this component because, other than some shift in the balance of the fraction of secondary encounters, which would be very high for a stripping mechanism, the observed product–state characteristics would be similar.

OH and squalane secondary collisions could also produce a minor but significant fraction of translationally and rotationally cold molecules, with a speed distribution that is empirically compatible with a TD simulation at 300 K. It is possible that an abstraction-secondary collision mechanism contributes partly to the significant amount of rotationally and translationally colder molecules that appear at longer delays as shown for $N = 1$ in figure 4.1.

Cooling of the translational or rotational distribution due to such secondary encounters would provide a source of rotationally and translationally cold OH. The initial reaction that creates the OH could be the non-statistical or stripping mechanisms or, an abstraction. Inspection of figure 4.3 suggests that the longer-time tail that is mostly confined to $N' = 1$ beyond ~ 20 μs in figure 4.1 would be consistent

with a significant underlying contribution from a 300 K TD distribution. This component is naturally suppressed, but still significant, once transformed to flux in figure 4.2. Since a definite yield of cold OH can still be seen, and no obvious direct mechanistic source can be found if the arguments above rule out statistical insertion then secondary interactions with the surface must necessarily be responsible for this component.

The inclusion of secondary interactions may be surprising but in a related study on F + squalane, Nesbitt and co-workers found similar results for the HF products detected by infrared absorption [47]. F + hydrocarbon reactions are well established to be prototypical abstraction reactions and not subject to multiple mechanisms in the gas phase. Resultingly, the bimodal rotational distributions and the strong positive correlation between HF product rotation and translation were taken to be clear evidence of secondary interactions at the surface. This argument was at least partly supported by the QM/MM modeling of the scattering dynamics using optimized semi-empirical Hamiltonians of Layfield and Troya [48].

4.5.4: Comparison with previous O(^{3}P) + liquid squalane measurements

It is interesting to compare the data collected for the excited state of oxygen O(^{1}D) to previously collected data [4] for the ground state O(^{3}P) of oxygen. New data pertaining to this is presented in Chapter 6. On reaction with the squalane surface both of these species produce OH. In the O(^{3}P) experiments, the Boltzmann plots were found to conform to a single temperature which corresponded to just above thermal in v' = 0 and just below thermal in v' = 1. This is in stark contrast to the data collected here, where two distinct temperatures were present, one roughly thermal and the other much hotter. This is almost certainly due to the fact that the excited state of oxygen contains more energy than the ground state to begin with. During a collision, this means that energy left over may be used for rotation.

Looking to the population data (summarized in table 4.3), it can be seen that the upper temperature is very hot. When comparing O(^{1}D) to O(^{3}P) (discussed further in Chapter 6), the upper temperature is much higher. This is unsurprising as the pre-collision properties of O(^{1}D) and O(^{3}P) are different. The O(^{1}D) has a much higher translational

energy (~ 180 kJ mol^{-1}) than $O(^3P)$ (15.8 kJ mol^{-1}), therefore it is reasonable that during collision with the same surface that more energy is available for rotation in the OH products generated from $O(^1D)$ as they had more energy pre-collision. What is more interesting is that without any forcing, the lower temperature for both $O(^3P)$ and $O(^1D)$ is calculated to be around 300 K. This is surprising due to the initial differences in pre-collision translational energy. This is strong evidence for a thermalisation mechanism although the evidence may not yet be sufficient to say that full trapping takes place. Further discussion on new $O(^3P)$ data is presented in Chapter 6.

4.6: Conclusions

- These are the first measurements of the reaction of $O(^1D)$ with a liquid hydrocarbon surface.
- Appearance profiles showed a much larger population in N = 1 than higher levels, indicating a significant rotationally cooler component, even for faster products.
- Presence of population in higher levels showed the presence of a more rotationally excited component that is confined to early delays and hence translationally hot products.
- There is a strong overall positive translational-to-rotational energy correlation.
- Excitation spectra showed that all scattered OH was much hotter than thermal but appeared to cool as the delay progressed.
- Presence of a dual temperature was confirmed by constructing Boltzmann plots and fitting to two temperatures. The cooler temperature component was confirmed to be thermal within error margins and the hotter temperature component was found to be much hotter than thermal but had larger errors present in the measurement. The fraction of molecules in the colder temperature was 30 % at early delays, and increased to 44 % at later delays
- The OH yield which escaped the surface was calculated to be < 3%, this agreed well with previous estimates of ~ 3 % for larger molecules.
- The fraction of OH products from $O(^3P)$ molecules generated in the photolysis of N_2O present in our results were calculated, despite unknown quantities, this was estimated as ~ 1 %
- Mechanisms identified for comparable gas-phase reaction were assigned as far as possible to the results. Statistical insertion was ruled out due to long times needed for vibrational relaxation to occur across a large number of nodes. Non-statistical insertion was proposed as a mechanism for the cooler rotational temperature component while abstraction was proposed as a possible mechanism for the hotter rotational temperature component.
- Although evidence was not as strong, presence of the stripping mechanism could not be ruled out as a contributor to the higher rotational temperature.

- Secondary encounters of OH with the liquid surface were also deemed to be present and responsible for a translationally and rotationally cold component most easily observed in lower *N* levels.

4.7: References

1. F. Ausfelder and K. G. McKendrick, *Prog. React. Kinet. Mech.*, 2000, **25**, 299-370.
2. F. Ausfelder, H. Kelso and K. G. McKendrick, *Phys. Chem. Chem. Phys.*, 2002, **4**, 473-481.
3. H. Kelso, S. P. K. Kohler, D. A. Henderson and K. G. McKendrick, *J. Chem. Phys.*, 2003, **119**, 9985-9988.
4. S. P. K. Kohler, M. Allan, H. Kelso, D. A. Henderson and K. G. McKendrick, *J. Chem. Phys.*, 2005, **122**, 024712.
5. S. P. K. Kohler, M. Allan, M. L. Costen and K. G. McKendrick, *J. Phys. Chem. B*, 2006, **110**, 2771-2776.
6. S. P. K. Kohler, S. K. Reed, R. E. Westacott and K. G. McKendrick, *J. Phys. Chem. B*, 2006, **110**, 11717-11724.
7. M. Allan, P. A. J. Bagot, M. L. Costen and K. G. McKendrick, *J. Phys. Chem. C*, 2007, **111**, 14833-14842.
8. M. Allan, P. A. J. Bagot, S. P. K. Kohler, S. K. Reed, R. E. Westacott, M. L. Costen and K. G. McKendrick, *Phys. Scr.*, 2007, **76**, C42-C47.
9. M. Allan, P. A. J. Bagot, R. E. Westacott, M. L. Costen and K. G. McKendrick, *J. Phys. Chem. C*, 2008, **112**, 1524-1532.
10. C. Waring, P. A. J. Bagot, M. T. Raisanen, M. L. Costen and K. G. McKendrick, *J. Phys. Chem. A*, 2009, **113**, 4320-4329.
11. C. Waring, P. A. J. Bagot, J. M. Slattery, M. L. Costen and K. G. McKendrick, *J. Phys. Chem. A*, 2010, **114**, 4896-4904.
12. C. Waring, P. A. J. Bagot, J. M. Slattery, M. L. Costen and K. G. McKendrick, *J. Phys. Chem. Letts.*, 2010, **1**, 429-433.
13. B. J. Finlayson-Pitts and J. N. Pitts Jnr, *Chemistry of the Upper and Lower Atmosphere*, John Wiley & Sons., 2000.
14. H. Okabe, *Photochemistry of Small Molecules*, John Wiley & Sons, 1987.
15. Y. Rudich, Y. Hurwitz, G. J. Frost, V. Vaida and R. Naaman, *J. Chem. Phys.*, 1993, **99**, 4500-4508.
16. J. Schlutter, R. Schott and K. Kleinermanns, *Chem. Phys. Lett.*, 1993, **213**, 262-268.
17. R. D. Vanzee, J. C. Stephenson and M. P. Casassa, *Chem. Phys. Lett.*, 1994, **223**, 167-172.
18. R. D. Vanzee and J. C. Stephenson, *J. Chem. Phys.*, 1995, **102**, 6946-6948.
19. J. J. Lin, J. Shu, Y. T. Lee and X. Yang, *J. Chem. Phys.*, 2000, **113**, 5287-5301.
20. C. C. Miller, R. D. van Zee and J. C. Stephenson, *J. Chem. Phys.*, 2001, **114**, 1214-1232.
21. J. Shu, J. J. Lin, C. C. Wang, Y. T. Lee, X. M. Yang, T. L. Nguyen and A. M. Mebel, *J. Chem. Phys.*, 2001, **115**, 7-10.
22. R. L. Gross, X. H. Liu and A. G. Suits, *Chem. Phys. Lett.*, 2003, **376**, 710-716.
23. M. A. Blitz, T. J. Dillon, D. E. Heard, M. J. Pilling and I. D. Trought, *Phys. Chem. Chem. Phys.*, 2004, **6**, 2162-2171.
24. H. F. Chen, C. W. Liang, J. J. Lin, Y. P. Lee, J. F. Ogilvie, Z. F. Xu and M. C. Lin, *J. Chem. Phys.*, 2008, **129**, 174303.
25. Paraskev.G and Cvetanov.Rj, *J. Chem. Phys.*, 1970, **52**, 5821.
26. C. R. Park and J. R. Wiesenfeld, *J. Chem. Phys.*, 1991, **95**, 8166-8177.
27. M. Brouard, H. M. Lambert, C. L. Russell, J. Short and J. P. Simons, *Faraday Discuss.*, 1995, **102**, 179-192.
28. M. Brouard, H. M. Lambert, J. Short and J. P. Simons, *J. Phys. Chem.*, 1995, **99**, 13571-13581.
29. R. Schott, J. Schlutter, M. Olzmann and K. Kleinermanns, *J. Chem. Phys.*, 1995, **102**, 8371-8377.
30. X. M. Yang, *Phys. Chem. Chem. Phys.*, 2006, **8**, 205-215.
31. P. Felder, B. M. Haas and J. R. Huber, *Chem. Phys. Lett.*, 1991, **186**, 177-182.

32. L. L. Springsteen, S. Satyapal, Y. Matsumi, L. M. Dobeck and P. L. Houston, *J. Phys. Chem.*, 1993, **97**, 7239-7241.
33. J. C. Luque and D. R. Crossley, SRI International, 1999.
34. P. A. J. Bagot, C. Waring, M. L. Costen and K. G. McKendrick, *J. Phys. Chem. C*, 2008, **112**, 10868-10877.
35. Y. Matsumi and A. M. S. Chowdhury, *J. Chem. Phys.*, 1996, **104**, 7036-7044.
36. S. Nishida, K. Takahashi, Y. Matsumi, N. Taniguchi and S. Hayashida, *J. Phys. Chem. A*, 2004, **108**, 2451-2456.
37. D. J. Garton, T. K. Minton, M. Alagia, N. Balucani, P. Casavecchia and G. G. Volpi, *Faraday Discuss.*, 1997, **108**, 387-399.
38. D. J. Garton, T. K. Minton, M. Alagia, N. Balucani, P. Casavecchia and G. G. Volpi, *J. Chem. Phys.*, 2000, **112**, 5975-5984.
39. R. P. Baker, M. L. Costen, G. Hancock, G. A. D. Ritchie and D. Summerdeld, *Phys. Chem. Chem. Phys.*, 2000, **2**, 661-664.
40. C. Waring, P. A. J. Bagot, M. W. P. Bebbington, M. T. Raisanen, M. Buck, M. L. Costen and K. G. McKendrick, *J. Phys. Chem. Letts.*, 2010, **1**, 1917-1921.
41. J. M. Zhang, D. J. Garton and T. K. Minton, *J. Chem. Phys.*, 2002, **117**, 6239-6251.
42. B. H. Wu, J. M. Zhang, T. K. Minton, K. G. McKendrick, J. M. Slattery, S. Yockel and G. C. Schatz, *J. Phys. Chem. C*, 2010, **114**, 4015-4027.
43. D. Kim and G. C. Schatz, *J. Phys. Chem. A*, 2007, **111**, 5019-5031.
44. G. Li, S. B. M. Bosio and W. L. Hase, *J. Mol. Struct.*, 2000, **556**, 43-57.
45. M. Brouard, A. P. Clark, C. Vallance and O. S. Vasyutinskii, *J. Chem. Phys.*, 2003, **119**, 771-780.
46. C. Waring, K. L. King, P. A. J. Bagot, M. L. Costen and K. G. McKendrick, *Phys. Chem. Chem. Phys.*, 2011, **13**, 8457-8469.
47. A. M. Zolot, P. J. Dagdigian and D. J. Nesbitt, *J. Chem. Phys.*, 2008, **129**, 194705.
48. J. P. Layfield and D. Troya, *J. Chem. Phys.*, 2010, **132**, 134307.

Chapter 5: Collision Dynamics of 'hot' OH radicals with atmospherically relevant liquids: separating the thermal desorption channel

This chapter will outline the experimental study of the interactions of rotationally excited OH radicals with liquid surfaces of atmospheric relevance. This work will be compared to that completed previously [1, 2] using a rotationally near-thermal source of OH radicals. Next, an introduction to the chemistry of the OH radical in the atmosphere will be discussed followed by a summary of pertinent previous experimental studies of oxidation of liquids used as proxies for atmospheric aerosols, focussing on reactive uptake measurements.

5.1: Introduction to hydroxyl radical chemistry

The OH radical is mostly formed in the troposphere from $O(^1D)$ which is a product of the photo-dissociation of ozone (equations 5.1 and 5.2). The wavelength of light typically needed for photolysis is between 280 nm – 320 nm. This is because over 320 nm would produce a ground state oxygen atom, and anything less than 280 nm is absorbed makes O_2 which has a $^3\Sigma$ state. Transitions to this state are forbidden according to state selection rules (discussed further in section 3.4). The excited state ($O(^1D)$) form of oxygen is necessary to overcome the high barrier to reaction in equation 5.2. Ground state oxygen, $O(^3P)$, would not have the 119 kJ mol^{-1} [3] required to overcome the reaction barrier. As $O(^1D)$ has 190 kJ mol^{-1} the overall reaction is still exothermic and therefore favourable.

$$O_3 + h\nu\ (280\ nm < \lambda > 320\ nm) \rightarrow O_2\ (^1\Delta) + O(^1D) \qquad \text{Equation 5.1}$$

$$O(^1D) + H_2O \rightarrow 2OH \qquad \text{Equation 5.2}$$

The OH radicals produced by these reactions are the most dominant oxidant species in the troposphere, they are known to oxidise the widest class of molecules including

alkanes, alkenes and aromatic VOC's. They are also known to oxidise species five orders of magnitude faster than a comparative oxidant species such as NO_3 [4]. These qualities are the reason that OH is so important. This fact may have initially been surprising to many as the average tropospheric concentrations of OH are of the order of 10^6 molecule cm^{-3} which is low when compared to other oxidant species such as the nitrate radical [4]. The lifetime of the OH radical is also very short at ~ 0.01 - 1 s which has been well characterised previously [5].

One of the OH radical's main roles in the troposphere (and the one relevant to the scope of this work) is to cause oxidation in aerosols, known as aging. Some aerosols are proposed to have a micelle-like structure [6] with a hydrophilic core and an organic outer hydrophobic layer. Radicals - such as OH - cause oxidation within the outer layer as shown in figure 5.1 which makes the aerosols more hydrophilic. This, in turn, enables them to become better cloud condensation nuclei. Without this aging action, aerosols would not gather water causing raindrops in clouds to be much smaller in general and may even be too small to fall as rain. This may already be evident as it is estimated that 50-60 % of the world is covered in clouds at any one time yet only 10 % are rain clouds [6]. A decrease in OH radical concentration or an increase in pollution could, in time, lead to droughts and crop failure in many polluted areas. A typical sequence of OH radical initiated reactions is shown in figure 5.2.

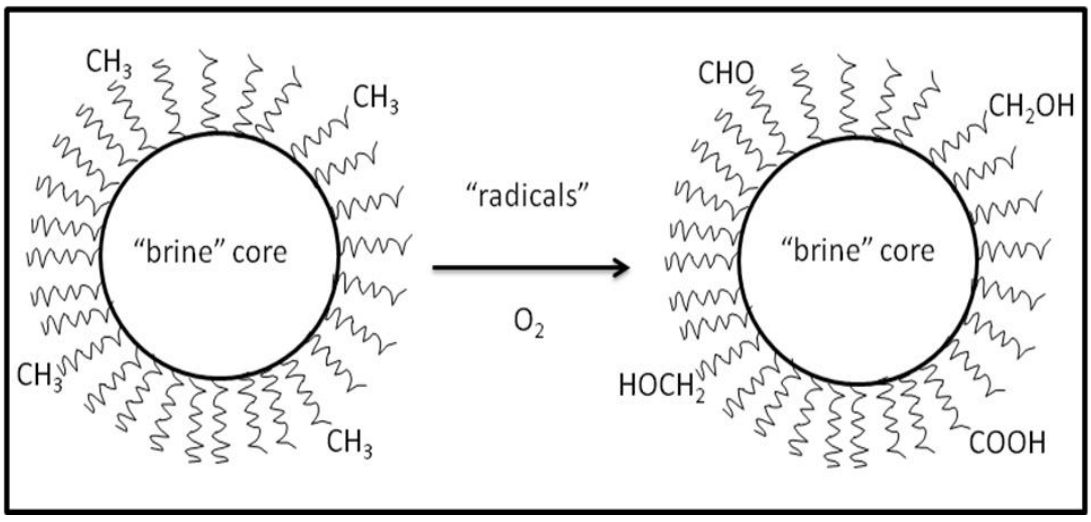

Figure 5.1: Schematic adapted from [7], showing the micelle structure of aerosols, during aging. It can be seen that the structure is hydrophobic with hydrocarbon tails pointing outward. Aging, as shown ensures the aerosol becomes more hydrophilic.

It is for all these reasons that the OH radical is such an important species, yet the heterogeneous interactions of OH with aerosol particles are poorly understood. This is mainly because heterogeneous gas-liquid interactions are poorly studied in general, as discussed in Chapter 1. This main aim of this chapter will be to explore the mechanistic detail of the elementary step of the encounter of OH radicals with hydrocarbon liquid surfaces. These liquid surfaces used in this chapter will serve as proxies for atmospheric aerosols but temperatures and collision energies used in this set of experiments are much higher than those present in the troposphere. The results collected are useful to compare with atmospheric chemistry processes and may indicate the first step in atmospheric aging of aerosols but are not directly comparable due to the differing conditions between the experiments and the troposphere.

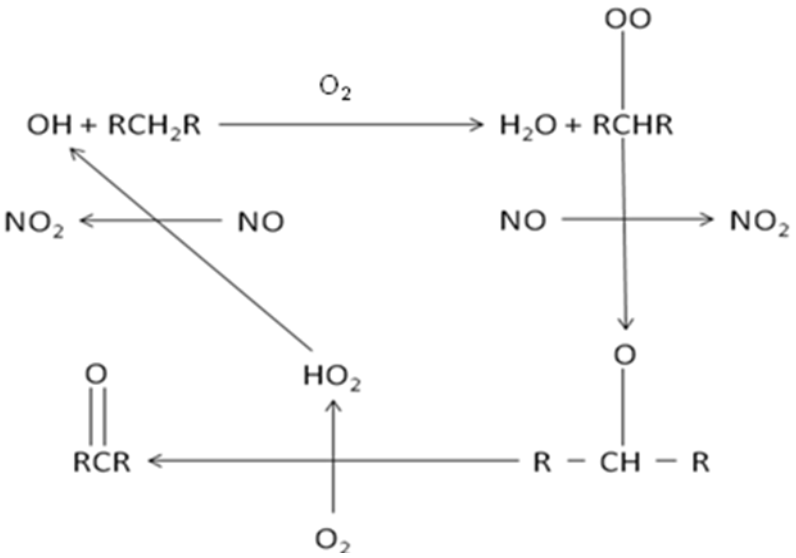

Figure 5.2: A typical sequence of OH radical initiated elementary reactions, in which the hydrophobic hydrocarbon portion of an aerosol is aged.

5.2: Past experimental measurements of OH uptake coefficients

The role of OH radicals in the atmosphere is a very complex one. To better understand the chemistry it is clear that many studies which encompass multiple fields of chemistry will have to be undertaken. This will include both field measurements and simplified laboratory studies, where a wide variety of aerosols proxies may be used.

These can include organic liquids in many forms such as liquid droplets, films waxes and self assembled monolayers (SAM's are discussed further in Chapter 1).

In the past many studies have been carried out on both homogeneous gaseous reactions and heterogeneous gas liquid reactions. A number of reviews summarise these studies well [8-15].

Typical measurements include the ability of the surface to collect water (important for aerosol aging) and the reactive OH uptake coefficient, γ. This uptake co-efficient is defined as the reactivity per collision, and is important to this work. The reactive uptake coefficient is measured in two main ways: either by monitoring the rate of removal of the particle phase, for example by mass spectrometry, or by monitoring the loss of gas-phase species (in this work OH, monitored by LIF).

The Donahue group in collaboration with Robinson [16] investigated the reactivity of OH radicals with motor oil aerosols which consisted of a mixture of hopanes, steranes and n-alkanes in a smog-style reaction chamber. OH was generated from 2,3-dimethyl-2-butene (TME) and ozone while products were detected by chemical ionisation mass spectrometry (CIMS). Uptake coefficients on these aerosols ranged from 0.1 – 8. In a similar study [17] the reactive uptake coefficient of OH with n-hexacosane aerosol particles was measured γ was 1.04 ± 0.21. In most of the experimental studies described, it was not possible to exclude secondary reactions from the measurement of the uptake coefficient, meaning that γ could be more than 1. Values of > 1 indicate at least some secondary reactions and are not wholly representative of a primary encounter with the liquid surface.

Moussa and Finlayson-Pitts [18] also performed an experiment in a reaction cell, where gas was continuously flowed. Where the reaction uptake coefficient was measured for OH (generated from isopropyl nitrate (IPN) reacting with a terminal alkene SAM on a solid wall (7-octenyltrichlorosilane, C_8 SAM), detection of both loss of the reactant SAM and formation of surface products were monitored by an infrared spectrometer (FTIR). The average uptake coefficient (of 8 experiments) was determined to be 1.1 ± 0.9. The error in each individual experiment was often larger than the measurement. This may be attributed to the manner in which γ was determined. This was accomplished by using FTIR to monitor the intensities of two

organic nitrate peaks at 1634 cm^{-1} and 1280 cm^{-1}. Yet it was noted that several different reaction pathways existed, it is possible that these different pathways contribute to the peaks monitored in different quantities, all of which cannot be accounted for, increasing the uncertainty in each measurement.

One of the most commonly used techniques for this type of work is the flow tube; this is where gas is flowed through a tube which has been coated in the surface of interest. The exiting gas flow is measured and γ is subsequently calculated. Molina and co-workers have carried out studies of reactive uptake of OH by a variety of surfaces [19, 20] using this method. The experiments were performed using a flow tube containing both inorganic and organic surfaces at varying humidity. OH was generated either from NO_2 or O_2 and detection was performed by CIMS. The uptake coefficients were found to be: halocarbon wax – 6 x 10^{-4}; paraffin wax – 0.34; vinyl terminated monolayer – 0.60; methyl terminated monolayer – 0.29; pyrene – 0.32 and palmitic acid 0.32. The results show that the acid group has very little effect on the uptake coefficient (eg palmitic acid vs. paraffin wax) while SAMs show similar reactivity to more random surfaces. The results also show increased reactivity in unsaturated surfaces when compared to saturated ones.

D'Andrea and co-workers [21] discovered that for aqueous inorganic salts, reactivity appeared to be much reduced. OH was produced from a corona discharge in an argon/hydrogen peroxide/water mixture and reflection/absorption infrared spectroscopy (RAIRS) was used to monitor OH levels This was in keeping with the results of Molina [19, 20] who found aqueous reactivity much lower than for organic liquids. The measured uptake coefficients were of the order of ~ 3-6 x 10^{-3}. They also performed experiments on methyl and vinyl terminated SAMs where γ was not measured finding that the reaction at the unsaturated monolayer occurred more readily than on the saturated counterpart. Degradation of the unsaturated components occurred on short timescales, it was proposed that this was due to radical chain polymerisation which initiated from OH insertion into the vinyl unit.

Abbatt and co-workers [22, 23] also used a flow tube type experiment, this time to measure the reactive uptake coefficient of OH by bis-(-2-ethylhexyl)sebacate (BES – $C_{26}H_{50}O_4$). BES is a saturated di-ester which is a proxy for an atmospheric aerosol which

has undergone some aging (known as a secondary organic aerosol or SOA). Again O_3 was used as the source of OH radicals but in this case loss of initial radicals was monitored by an Aerodyne aerosol mass spectrometer (AMS). In this case γ was found to be 1.3 ± 0.4, which indicates that a secondary reaction mechanism must be present as for a primary mechanism γ < 1. In this study it was also noted that the secondary reactions included volatilization of reaction products which could account for up to a 10 % mass loss [23].

Abbatt and Cooper [24] also performed a much earlier experiment on the reactive uptake coefficient of OH (generated from the reaction of fluorine and water) by water ice, NH_4HSO_4 and $(NH_4)_2$-SO_4. The experiment used a flow tube set-up but resonance fluorescence was used to detect the OH and thus monitor γ. γ was found to be small in all cases; 0.03 ± 0.02 for water ice and < 0.03 for both NH_4HSO_4 and $(NH_4)_2$-SO_4 although this value was found to increase greatly (to γ > 0.2) with the addition of a small amount of 1-hexanol. This study shows that reactive uptake coefficients for OH are greatly increased when a hydrocarbon is present.

A comparable experiment also using a flow tube to measure the reactive uptake coefficient of OH by BES was performed by Hearn and Smith [25] where HONO was used as the OH source and CIMS was used to measure particle loss. In this case γ was found to be 2 ± 0.6, again showing that secondary reactions are involved in this process. In unpublished work [26] Smith and co-workers have used the same experimental method to measure γ of OH radicals from squalane, squalane and oleic acid. The results were γ = 0.28 ± 0.04 for squalane; >1 for squalane and 0.4 ± 0.03 for oleic acid.

McNeill and co-workers [27] measured the reactive uptake coefficient of OH by palmitic acid thin films. Experiments were performed in a continuous flow reaction chamber using $O(^1D)$ plus water to generate OH. CIMS was employed to monitor palmitic acid particle loss. γ was found to be 0.8 – 1 for pure palmitic acid. For palmitic acid coated aqueous particles γ = 0.05 ± 0.01 and for palmitic acid coated salt particles (mimicking sea-salt aerosols) γ = 0.3 ± 0.1. This study shows that reactivity drops from pure hydrocarbons to both aqueous and sea salt particles.

In one of the most recent studies by Renbaum and Smith [28] a flow tube was employed to measure the reactive uptake coefficient of OH and Cl radicals by squalane and brassidic acid. In this case, liquids were heated and then cooled to form super-cooled liquid droplets. OH radicals were generated from ozone (O_3) and particle reaction was measured by chemical ionisation mass spectrometry (CIMS). Two different sizes of flow tube (small and large) were used to measure γ for squalane which was found to be 0.22 and 0.39 respectively for the flow tube sizes.

Wilson and co-workers [29, 30] have carried out two studies, one using a flow tube reactor with high OH concentration (1 x 10^{10} molecules cm^{-3}) [30] and the other using a continuous flow stirred tank with low OH concentrations (1 x 10^{8} molecules cm^{-3}) [29]. In these experiments OH is generated from ozone and detection is performed by a high resolution time of flight mass spectrometer. These highly sensitive experiments allow aging to be observed in a step-wise manner as squalane particles are oxidised by OH from sq in the sequence: sqO, sqO_2, sqO_3 etc. It was determined that as the aging process continues, fragmentation occurs leading to increasing loss due to volatilization. This may be atmospherically relevant as greater loss due to volatilization may occur in the troposphere as oxidation occurs. This was also noted by Abbatt et al [23]. γ was determined to be 0.3 ± 0.07 for the flow tube and 0.51 ± 0.10 for the reaction tank. A summary of relevant γ values is given in table 5.1. The differences in these measurements were attributed to the different OH concentrations. Although the experimental set-ups were very different, the uptake coefficients are surprisingly similar. The authors attributed this to an apparent acceleration of squalane loss at highly oxidised particles in the low concentration OH experiments. Therefore the uptake co-efficient was a measure of both the primary encounter and a secondary loss process. It was postulated that these loss processes had less of an influence in the higher concentration OH experiment.

In the following experimental technique described, LIF is employed along with low pressure and short times (as described in section 2.4.1) to ensure that only primary encounters are possible meaning that single collision conditions are strictly imposed. This is an advantage in understanding the dynamics of the primary encounter of the OH radical but consequently means that collision energies of the OH radical are much higher and therefore not directly comparable to atmospheric interactions. In addition,

this work is meant to complement the previous studies by using a rotationally hot source of OH and comparing this to previously near-thermal rotational OH temperatures.

Group	Experimental Details	γ value	Reference
Donahue	OH with n-hexacosane	1.04	17
Finlayson-Pitts	OH with terminal alkene SAMs	1.1	18
Molina	OH with Palmitic Acid	0.32	19
D'Andrea	OH with aqueous organic salts	~ 3-6 x 10^{-3}	21
Abbatt	OH with BES	1.3	24
Hearn and Smith	OH with squalane OH with Squalene OH with Oleic Acid	0.28 > 1 0.4	26
McNeill	OH with Palmitic acid coated aqueous particles	0.05	27
Wilsom	OH with squalane (flow tube) OH with squalane (stirred tank)	0.3 0.51	30 29

Table 5.1: Summary of γ values discussed in section 5.2.

5.2.1: Past OH interfacial scattering experiments of the McKendrick group

In the past, within the McKendrick group, experiments on the inelastic scattering dynamics of OH radicals from a variety of organic liquids have been performed. These experiments used HONO as a source of OH radicals. These include the first paper [1] which detailed the interaction of OH with the benchmark liquid hydrocarbon squalane. In addition to this, a further paper [2] was published which included further experiments on three different liquids. PFPE (shown in figure 2.3) was used as a

standard; there are no hydrogens present on PFPE so reactive uptake should not occur. Squalene (shown in figure 2.3) was used as an unsaturated counterpart to squalane to investigate the effect that double bonds have on reactive uptake. Finally oleic acid was used to try and investigate the effects of a further functional group (structure shown in figure 5.3). These experiments were summarised in the thesis of a past student [31] and will be shown alongside new results presented here to illustrate the differences between the scattering of OH generated from HONO and the OH generated from allyl alcohol. Where work presented in a thesis before is shown, this will be noted.

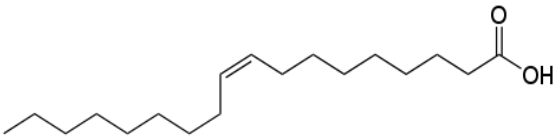

Figure 5.3: Structure of oleic acid.

5.3: Experimental Summary

The broad experimental set-up for this series of experiments is detailed in Chapter 2. In this section details will be presented which are relevant to only this series of experiments. In addition to this, conditions used for the rotationally near-thermal OH will also be detailed as these results will be included for comparison later.

The liquids used have been well described in previous sections (2.5 and 5.2.1), however it is worth noting that in all experiments described in this chapter liquids were at room temperature (297 ± 3 K).

In the rotationally near-thermal OH experiments, the OH radicals were generated from a continuous flow of HONO (equation 5.3) gas precursor in a N_2 carrier gas stream as described in [31].

$$2NaNO_2 + H_2SO_4 \rightarrow 2HONO + Na_2SO_4 \qquad \text{Equation 5.3}$$

The mix of HONO and N_2 was set to maximise OH production. A set pressure of HONO gas (1 ± 0.5 mTorr) was admitted to the chamber continuously, this gas was photolysed (355 nm third harmonic Nd:YAG, 5 mm diameter beam, fluence ~2000 mJ cm^{-2}) at a fixed distance of 9 mm from the liquid surface. The spatial distribution of the OH

produced from HONO has an anisotropy parameter of β = - 0.9 [32]. Therefore a λ/2 wave-plate was used to rotate the polarisation of the beam to vertical and thus maximise the fraction of OH travelling towards the liquid surface. The OH returning from the liquid surface was probed (beam also at 9 mm distance, 2 mm diameter, fluence ~ 500 mJ cm^{-2}) on the $A^2\Sigma^+$ - $X^2\Pi$ (0,0) band which occurs at around 308 nm. OH from HONO was collected using the (0,0) band of OH to avoid saturation problems. This method means that absorption and emission occur at the same wavelengths and it is difficult to mask the emission. Due to these difficulties OH from allyl alcohol was collected on the (1,0) band.

In the rotationally hot OH experiments, the OH radicals were generated by photolysis of a controlled pressure (1 ± 0.5 mTorr) of allyl alcohol. The photolysis beam was produced by an ArF excimer (GAM EX350 or Compex 102 Lambda Physik), with a pulse length of approximately 20 ns. The excimer beam was guided to enter the vacuum chamber and focussed in the interaction region of the chamber. The sizes of the two beams in the centre of the chamber were slightly different: 4 mm x 2 mm in the vertical frame of the laboratory axis for the Compex 102 and 3 mm x 3 mm for the GAM EX350 but to ensure experimental reproducibility, the overall fluence was monitored and kept constant. The laser pulse energy was ~ 5 mJ which corresponds to an average fluence of 150 mJ cm^{-2}. The photolysis beam is effectively unpolarised so anisotropy considerations are not taken into account here [33], it is known that a sufficient fraction of OH radicals generated will recoil towards the liquid surface. As in the HONO experiments, the photolysis beam was 9 mm in distance from the liquid surface. The scattered OH was probed by a counter-propagating probe beam of around 2 mm in diameter (also at a distance of 9 mm). Typical pulse energies of the probe beam were of the order 300 – 400 μJ which corresponds to a fluence of 9 – 12 mJ cm^{-2}. The returning OH was probed on the $A^2\Sigma^+$ - $X^2\Pi$ (1,0) band, which occurs at around 280 nm.

5.3.1: OH properties: differences between rotationally hot and near-thermal OH

The reason for using two different sources to seemingly do the same thing may not be immediately obvious. When OH radicals are generated from a precursor source, the

OH can have many different varying properties such as kinetic and rotational energy. The properties relevant to the two sources of OH used are summarised in table 5.2.

	OH from HONO at 355 nm [32]	OH from allyl alcohol at 193 nm[34]
Average Kinetic energy	54 kJ mol^{-1}	80 kJ mol^{-1}
Speed	2500 m s^{-1}	~ 4300 m s^{-1}
Average Rotational energy	2.49 kJ mol^{-1}	57 kJ mol^{-1}
Rotational temperature	~ 300 K	2050 K

Table 5.2: Properties of OH as generated from each precursor named.

5.4: Experimental Results

5.4.1: Estimate of relative signal sizes and other considerations

At the beginning of this set of experiments, there were factors to consider which would impact the size of the OH signal before experimental testing began. One of these was using the β parameter to estimate the number of molecules which scatter preferentially towards the liquid surface (as discussed in section 2.6). In this case, OH from allyl alcohol has an isotropic distribution [34] which means that as allyl alcohol is photolysed at 193 nm (table 2.1), the photolysis laser used is an excimer with an unpolarised beam. Using any beam with a species which had a β parameter of zero would produce an isotropic distribution of photo-fragments. This means that using Monte Carlo (MC) simulations and inputting real values from the experiment such as beam diameter and distance from the liquid wheel, it can be expected that 11.2 % of OH generated from allyl alcohol would interact with the liquid wheel.

In the case of OH from HONO, the β parameter (-0.9) is close to the limiting case of -1. This means that with a vertically polarised photolysis beam ca. ~ 50% of the HONO

fragments should be travelling in the direction of the liquid wheel. Using the same MC simulations with the correct beta parameter and beam diameter from the HONO experiment, an estimate of the percentage of molecules which will interact with the liquid surface can be calculated. This number is slightly higher than with allyl alcohol and 12.5% of the OH generated from HONO is expected to interact with the liquid surface. It should be noted that this factor only accounts for the molecules that reach the liquid surface and does not take into account that some of these will not reach the probe laser to be detected.

Other factors which may affect the signal sizes observed are the absorption cross sections of HONO at 355 nm and allyl alcohol at 193 nm as well as their quantum yields. Allyl alcohol has an absorption cross section of 1×10^{-19} cm^2 $molecule^{-1}$ [33] while HONO has an absorption cross section of 6×10^{-19} cm^2 [35]. These cross sections are in the same range and will probably not have a great effect on observed signal. The OH quantum yield for HONO is 1; meaning that for every photon absorbed a photochemically active OH molecule is created. The OH quantum yield for allyl alcohol is 0.23 meaning that one photo-chemically active molecule is created for just over every four photons absorbed. This is a disadvantage for allyl alcohol.

Finally, perhaps the most influential factor on the relative signal sizes is the purity of the gases used. For allyl alcohol 1 mTorr of pure (≥ 99 %) sample was admitted to the chamber while for HONO a 1 mTorr mixture of HONO gas and high purity nitrogen was used. Measurement of the LIF signal on a particular branch was used to maximise HONO production, despite this the quantity of HONO in the mixture is not quantified. This will likely mean that there is less HONO than allyl alcohol in the experimental chamber but the extent of this is unknown.

These factors show that there may be differences in the relative quantities of OH produced from HONO and from allyl alcohol. As the experiments are not entirely equal direct quantifications should not be attempted but it should still be very useful to compare data quantitatively and compare similarities and differences.

5.4.2: Scattered OH signal verification

In the experimental set-up described previously (in Chapter 2), the molecule which is detected is OH. When using allyl alcohol, OH is generated during the photo-dissociation process. This raises the question of how to distinguish between the initially generated OH and the OH which has returned from the liquid surface? To answer this question, a few new terms will be introduced. Pre-collision OH refers to the nascent OH generated from photo-dissociation of the pre-cursor molecule. Post-collision OH is the OH which has been generated and has interacted with the liquid surface then returned to the probe volume and been detected.

To separate the pre- and post-collision OH, a separate experiment must be performed alongside each liquid data collection. This experiment was named a 'no-wheel' procedure. This experiment entailed collection of data in separate runs just prior to or just after collection from a liquid surface experiment, the only difference being the removal of both the liquid surface and the stainless steel wheel. This enabled all parameters, such as base pressure, laser power and pressure of precursor gas to remain stable while ensuring that all 'background' signals – such as scattered fluorescence from both lasers or residual fluorescence from molecules stuck on the chamber walls, windows or wheel assembly – was accounted for.

In past experiments [1], the entire copper bath assembly was removed, and replaced with a blank flange. This may have affected background signals in two ways: the wheel assembly may have contained small molecules adsorbed onto the surface. Also removing the assembly from the vacuum and exposing to atmosphere may have increased the coverage of these small molecules. Removal of only the stainless steel wheel from the vacuum chamber ensures that this variability is minimised as far as possible.

When the no-wheel experiment is performed, a smooth decay curve is obtained from the pre-collision OH from photo-dissociation of allyl alcohol as shown in figure 5.4. When the liquid covered stainless steel wheel is returned to the chamber, another profile is obtained which contains information on both the allyl alcohol photo-dissociation (pre-collision) and any OH which may return from the liquid surface (post-collision). By subtracting the no-wheel contribution from the data collected with the

wheel in place it is possible to isolate a signal which originates only from the post-collision OH which has returned from the liquid surface (figure 5.5). For the case of allyl alcohol this has been performed alongside each set of data in each type of experiment for both the appearance profiles and the excitation spectra. This is shown more clearly in figures 5.4 and 5.5.

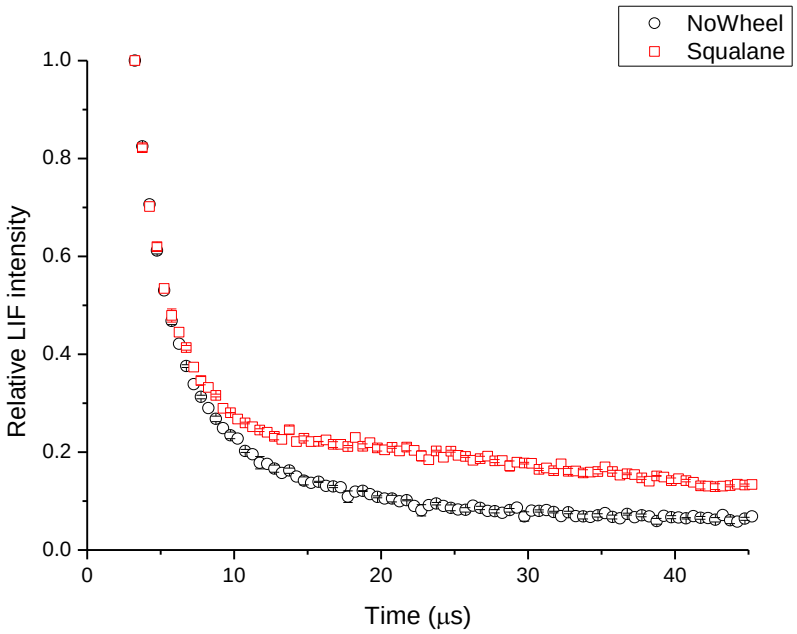

Figure 5.4: The LIF $Q_1(1)$ signal of OH scattered from representative liquid squalane (shown out to 45 μs for reference) and comparatively with no wheel present. No-wheel is plotted as open black circles and squalane as open red squares. The traces shown are averages of several scans. Error bars shown are the standard 1σ error in the mean, but are generally smaller than the symbols. The post-collision OH signal can be seen in the PFPE trace beginning below ~ 5 μs, as it separates from the no-wheel trace.

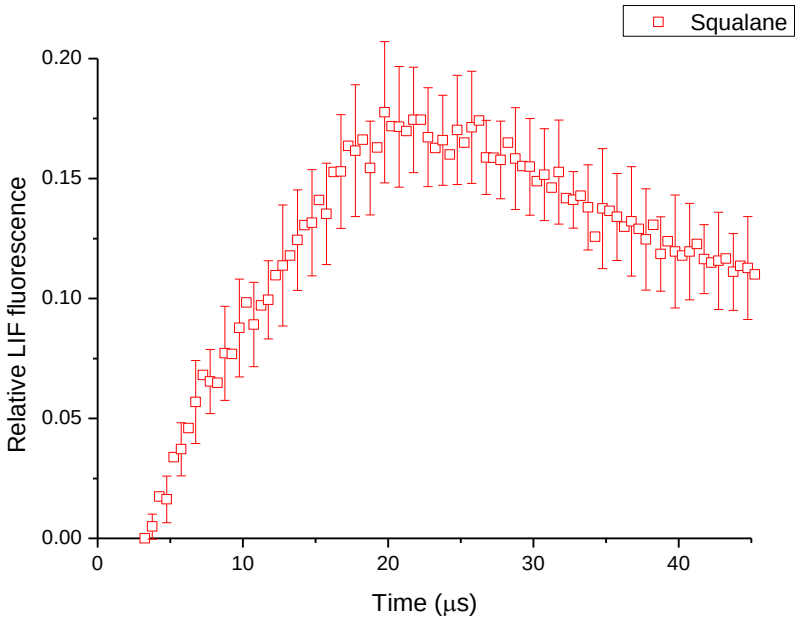

Figure 5.5: The OH LIF $Q_1(1)$ signal from squalane shown after subtraction of the no-wheel $Q_1(1)$ LIF signal. This gives a 'wheel only' LIF signal for squalane. The error bars are the standard 1σ error in the mean and are plotted on every other point for clarity.

5.4.3: Appearance profiles

A general description of appearance profiles was provided in section 2.9.1. The description given here will be more detailed and in some ways specific to this set of experiments. The term appearance profiles itself relates to the appearance of OH over time. This is collected while increasing the delay between photolysis and probe pulses. During these scans the probe laser is set at a fixed wavelength, usually of a selected transition.

The day-to-day collection of these appearance profiles followed a set procedure to ensure reproducibility. First a transition was selected (three were studied in this section of work $Q_1(1)$, $Q_1(5)$ and $Q_1(10)$) and the probe laser was set to the approximate wavelength; using the theoretical wavelength from LIFBASE [36] as a guide. Then probe laser was slowly scanned in both wavelength directions at a photolysis probe time delay of zero μs. This was to determine the exact wavelength of optimum OH detection on the relevant probe transition. This signal size at this wavelength was recorded and monitored regularly to check stability. The sets of appearance profiles were then collected at this desired wavelength. Each of the three

liquids and the no-wheel were scanned in a single day with a randomised order. For each liquid or no-wheel set ~10 scans were performed and then averaged.

After collecting each set of 10 scans, four further scans were taken. Two scans– known as photolysis only were collected using the same experimental conditions except the probe laser was blocked. A further two scans were collected – known as probe only using the same experimental conditions but with the photolysis laser blocked. The average of the two scans of both probe only and photolysis only were subtracted from each set of collected data to remove any scattered signal contribution emanating from the lasers. Including these extra scans, each set of data took just over an hour to collect. Once this subtraction of background photolysis and probe signals had been completed the no-wheel signal could also be subtracted using the same no-wheel set of ten scans to subtract from each of the three liquids (squalane, squalene and PFPE) recorded in that day. After this, signals were normalised at 3 μs, this is sufficiently early enough to ensure that no post-collision OH is present but accounts for daily fluctuations in the quantity of pre-collision OH. All data presented in graphical form (Figures 5.6, 5.7 and 5.17) were collected on at least three separate occasions and are therefore an average of at least thirty separate appearance profiles.

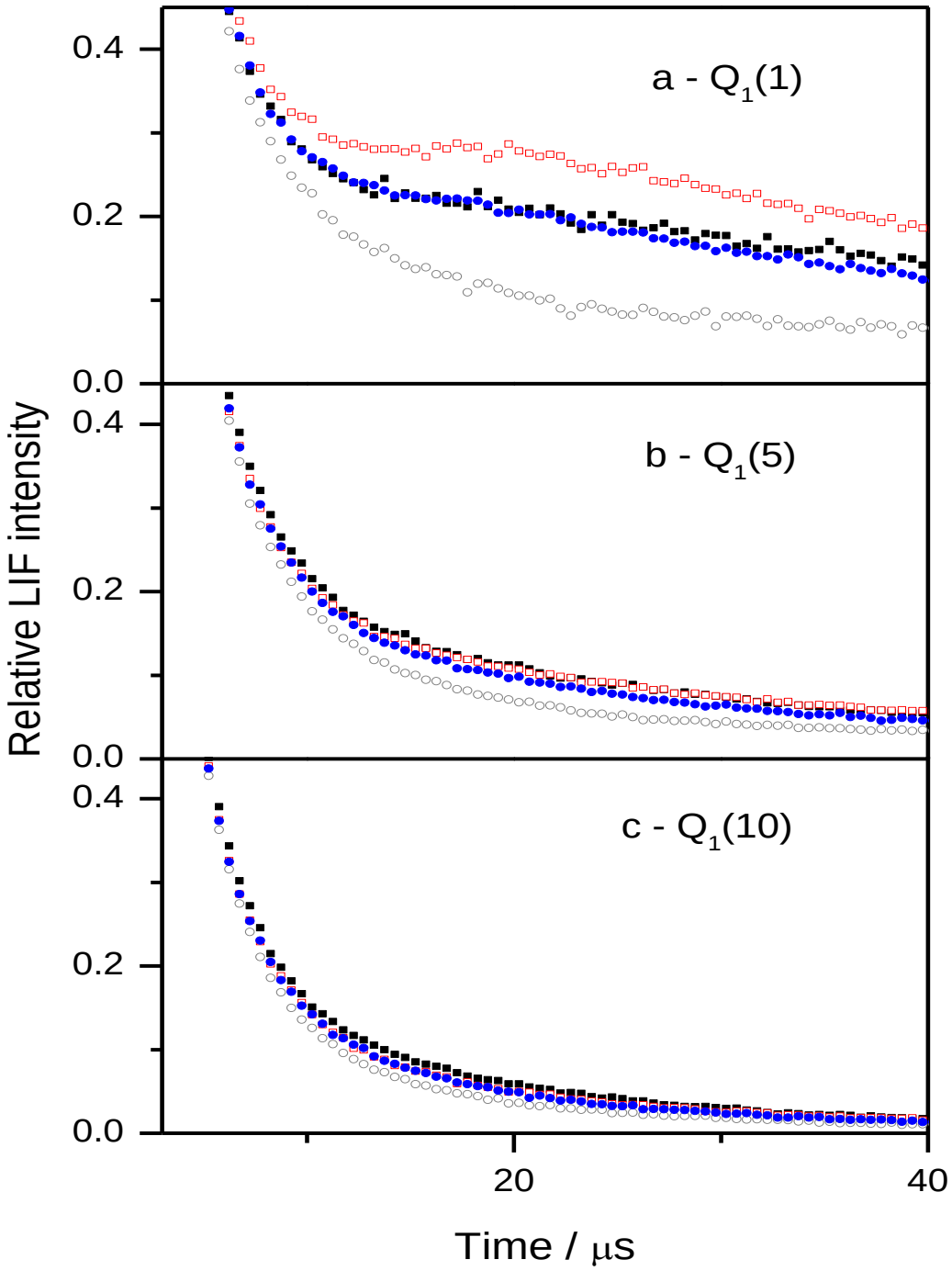

Figure 5.6: Appearance profiles recorded on the OH A-X (1,0) band are shown for PFPE (black, closed squares); squalane (red, open squares); squalene (blue, closed circles) and no wheel (grey open circles) for each of the probe transitions a - $Q_1(1)$, b - $Q_1(5)$ and c - $Q_1(10)$. Error bars have not been displayed for clarity but are included in the subtraction shown in figure 5.7. P(allyl alcohol) ~ 1 mTorr, wheel-laser axis distance = 9 mm.

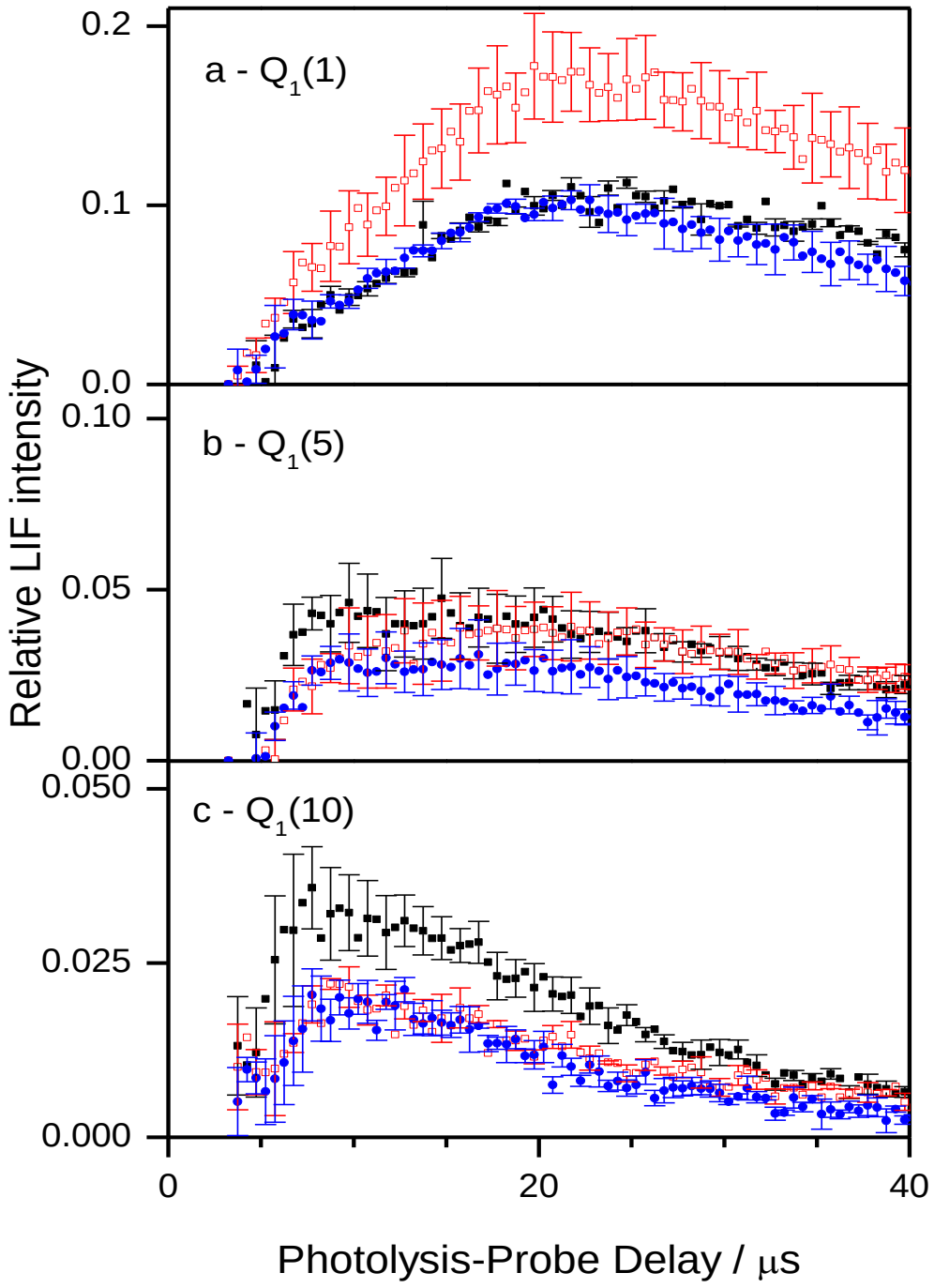

Figure 5.7: Subtracted profiles for each of the liquids recorded on the OH A-X (1,0) band are shown: PFPE (black, closed squares); squalane (red, open squares) and squalene (blue closed circles) for each of the probe transitions a - $Q_1(1)$, b - $Q_1(5)$ and c - $Q_1(10)$. Error bars are the 1σ standard error in the mean of the measured data points. Only every second error bar is plotted for clarity. P(allyl alcohol) ~ 1 mTorr, wheel-laser axis distance = 9 mm.

There are many things to note about the appearance profiles collected. Looking at figure 5.7, it can be seen that early on there only appears to be a small amount of post-collision OH for N = 5 and 10 (Q_1 (5) and (10)). This is most likely just an optical effect of the population being spread over a greater number of rotational levels.

The other important point to note, which makes the overall signal appear even smaller, is that there is a wide variety of speed distributions, even within the pre-collision OH, this broad speed distribution was proposed by Dhanya et al. to explain large errors in their measure of the translational distribution [33]. Indeed this seems to be confirmed by our own experiments where pre-collision OH signals persist at long times despite the fast average translational speed.

This is most evident in the N = 1 (Q_1(1)) appearance profile, where the signal is still very large even at 45 μs where the graph ends. This means that the absolute signal is spread over a wider interval, making the signal in each level appear smaller when compared to HONO (Figure 5.17) where the scattered OH is spread over around half the rotational levels. This also means that the post-collision distribution is much more difficult to extract. Where a speed distribution is near-monotonic, as with HONO [discussed in section 5.5.3 figure number 5.17], a sharp peak is distinguishable at early times and drops sharply. When the post-collision OH begins to appear in time, most of the pre-collision OH is gone, meaning that only a small correction is made. In this case, as the speed distribution is wide-ranging the whole no-wheel profile must be abstracted. However, this can be done, and as seen from Figure 5.7, it is possible to extract only the post-collision OH.

Most of the useful information is contained in figure 5.7. In the subtracted profiles the two main things to compare are the three individual N levels for each liquid. The liquids can also be compared to one another on any specific N level.

First of all, it can be seen that the appearance profiles for each N level are very different. Notably, the peak for each level differs in size, where N = 1 is over four times larger than the peak for N = 10 for all liquids even after transformation to a flux (which accounts for the fact that slower molecules spend more time in the probe volume and therefore contribute more than faster moving molecules) this difference is still significant.

Secondly, the shapes of the appearance profiles are very different for each individual J level. For *N* = 10, the peak of the appearance profiles is very early and occurs between 7 and 9 μs for all liquids. For *N* = 1, the peak is fairly late and occurs at 20-25 μs for all liquids. Also in *N* = 1, the signal is still very high when the plot ends at 45 μs. It can be observed that signals do not decay to zero at times longer than 30 μs and are *N* dependent and correlate with peak signal intensity. We believe that this anomaly in the *N* = 1 is due to thermalised gas-phase OH which is initially formed through secondary gas-phase collisions of OH produced by photolysis. This specifically means that OH which has undergone two distinct collision encounters is detected more than once by the probe laser. Under these conditions, the same OH molecules can be detected numerous times meaning the signal appears to decay very little. This only occurs at times longer than 30 μs, which is why data beyond this time is not used in analysis. The appearance profile for *N* = 5 ($Q_1(5)$) is intermediate between *N* = 1 and *N* =10. The reasons for these differences will be explained further in section 5.5.3.

Looking more specifically at each liquid, it can be seen that there are more subtle liquid differences in each individual *N* level. It can be seen that PFPE peaks slightly earlier than both squalane and squalene over all levels. It is most easily observed in the higher *N* levels. In addition to this small changes are evident between the peak arrival times of squalane and squalene. Also evident and most observable in *N* = 1 is that the quantity of OH returning from squalane and squalene is very different. These differences show that the nature of the liquid surface is very important in determining the shape and size of the appearance profiles. These observations will be explained in more depth in section 5.5.3.

5.4.4: Rotationally resolved LIF excitation spectra

The second type of experimental data collected in this study was the rotationally resolved LIF excitation spectra. These were collected by varying the wavelength of the probe laser while keeping the time delay between the photolysis and probe laser pulses constant. This resulted in a complete rotational excitation spectrum collected across a designated wavelength range. Excitation spectra can usually be used to quantify the spin-orbit and Λ-doublet distributions but in this case there are so many high *N* lines populated that it would be very difficult to analyse. However, these

calculations were performed for HONO where there was a modest spin-orbit and minor lambda doublet preference. These preferences were found to scramble on impact. It is reasonable to assume, that as OH from allyl alcohol and OH from HONO have similar translational distributions, if any preferences existed in the OH distribution from allyl alcohol they would be lost on collision also.

The LIF excitation spectra were collected following the appearance profiles. Using the data collected in the appearance profiles, it was decided to collect excitation spectra at 3, 7, 16 and 21 μs. These times correspond to the peaks of the appearance profiles at the three *N* levels, 1, 5 and 10, while 3 μs is chosen to characterise the pre-collision OH. To collect the excitation spectra a wavelength range was selected, using LIFBASE [36] to identify the desired transitions. After the range had been selected, the power of the probe laser was set to be constant, by choosing a probe power and setting the motor position of the doubling crystal at each point to ensure this probe power remained constant by measuring with a power meter. This method of setting a constant power across a wavelength range ensures correct ratios of one branch to another over the entire wavelength range. This method is preferable to setting a maximum power across the entire range where those transitions in the middle of the dye range, where the power is naturally higher, would falsely appear more intense. This learned power setting was used to scan the wavelength range for each of the three liquids and the corresponding no-wheel trace. The no-wheel trace is required to be collected in conjunction with the other liquids as the broad ingoing speed distribution of the OH means that some pre-collision fragments may still be present at the specified times. This was most likely to occur in the 7 μs LIF excitation spectrum but is still present, even at 21 μs. In our current experimental set-up we cannot record a spectrum with a liquid present and a no-wheel spectrum without evacuating the chamber and imposing a (slightly) different set of conditions. Therefore to allow us to properly scale and subtract the no-surface signals from those from the liquid coated wheel, we have used the appearance profiles to infer the correct ratio of no-wheel to each spectrum with liquid present and scaled the excitation spectra using this ratio. The spectra were then converted into populations (this process is described in section 5.4.4) and subtracted the scaled no surface populations to produce final population distributions shown in section 5.4.4.

When comparing the various liquids at the same time (figure 5.8), the first thing to note is that the signal size for the no-wheel is slightly smaller than for all the spectra with liquids present. This is seen as the signal to noise ratio is slightly higher. This is to be expected as most of the pre-collision OH will have left the probe volume by this time, in fact, it may be surprising that the pre-collision OH signal is so large at that time.

One of the most important points to note is that for all liquids the temperature appears to have cooled from the pre-collision OH (shown in panel (a) of figure 5.9). It appears from the spectrum that only a modest amount of cooling has taken place in PFPE while a greater amount of cooling has taken place in the cases of squalane and squalene. This can be most clearly observed in the Q_1 branch where the ratio of $Q_1(1)$:$Q_1(10)$ decreases in the order No-wheel: PFPE: squalene: squalane. This trend can also be observed in the R_1 branch where the $R_1(1)$: $R_1(6)$ ratio decreases in the same order as before. This shows that the different liquid surfaces have an effect on the rotational excitation of the post-collision OH. This will be explored further in section 5.5.2.

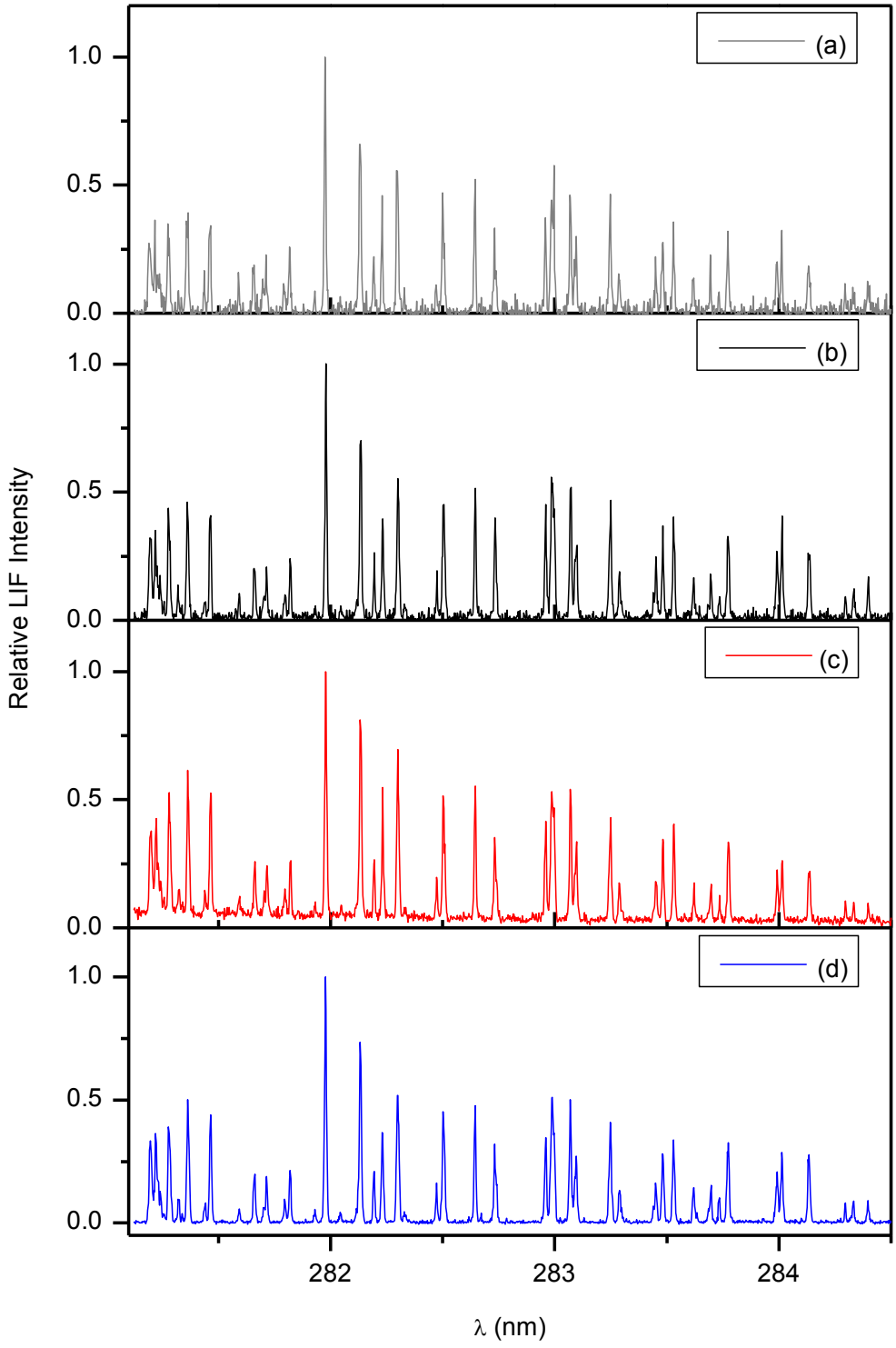

Figure 5.8: Representative excitation spectra on the OH A-X(1,0) band of different liquids at 21 μs. Spectra: (a) - no-wheel; (b) - PFPE, (c) - squalane and (d) - squalene. P(allyl alcohol) ~ 1 mTorr, wheel-laser axis distance = 9 mm. All spectra are normalised to 1 at the highest line, in all cases, the $Q_1(1)$ line. The laser linewidth was 1 cm^{-1} and the laser step size was 0.1 nm.

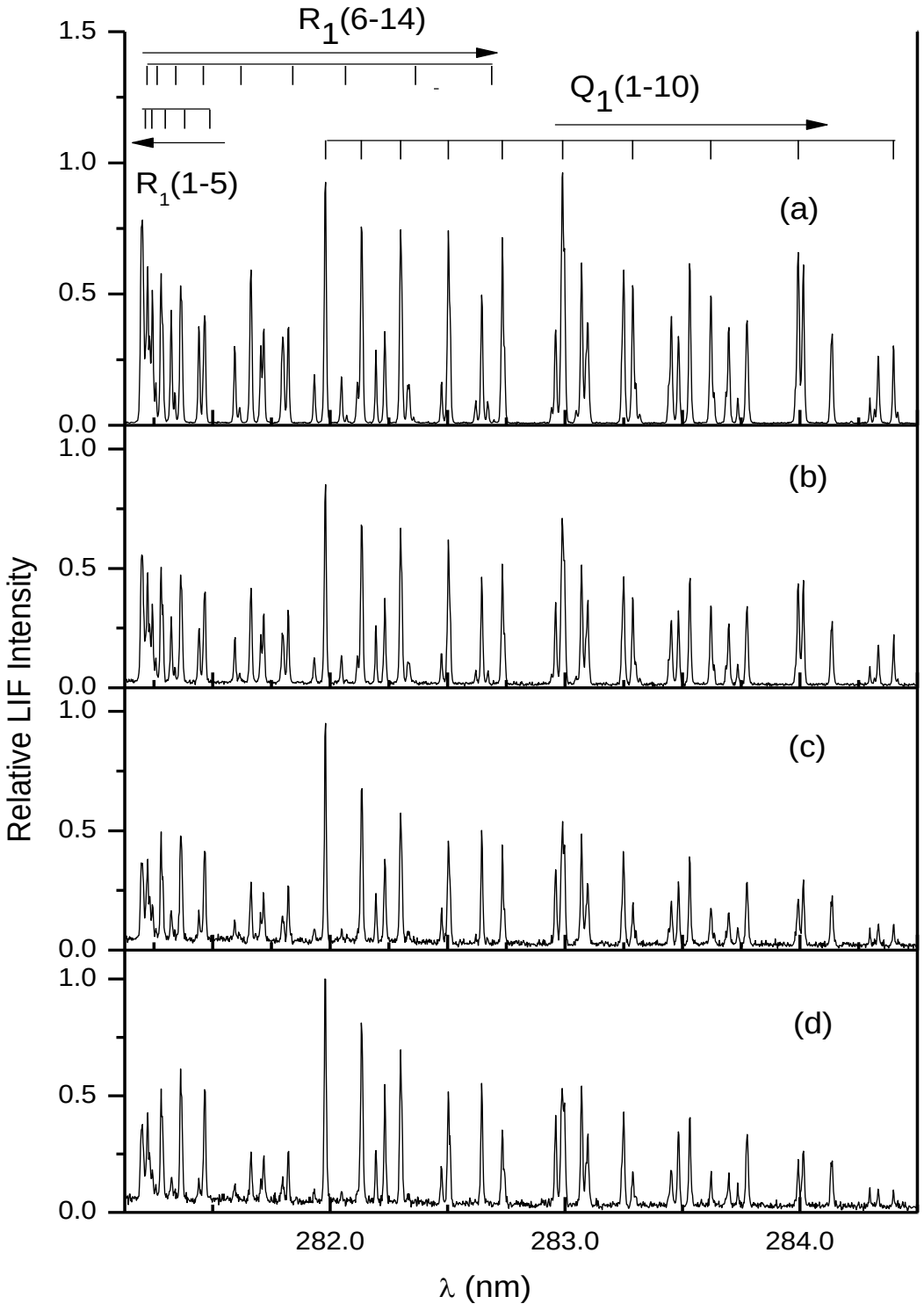

Figure 5.9: Representative excitation spectra on the OH A-X(1,0) band of squalane at different times. Spectrum a is taken at 3 μs; b at 7 μs, c at 16 μs and d at 21 μs. P(allyl alcohol) ~ 1 mTorr, wheel-laser axis distance = 9 mm. The R_1 branch is labelled on the left in two parts and the Q_1 branch is labelled on the right. The laser linewidth was 1 cm^{-1} and the laser step size was 0.1 nm.

When comparing the spectra for squalane by time (as in figure 5.9), the spectra are organised by delay, which enables clear differences to be observed as time progresses. Spectrum a is taken at 3 μs, spectrum b is taken at 7μs, spectrum c is at 16 μs and spectrum d is at 21 μs. In spectrum (a) it can clearly be seen that the low and high *N* lines are a similar size indicating a high temperature. As time progresses, the ratio between the size of the low *N* and high *N* lines increases indicating a cooling in temperature as time progresses. However, it is important to note that the high *N* lines are still present even at long times, indicating that even when a lower temperature is present that there is still a higher temperature component present. This is indicative of the fact that these distributions may not conform to a single temperature.

5.4.5: Optical saturation effects

An important variable to check is that the probe power is low enough in all excitation spectra to ensure that saturation does not significantly affect the derived populations. The phenomenon of optical saturation can be observed most easily when beginning with a low probe laser power. To observe fluorescence the probe laser is exciting the OH to a higher vibrational level. On returning to the lower level a photon is emitted and this fluorescence is detected. On increasing the probe laser power, the signal size of a transition will begin to rise linearly. At a certain point, when the population in the lower level begins to become depleted this signal will no longer rise linearly as there begins to become a case where every molecule that returns to the ground vibrational state via stimulated emission is immediately excited. At this point extra power does not help increase the signal size but begins to cause broadening of the peaks. Saturation affects the lower *N* transitions more than higher *N* ones as the Einstein coefficients for lower *N* lines are higher. To determine whether or not our LIF excitation spectra are susceptible to saturation effects, the ratio of low and high *N* lines which are close together must be investigated with varying probe power. To investigate if this effect was present in the data collected an experiment was set-up where the Q-switch delay between the flash-lamp pulses is varied to change the energy of the probe-laser pulse. A shorter Q-switch delay means that charge has a shorter time to accumulate and as a result of this probe laser energy is reduced. The data collected for this experiment are presented in figure 5.10. Spectrum (a), taken at

a probe delay of 160 μs, represents the typical experimental conditions used in collection of LIF excitation spectra presented in figures 5.8 and 5.9

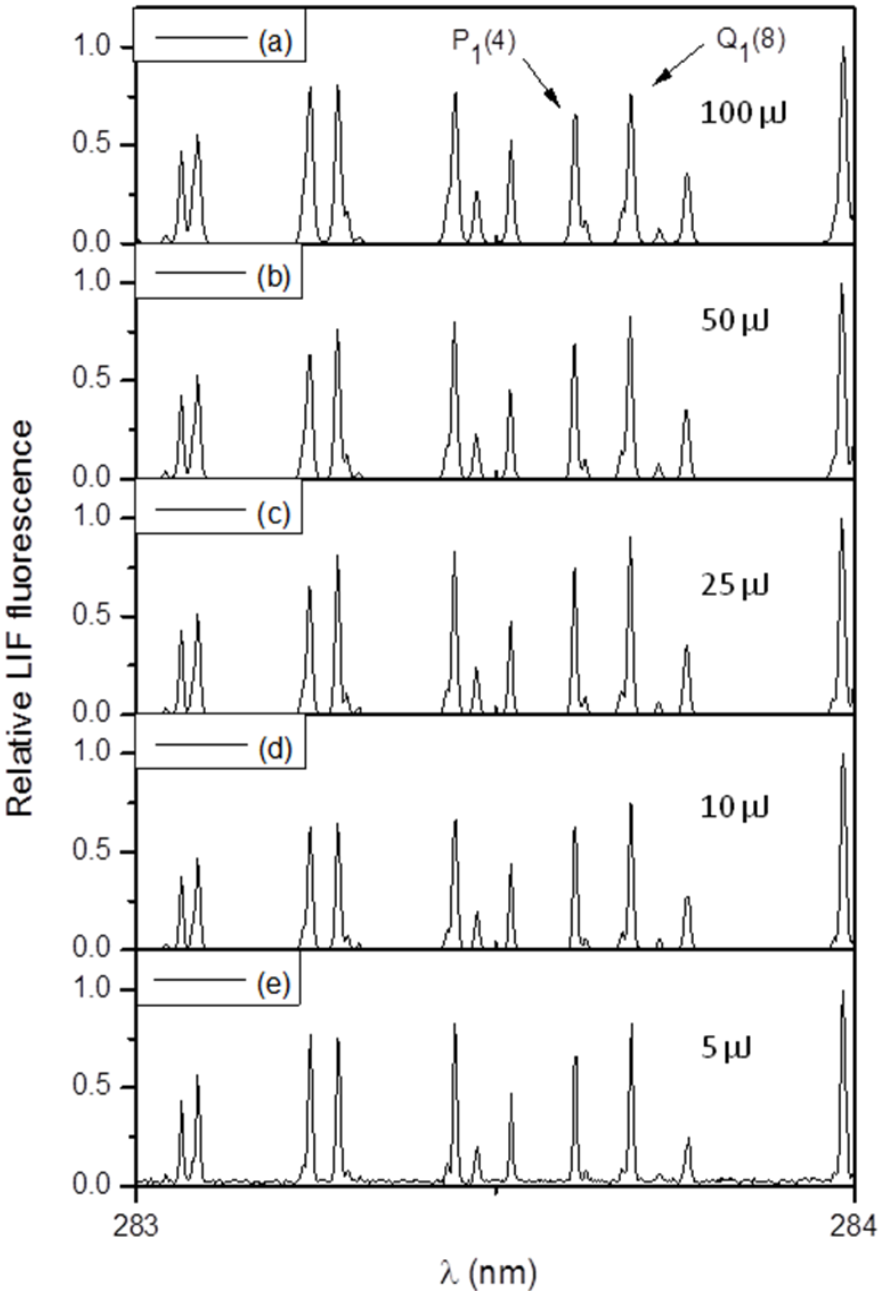

Figure 5.10: Representative excitation spectra on the OH A-X(1,0) band of nascent OH at a photolysis-probe delay of 0 μs, with a varying Q-switch delay. The probe power across this range varied from 5 – 100 μJ. The two compared transitions are labelled. Spectrum a is taken at 160 μs; b at 120 μs, c at 110 μs, d at 105 μs and e at 100 μs. The relation of these delays to probe power is presented in table 5.2. P(allyl alcohol) ~ 1 mTorr. Wheel-laser axis distance = 9 mm. Spectra are normalised to 1 at the most intense line.

The Q-switch delay was varied from 160 – 100 μs, in the manner shown in table 5.3. This is shown in figure 5.10 ((a) – (e).

Q-Switch delay (μs)	Laser pulse energy (μJ)	Laser fluence (J/m^2)	% of initial power
160 (a)	100	0.033	100
120 (b)	50	0.017	50
110 (c)	25	0.008	25
105 (d)	10	0.003	10
100 (e)	5	0.002	5

Table 5.3: Variation of probe laser power with Q-switch delay. The final column shows the % of power remaining from the initial power used in collection of all LIF excitation spectra.

Using figure 5.10 for comparison, a low *N* line and a high *N* line are compared. These lines were chosen to be $P_1(4)$ and $Q_1(8)$. The lines were chosen as they are not blended with any other transitions and are close to one another in wavelength allowing both an easier comparison and ensuring minimal variation in experimental conditions. The transitions are labelled in spectrum (a). An increase of probe power from low (e) to that used in experiments (a) shows only a minor change in the ratio of these two peaks. This can be taken to mean that optical saturation will only have a minor effect on these spectra and the effects will be negligible. The effect of saturation between branches is difficult to compare. There is no reason to believe that saturation will affect any one branch more than another, however to ensure that this would not be a factor, each branch was analysed separately (as described in section 5.4.4) to derive populations, conserving the ratio of lines within a branch to one another. Absolute signal heights of Q:R branches were not be compared. When performing a global analysis of all branches (section 5.5.2) combined absolute signal heights need not be included, it is only the in-branch line ratios which will be compared. The branches will be scaled to one another for comparison but this by no means reflects their true sizes or scale relative to each other.

5.4.6: Extraction of populations from excitation spectra

The process of extracting populations from the excitation spectra is a relatively simple one with few steps. However, in this case of allyl alcohol, the matter was complicated by the fact that pre-collision allyl alcohol was present even at 21 μs. This long-lived pre-collision signal coupled with the fact that with our current experimental set-up that the no-wheel and liquid experiments cannot be completed without opening the chamber to remove or replace the wheel, thus imposing a (slightly) different set of conditions.

To extract the populations from an excitation spectrum the simulation programme LIFBASE is used [36]. The collected excitation spectrum is imported into the simulation programme and the wavelength settings are adjusted for any absolute offset, as necessary, so that the transitions line-up. For each branch in turn, the heights of the simulated spectrum are matched to the heights of the experimental data collected. The programme then transforms the heights into relative populations. These relative populations can be turned in to absolute populations if required by measuring the intensity of the LIF signal at one particular transition and multiplying the relative populations by this number. For the $Q_1(1)$ transition, it is known (from LIFBASE[36]) that there is around 15 % of the $R_2(3)$ transitions present at the pre-collision temperature of 2050 K. This is removed from all $Q_1(1)$ measurements taken in excitation spectra before processing to populations occur. This 15 % is not removed from appearance profiles, as they all contain it we can compare $Q_1(1)$ transitions to other $Q_1(1)$ transitions without correction but not to any others, even within the same branch.

To ensure that the correct ratios of signals from the LIF excitation spectra of each liquid to the no-wheel standard were conserved, data taken from the appearance profiles were used. As an example; if the data taken at 21 μs were being analysed, the LIF intensity of each liquid and the no-wheel would be recorded from the appearance profiles collected on the $N = 1$ ($Q_1(1)$) transition. The excitation spectra would then be scaled using the ratios recorded during the appearance profiles at the $N = 1$ ($Q_1(1)$) transition. This means that if the no-wheel intensity was normalised to 1 at the relevant delay at which the LIF spectra were taken, using the $Q_1(1)$ appearance profiles

the squalane would have a relative intensity of approx 2 and the PFPE and squalene both around 1.5. The N = 1 populations from the excitation spectra for each liquid would then be scaled to the same corrected ratio. The correct-scaled ratio of the populations in each level from the no-wheel spectra can then be subtracted from each set of populations derived from the excitation spectra for each liquid to generate a global population, those from the three main branches collected (Q_1, R_1 and R_2) were scaled and averaged. In figure 5.11, the scaled populations from each branch are shown together to indicate the level of agreement. The branches shown are for squalane collected at 21 µs. This coincides with the populations presented in figure 5.12.

We generally cannot analyse blended transitions and sometimes no transitions from certain *N* could be analysed. This is why *N* = 6 and 11 are missing from the figures below, and also why some error bars appear quite large. These are the result of averaging across two measurements where statistics may be poor. Generally where error bars are smaller, three measurements have been used. The Q_2 branch was excluded as there are only four unblended lines which can be seen in our spectra. Examples of the global average populations extracted in this manner are presented in the figures 5.12 and 5.13.

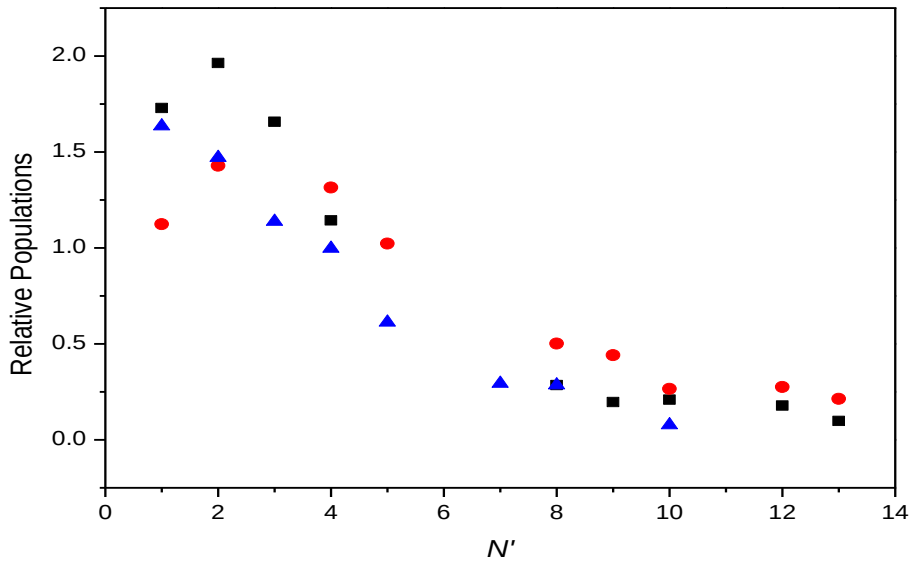

Figure 5.11: The 3 scaled branches at each *N*, to indicate level of agreement. R_1 is shown as closed black squares, R_2 is shown as closed red circles and Q_1 is shown as closed blue triangles.

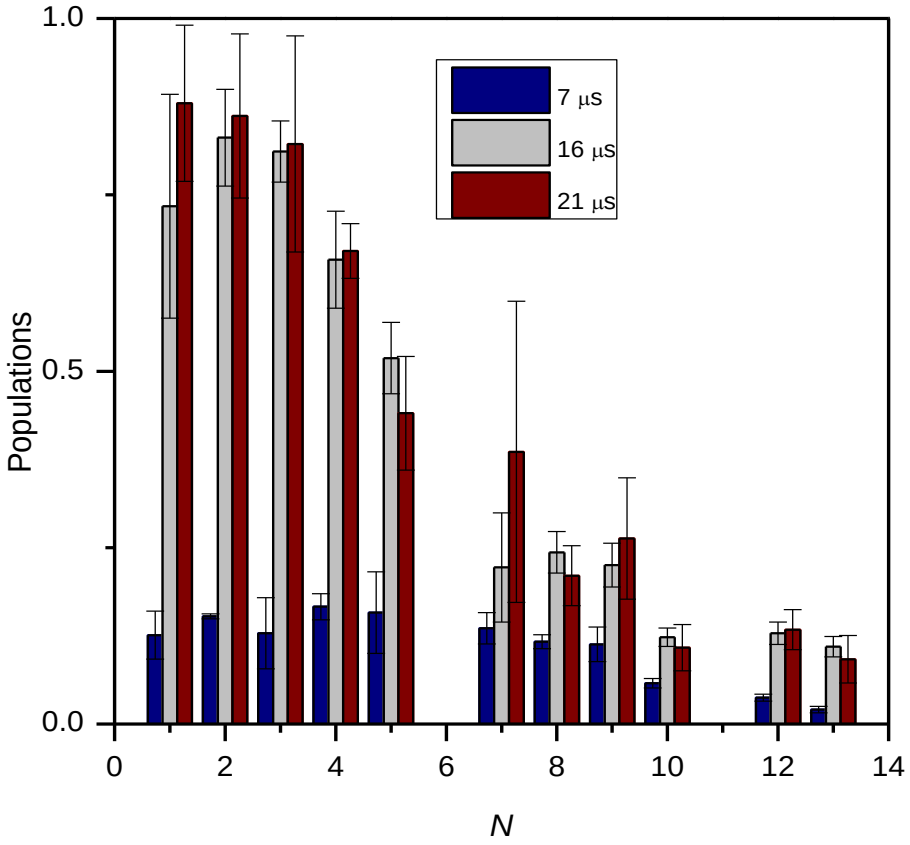

Figure 5.12: The global average (as described in the text) of squalane transformed into populations (excluding the Q_2 branch as there were only 4 data points available). The navy bars correspond to 7 μs, the grey bars correspond to 16 μs and the wine bars correspond to 21 μs shown at each *N*. The errors shown are the standard 1σ error in the mean.

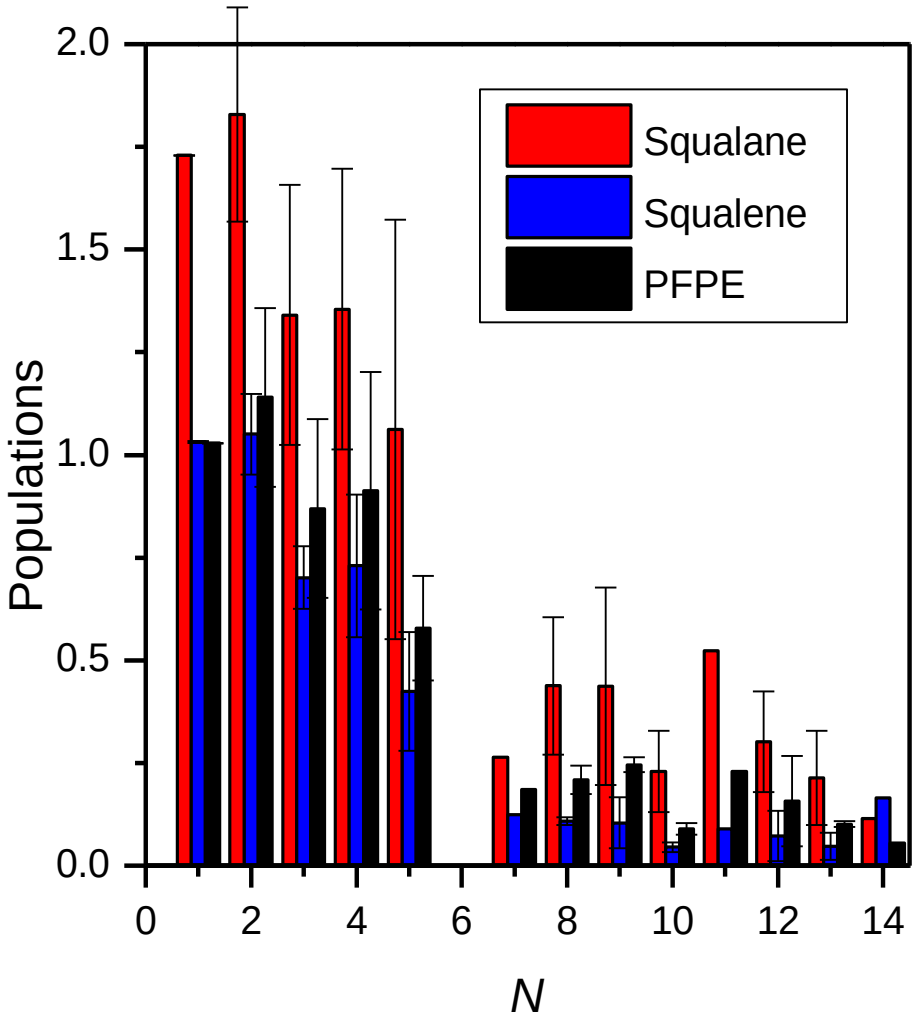

Figure 5.13: The global average (as described in the text) of each liquid transformed into populations (excluding the Q_2 branch as there were only 4 data points available) at 21 μs. The black bars correspond to PFPE, the red bars correspond to squalane and the blue bars correspond to squalene shown at each *N*. Error bars are the 1σ standard error in the mean. Where error bars are missing only one data point was available over the three branches. $Q_1(1)$ ratio was set using the method described in the text.

In figure 5.12, the OH population distribution from squalane generated from the LIF appearance profiles is shown to change with time. Possibly the most obvious difference is that the 7 μs signal is much smaller than the other two. This is because only the very fastest travelling OH molecules will have had time to travel to the surface, interact and then return to the probe volume for detection. This was evident in the calculation presented in section 5.4.2. From this figure, it can be seen that at 7

μs, the population at all levels is similar while at later times, the population in lower *N* levels begins to grow. The reasons for this will be further explored in section 5.5.2.

Looking at figure 5.13, where each liquid is compared at a delay of 21 μs, it can be seen that the error bars on all of the squalane measurements are large. This is because the liquid squalane seemed to be more sensitive to small changes in the conditions within the chamber than the other liquids. As was mentioned previously, the chamber must be brought up to atmosphere every time the liquid is changed, this means that despite the best efforts made that conditions within the chamber can never be entirely the same. Consequently, the data collected for squalane exhibited a larger spread than for the other liquids. Due to this fact the results for squalane in the excitation spectra often appear larger than it is believed they should. The results garnered from the appearance profiles are much more reliable as many different scans are performed and average per graph presented (30 on average), which minimises the effect of this spread. In the excitation spectra presented each is an average of three separate data scans and despite using a correction factor from the appearance profiles the data does not quite correspond. In this case, the excitation spectra for PFPE and squalene may be analysable and comparable and will be discussed but the main analysis on the liquid comparisons should be taken from the appearance profiles collected. There is no reason to believe that the ratios of the specific *N* lines will be affected by this as they should all appear larger by roughly the same amount. Therefore comparisons of various *N* lines within squalane are still valid.

Observing the data presented in figure 5.13, it can be seen that scattering is obviously a function of the liquid surface as the distributions for each liquid are different. The mechanistic reasons behinds this will be further explored in section 5.5.2.

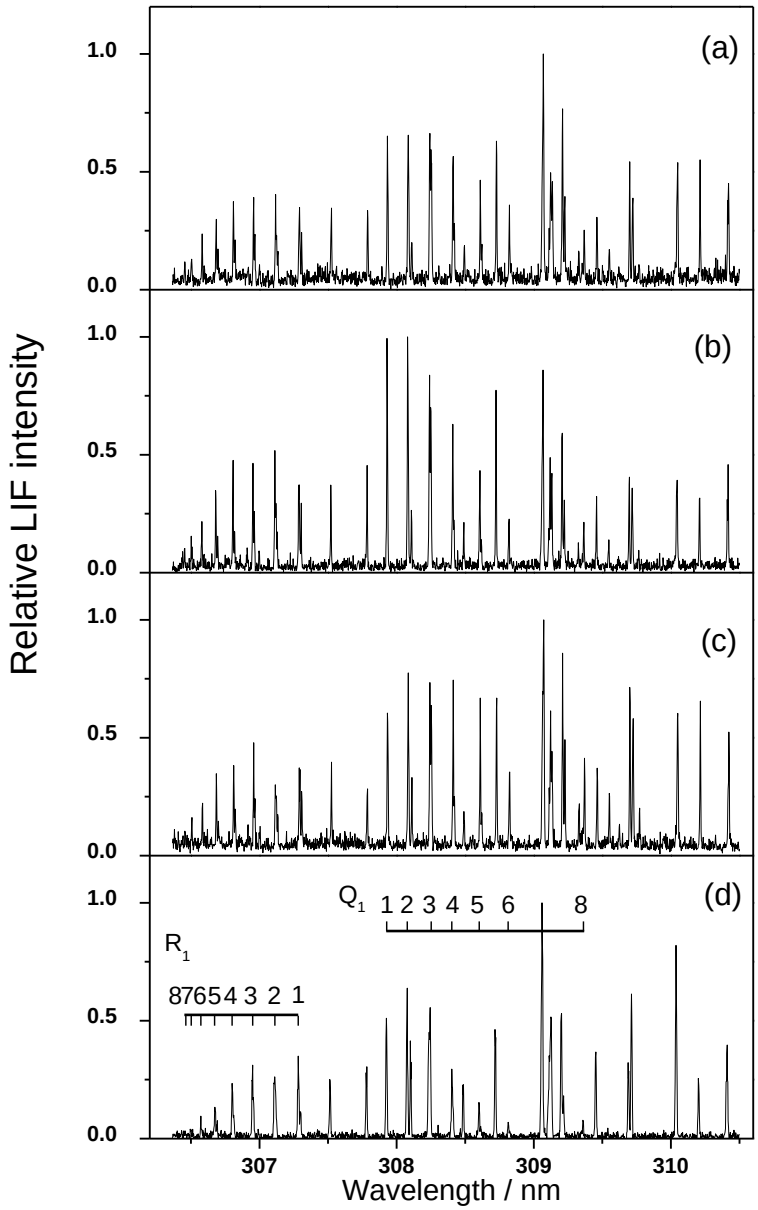

Figure 5.14: Representative LIF excitation spectra on the OH (from HONO photolysis) *A-X* (0,0) band at photolysis-probe delays of (a) squalene - 14 μs; (b) squalane - 16 μs; (c) PFPE - 12 μs and (d) pre-collision - 4 μs. All spectra have been normalized to the intensity of the strongest line. P(HONO) ~1 mTorr, wheel-laser axes distance = 9 mm. Taken from [2].

The first thing that is immediately noticeable about OH generated from HONO (Figure 5.14) is that there are far fewer *N* lines present in the spectra for all liquids. For HONO they only reach around *N* = 8 with significant intensity, while for allyl alcohol *N* = 14 could be clearly seen. This indicates a much lesser degree of rotational excitation overall. This is not too surprising initially as OH from HONO has different characteristics to OH generated from allyl alcohol. Pre-collision OH from HONO has a

translational energy of 53.7 kJ mol^{-1} [2] compared to around 85 kJ mol^{-1} for allyl alcohol [34]. These correspond to speeds of, 2500 m s^{-1} for HONO [2] and 3400 m s^{-1} for allyl alcohol [34]. Rotationally, OH from HONO is near-thermal [2] while from allyl alcohol is ~ 1900 K [34]. Taking this information into account, it is easy to see that the smaller number of *N* level present in the HONO spectra occur as a result of much smaller initial rotational energy. This means that after a comparable collision, far fewer OH molecules will have the required energy to rotate enough to populate higher *N* levels. These dynamics will be further explored in section 5.5.3.

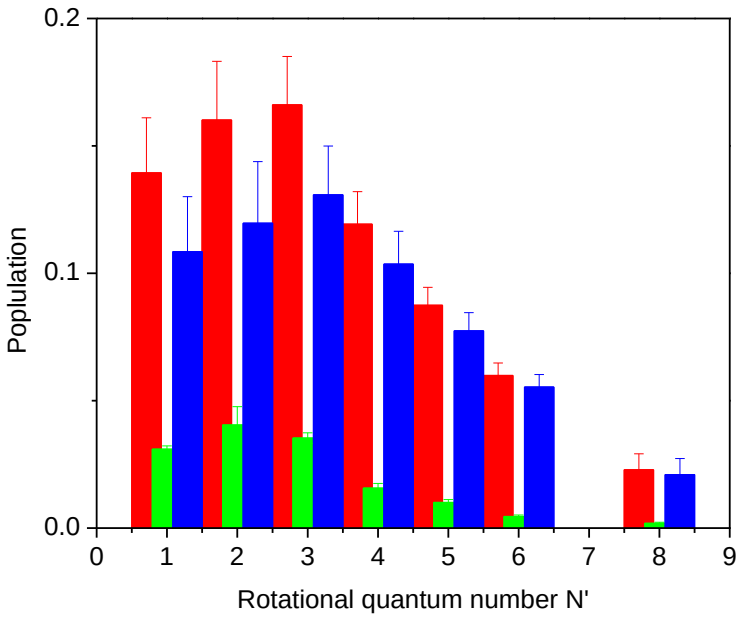

Figure 5.15: Global rotational populations extracted from OH LIF excitation spectra for squalane. (Red bars) populations extracted from the raw LIF spectrum at the peak of the appearance profile (16 μs). (Green bars) estimated weighted contribution from the underlying pre-collision distribution at the same delay. (Blue bars) scattered OH distribution, obtained by subtraction. Error bars represent the 1σ standard error in the mean of repeated measurements.

The populations shown in figure 5.15 reflect the data collected from the LIF excitation spectra. In contrast to the populations generated from OH from allyl alcohol scattering from squalane (figure 5.13) the distributions appear to decay more smoothly on increasing *N*. The differences between the two OH sources will be further explored in section 5.5.2.

5.5: Analysis of Results

To enable further interpretation of results, it is important to understand the types of interactions which may take place when an OH collides with the liquid surfaces under investigation. These mechanisms are summarised in the following section.

5.5.1: Mechanisms involved in OH collisions with liquid surfaces

At this point, it is apt to discuss the possible mechanisms which may take place when an OH molecule encounters the liquid surface and try to assign some of these mechanisms to the features which appear in the data. There are three main things that may happen to an OH molecule when it encounters a liquid surface. The first is that the molecule may simply bounce off the surface with a single encounter and leave with minimal time spent on the surface. This tends to result in a relatively minimal loss of energy meaning these molecules are often fast and hot. This is known as impulsive scattering (IS), these molecules will certainly be the earliest seen but may also appear later in time if longer paths to and from the surface are taken. The second limiting type of encounter which may occur is known as a trapping desorption or (TD) encounter. This is where a molecule reaches the surface and, instead of bouncing immediately off, the molecule bounces in or around the surface for a short period of time becoming more thermally accommodated. Generally the molecule loses much more energy in these types of collisions. This means that the molecules returning from these types of collisions are usually slower and colder than pre-collision OH assuming a hotter than thermal pre-collision distribution. The third type of encounter which may occur is reaction. In the case of OH there are two possibilities. Firstly the OH molecule may abstract a hydrogen from the liquid surface and form water (this is not possible in PFPE, where there are no hydrogens present). Secondly, the OH may add to the molecule. This can occur in species with double bonds such as squalene – these mechanisms are shown in figure 5.16. The quantity of OH to escape the liquid surface is known as the survival probability, σ, and is closely related to the reactive uptake, γ, (which was discussed in sections 5.2 and 5.3) as shown in equation 5.4

$$\gamma = 1 - \sigma$$ Equation 5.4

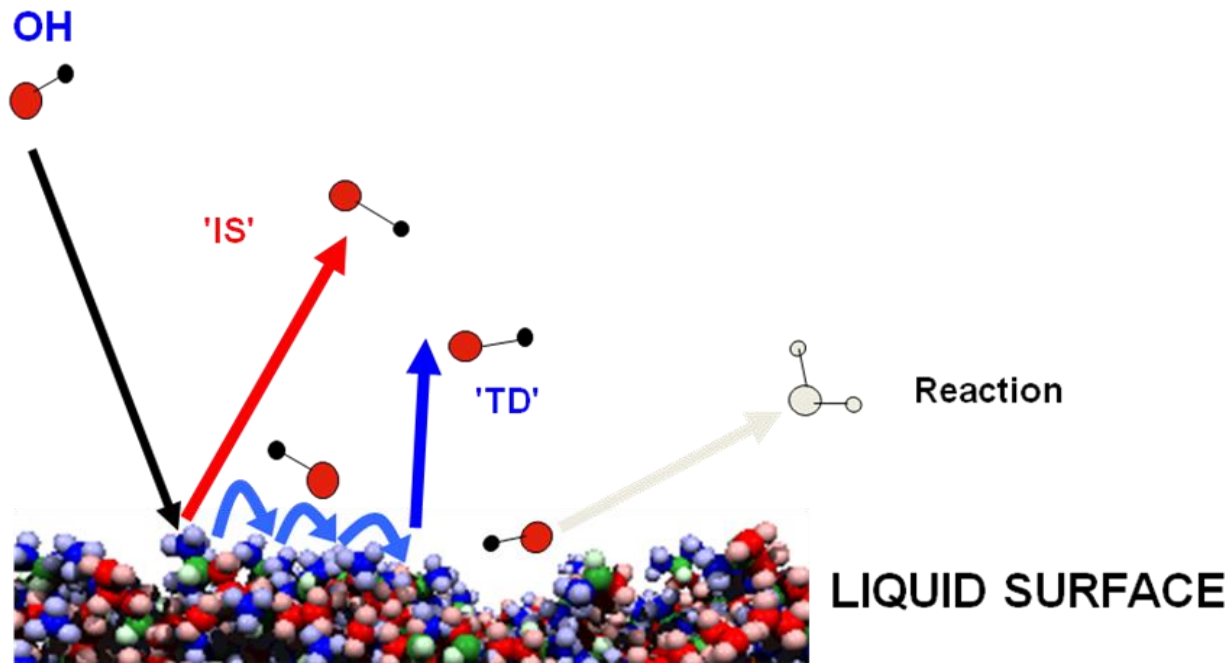

Figure 5.16: Schematic showing the various mechanisms of OH reaction. Pre-collision OH is shown with a black arrow. Impulsive scatter is denoted by a red arrow. Trapping desorption is indicated with a blue arrow and reaction is shown with a grey arrow. Figure generated by Kenneth G McKendrick and copied with permission.

5.5.2: Analysis of populations

Using the mechanisms described and looking back at the data presented in figure 5.12, it is reasonable to believe that there must be an impulsively scattered component present. If any molecules are present at 7 μs then this is the only reasonable mechanism which may have occurred. This mechanism has been observed previously [1, 2] and believe it is the cause of the early OH. The other obvious point to make is that the degree of rotational excitation of the returning OH is changing substantially over the three time points. At 7 μs, the returning OH is fairly hot and population extends across most levels. As time progresses, the populations in the higher *N* levels are growing slowly while the populations in the lower *N* levels are growing more quickly. This means that the overall degree of excitation is less as time progresses. The fact that the population in the higher *N* levels is growing slowly is no great surprise given that it is reasonable to assume that the most translationally excited OH atoms are also the most rotationally excited, and therefore that most of these appear at earlier times. What may be more surprising is that the population in the lower levels is

growing with time. This seems to indicate that a cooling mechanism of some sort is taking place.

This type of cooling mechanism has always been believed to occur but has been very difficult to observe when beginning with a source of OH which is near-thermal, such as HONO. By using a rotationally hot source of OH it was hoped that this kind of mechanism would be observable and the populations generated seem to provide the first clear evidence that this is so.

The populations extracted from the OH from HONO excitation spectra (figure 5.15) from squalane are shown alongside the comparative pre-collision spectra. From this it can be seen that the peak of the distribution moves from N = 2 in the pre-collision spectrum to N = 3 in the scattered spectrum. From this, it can be seen that in all cases the returning OH has increased in average rotational energy and therefore exhibits population of more N levels. This indicates that OH from HONO is extremely useful in determining a 'warming' (due to ballistic T-R conversion) or IS mechanism as opposed to allyl alcohol which is apt for detecting the cooling mechanism or TD mechanism.

Looking at figure 5.13, it can be seen that the squalane signal is much larger in the lower N levels than the other liquids. This seems to suggest that the squalane surface is the best at absorbing energy and therefore provides the most effective cooling. This is likely to occur as in IS scatter more energy will be lost to a softer surface during collision. In addition to this, a softer, rougher surface increases the likelihood of a trapping desorption mechanism. PFPE exhibits the least difference in population size between the lower and higher N levels. This seems to suggest that the PFPE is not as effective at cooling and provides more IS molecules. PFPE appears to be the worst at making cooler molecules. This is likely due to the fact that PFPE has the most rigid surface. The CF_3 groups are large and provide a very stiff surface. Molecules which collide with this surface are much more likely to impulsively scatter due to the heaviness and stiffness of the surface. These properties ensure that minimal energy is lost to collision. Squalene is intermediate between the cases of PFPE and squalane. This may be as the double bonds impose a level of rigidity in the liquid surface meaning that the flexibility is reduced and due to this, the ability of the liquid to act as

an energy sink. These properties have been confirmed by molecular dynamics simulations and make the squalene surface less soft than squalane [37].

Notably in all the allyl alcohol population data, none of the populations decay linearly and some even appear to have a secondary maximum. This indicates the presence of more than one temperature for all liquids at all times. We have seen previously, in the work on O^1D (Chapter 4), that a two-temperature Boltzmann model may be used to fit to distributions which have more than a single temperature distribution.

Once the data collected from the LIF excitation spectra has been collected and transformed into populations, further steps can be taken to transform the populations into Boltzmann plots from which the rotational temperatures can be extracted. To begin this process we take the global population data; the natural log of the population per *N* level divided by the degeneracy of that specific *N* level is taken. This value is plotted against the energy of each specific *N* level. This will provide a Boltzmann plot, from which the temperature can be extracted. If the plot is linear then only a single temperature is present and extraction of the temperature is simple as it is contained within the slope of the graph ($-k_BT$). In figure 5.17 the graph shape is curved; in this case it is reasonable to try and fit the temperature to a two-temperature model according to the formula presented in equation 5.5. One reason for trying to fit to a dual temperature is that the two types of scattering (IS and TD) may generate scattered OH with differing rotational excitation and although it is not possible to separate these two mechanisms, a dual temperature fit may be empirically useful.

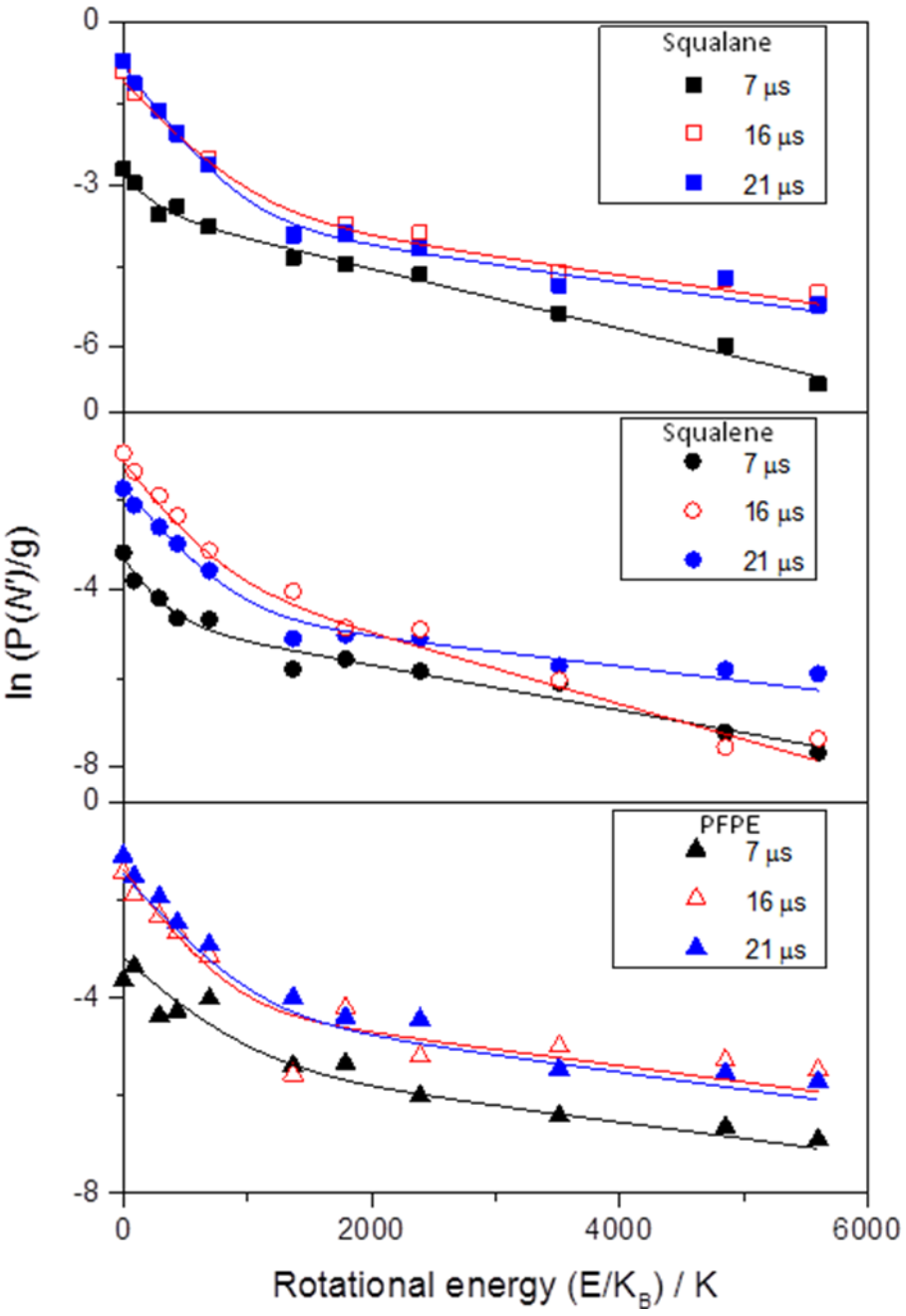

Figure 5.17: Boltzmann plots for the global scaled populations of the three liquids shown with their two temperature fits. Squalane is shown in the top panel with black closed squares for 7 µs, red open squares for 16 µs and blue closed squares for 21 µs. The fits for each time are shown as lines with the colour matching the appropriate time. Squalene is shown in the middle panel with black closed circles for 7 µs, red open circles for 16 µs and blue closed circles for 21 µs. The fits for each time are shown as lines with the colour matching the appropriate time. PFPE is shown in the bottom panel with black closed triangles for 7 µs, red open triangles for 16 µs and blue closed triangles for 21 µs. The fits for each time are shown as lines with the colour matching the appropriate time.

$$\frac{P(N')}{g_j'} = c\left(\frac{\propto \exp\left(-\frac{E(N')}{k_B T_1}\right)}{T_1} + \frac{(1-\alpha)\exp\left(-\frac{E(N')}{k_B T_2}\right)}{T_2}\right)$$

- Equation 5.5

where P(*N*) are the populations specific to each *N* level, g_j is the degeneracy at each specific level. *C* is a floating constant. α is the proportion of molecules with the colder temperature, T_1. *E (N)* is the energy of each specific *N* level and k_B is the Boltzmann constant.

Upon examining the data is figure 5.17, a few initial points can be noted. It is immediately obvious that there is definitely more than one temperature present at all times for all liquids. The two temperature fit also appears to capture the curvature of the data well and appears to be a suitable model for the data collected. For both PFPE and squalane, the 16 and 21 µs curves appear very similar to one another while the 7 µs curve is different in both cases. For squalene all curves differ in appearance. Comparing the results is much easier with the aid of the results produced in the two temperature fit which are summarised in table 5.4.

Squalane			
Time (μs)	α	T_1 (K)	T_2 (K)
7	0.091 ± 0.048	200 ± 98	1810 ± 112
16	0.513 ± 0.053	373 ± 66	3315 ± 732
21	0.576 ± 0.037	305 ± 41	3694 ± 805
Squalene			
Time (μs)	α	T_1 (K)	T_2 (K)
7	0.235 ± 0.083	200 ± 76	1963 ± 251
16	0.648 ± 0.102	267 ± 69	1255 ± 159
21	0.575 ± 0.035	303 ± 39	2989 ± 698
PFPE			
Time (μs)	α	T_1 (K)	T_2 (K)
7	0.465 ± 0.113	400 ± 159	3864 ± 1346
16	0.560 ± 0.129	282 ± 121	3803 ± 1560
21	0.612 ± 0.098	336 ± 101	2860 ± 1091

Table 5.4: The results extracted from the two temperature fit for each liquid. The errors correspond to the standard 1σ error in the measurements.

From the data presented in table 5.3, it can be seen that T_1 for all liquids corresponds to around 300 K (within error margins). It is believed that this largely corresponds to molecules which have undergone the trapping desorption mechanism and lost most of their energy when trapped at the liquid surface. Almost exclusively, the quantity of α increases with time further strengthening this evidence as it is likely that most of these molecules will take a longer time to return to the probe volume as they travel more slowly on their return journey. However, it is important to recognise that there must at least be some IS present in T_1 as at 7 μs when it is simply too early to observe TD style OH, there is still a 300 K component present. It is also possible that molecules present at later times are there because they have always moved more slowly, even pre-collision.

The case where this does not seem to apply is with squalene, where the quantity of molecules in T_1 drops between 16 and 21 μs. Although within errors these values are

the same so this may not be statistically meaningful. It was previously theorised [2] that slow travelling cold molecules may be performing an addition reaction across the double bonds in squalene. This could possibly be the cause for the loss of cold molecules seen here. Further evidence which may strengthen this theory is that temperature for squalene is higher at 21 μs than at 16. If the cold molecules were being lost to reaction then the overall temperature would appear higher at long times where more TD molecules will be expected to be present.

For PFPE, the upper temperature is cooling as time proceeds. This would be expected as the colder molecules produced would take longer to appear in the probe volume. For the other parameters, the statistics are too poor for any detailed comparisons to be drawn but are a useful indication of trends.

It is important to note that this method of analysis for the dual temperature component is useful for beginning to form a picture of the dynamics taking place within the OH-liquid interaction but due to the large number of parameters calculated from a relatively small measure of *N* levels there is a large propensity for errors. This means that these quantities should by no means be used as an absolute number for temperature or fraction of molecules present but just as a useful guide. The data presented here for the Boltzmann plots will now be compared to the aforementioned OH from HONO data [2] (Figure 5.18).

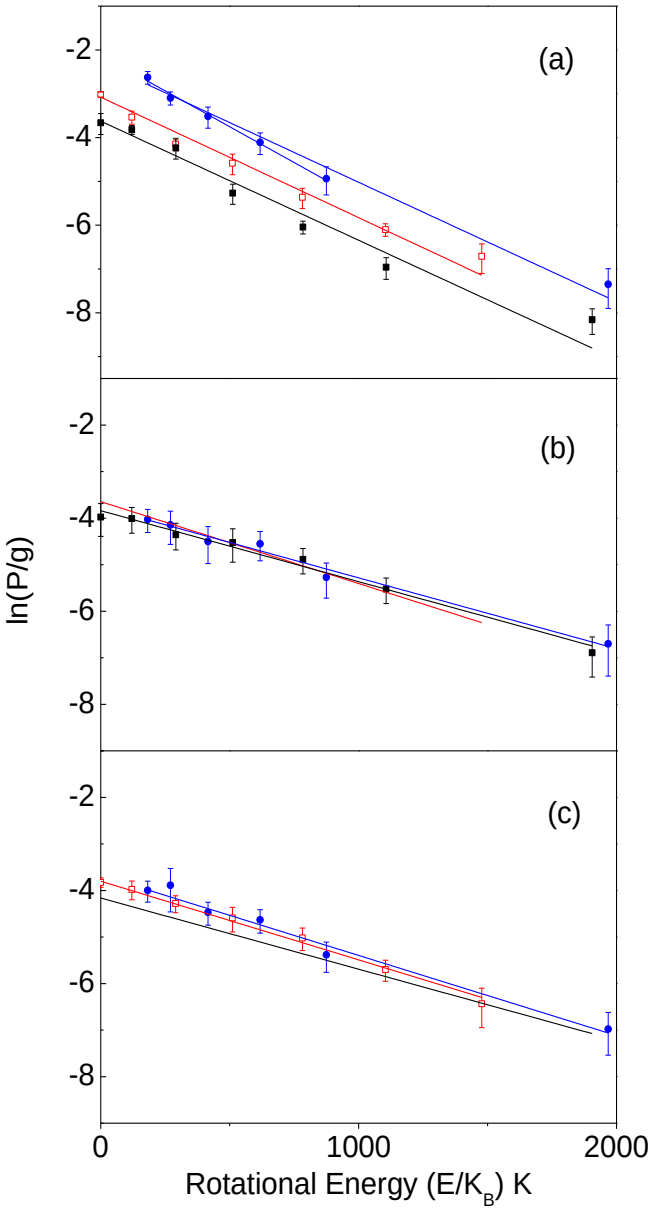

Figure 5.18: Representative Boltzmann plots for (a) pre-collision OH, and scattered distributions (with photolytic background contribution removed) from (b) PFPE and (c) squalene. Populations derived from R_1 (red open circles), Q_1 (black closed squares) and R_2 (blue closed circles) branches. Linear best-fits are shown spanning the full range in N or, in addition, $N = 1 - 5$ for R_2 in the pre-collision data in (a).

Comparing the Boltzmann plots of the data collected here from allyl alcohol to those from HONO (figure 5.18), it is easy to see an immediate difference. The OH generated from HONO gives linear Boltzmann plots characteristic of a single temperature. This was found to be an average of 365 K for pre-collision. The pre-collision HONO also had an F_2 spin-orbit preference and an A' Λ doublet preference both of which were

scrambled during collision. Even at *N* levels 1-8 (as shown for HONO) the allyl alcohol data would not fit to a straight line single temperature distribution.

The post-collision OH from HONO has warmed up from the initial near-thermal distribution in all cases. This is most likely due to the initial (relatively high) translational energy being transformed to rotational energy on collision with the liquid surface. For PFPE the rotational warming effect was most evident with the post-collision temperature equalling ~ 652 K. This was believed to be a result of the PFPE having a heavy, more rigid surface where less energy is lost in collision and therefore produces more impulsively scattered OH. Squalane showed the smallest temperature increase (to ~ 473 K) this may reflect the softness of the surface and its higher probability to perform the TD mechanism. In the HONO data squalene exhibited a higher temperature than squalane (~587 K) which may reflect the possibility that some of the colder OH is lost to reaction. This will be explored in more detail in section 5.5.3.

Comparison of the HONO to allyl alcohol data shows certain similarities. Both of these precursors are extremely useful for a specific function. HONO for observing the IS mechanism and translational to rotational energy transfer as molecules warm from near-thermal; it was difficult to definitively confirm the presence of a TD mechanism using HONO. Although IS is still the dominant scattering mechanism using an allyl alcohol precursor, the hotter than thermal pre-collision distribution is useful for observing the cooling effect of the TD mechanism.

5.5.3: Analysis of appearance profiles

The reaction mechanisms which were introduced with respect to the LIF excitation spectra are also applicable for appearance profiles. Due to the nature of the appearance profiles, the fact that a great number can be collected and averaged, the statistical error is greatly reduced.

Looking at the differences between the liquids (Figure 5.7), some interesting trends can be observed. PFPE is used as an internal standard in this study. It contains no hydrogen atoms which mean that OH cannot perform an abstraction reaction with the surface, leading to loss as water. As a result of this, it may be expected that PFPE would have the highest OH signal in each individual level. However, this is not the case as can be seen from figure 5.7. By definition, the PFPE signal from all levels combined

must be higher than the squalane signal for all levels combined. However, for any individual level the squalane signal may be higher than the PFPE signal. This appears to be what has happened for the case of N = 1, where the PFPE signal is a little higher than squalene but appears much lower in intensity than squalane. This trend is then reversed for N = 10, where PFPE is much more intense than squalane. For N = 5 all liquids have similar signals but PFPE is slightly higher than the other two. This trend seems to indicate that PFPE will have the higher signal overall as it is higher than both squalane and squalene by N = 5 and there are fourteen rotational levels overall. The N levels present go higher than N = 10, but this is the highest level that can be seen with the laser dye which was present in the probe laser. In the R branch lines were seen up to N = 14.

The differences in absolute signal sizes between the levels are probably partially due to the fact that the N = 1 level is lower in energy, and even where excitation may occur, a larger population would still be expected to reside in the lower energy level. Such a large low N level population may also be evidence of a cooling mechanism taking place, as the relative population in N = 1 appears to be much larger than in pre-collision OH [33, 34].

It is important to note that any population present in N = 10 indicates a rotationally hot molecule where the highest level accessible in a near-thermal sample would be around N = 7. It is probably a fairly logical trend that the peak of the N = 10 distribution is much earlier than for lower N levels. It is likely that molecules which have retained sufficient rotational energy from collision to be present in the higher N levels have this energy available for translation which means that it is fairly obvious that they will be travelling faster. Those present in the lower N levels have began in lower rotational levels to begin with and have retained their energy or have not retained as much rotational energy from collision and therefore will be travelling slower. The latter is known as translational-rotational correlation and implies that the fastest travelling molecules are also the most rotationally excited.

For all the liquids in collision with OH from allyl alcohol, the early time shapes (figure 5.7) are conclusive of the presence of the IS mechanism. This is most observable in the N = 10 graph where the peak arrival time of OH is present at 7 µs. This can be proved

by a simple calculation. The allyl alcohol pre-collision speed is 3400 m s^{-1}. This means that the journey to the surface of the liquid (9 mm in distance) takes 2.64 µs. Assuming that energy is lost to collision, the speed on the return journey will be lower. This means that the earliest reasonable time for molecules to be detected will be around 6 or 7 µs. Therefore we are detecting the fastest molecules only at this point as a result these must be due to the IS mechanism occurring.

Comparisons between liquids at the specific *N* levels are possible within this allyl alcohol data. The peak of the PFPE curves is generally earlier than the corresponding hydrocarbons. This is most evidently observed in the higher *N* levels. This phenomenon is likely a result of light OH molecule hitting an extremely heavy surface. The surface cannot absorb much of the collisional energy as it is so rigid, therefore a portion of this energy remaining is transformed into rotational energy meaning that the OH will have a higher quantity of OH molecules in upper *N* levels but will lose translational energy (speed). This explains why PFPE exhibits both a higher signal in upper *N* levels and has a faster overall speed. This effect has been observed in both previous studies by the McKendrick group [1, 2] and by Nathanson and co-workers in their molecular beam set-up [38-41]. With the current data it is difficult to tell if there are any major speed differences between squalane and squalene. If anything squalene is slightly faster which may stem from the effect of the double bonds imposing a slight rigidity on the surface. This effect appears to be minor at most here. To enable a better understanding of the TD mechanism, a TD only simulation can be superimposed on the appearance profiles. This TD simulation is generated using a custom built LABVIEW program and inputting the parameters from the real experiment such as beam diameter and distance to the surface. The program calculates the how many generated OH molecules interact with the surface and predicts the quantity to survive a TD collision along with their appearance time. This simulation has been included in figures 5.20 and 5.21.

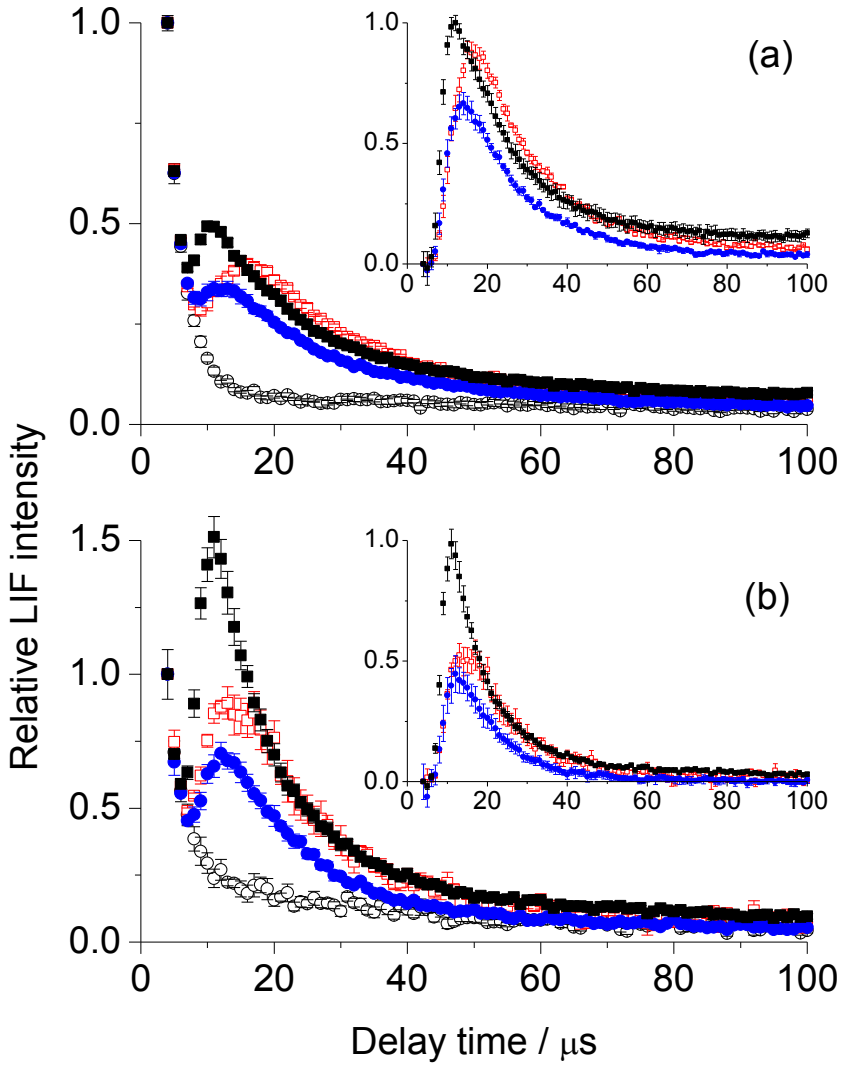

Figure 5.19: Main figure: appearance profiles of the OH *A-X* (0,0) LIF signal on photolysis-probe delay. (a) $Q_1(1)$, (b) $Q_1(5)$. Liquids: PFPE (black closed squares), squalane (red open squares), squalene (blue closed circles); plus background profiles with no liquid surface present (black open circles). All raw profiles have been normalized at a delay of 4 μs. Insets: profiles following subtraction of the background. In (a), N = 1 from PFPE has been renormalized at its peak. Those for other liquids remain in the correct proportions. Subtracted signals in (a) and (b) are also on a common scale, having been adjusted for the known relative populations of N = 1 for N = 5 in the pre-collision distribution at 4 μs. Error bars are the 1σ standard error in the mean of the measured data points. p(HONO) ~1 mTorr, wheel-laser axes distance = 9 mm.

From figure 5.19, the subtracted appearance profiles for OH from HONO can be analysed and compared to those captured for allyl alcohol in figure 5.7. In the case of OH from HONO the PFPE is largest in both N levels recorded. The main observable

difference in the HONO results is that the differences between squalane and squalene can be more clearly observed. In the case of allyl alcohol, most of the squalane to squalene differences are in absolute signal size. If these profiles are normalised to one another the shapes are fairly similar. For allyl alcohol, this is not the case. If the squalane and squalene profiles are normalised together there are distinct differences in the tails of the distributions. In this case the rising edges of the squalane and squalene are co-incident and the only differences stem from the region after the peak where the quantity of squalene returning is smaller than that from squalane. It was these results which first led to the theory that slow-moving TD type molecules were being preferentially lost in the case of squalene. The only differences between the two liquids are the presence of the double bonds in squalene, which led to the realisation that an addition mechanism of OH to the double bonds is the most likely culprit for this loss. This squalane and squalene difference is not so easily observable in the allyl alcohol data but the use of a TD simulation in conjunction with the allyl alcohol data as in figure 5.20 makes this more clear. The method for generating the Td simulations is discussed in appendix 1.

This TD simulation superimposed onto appearance profiles shows where a TD mechanism may begin contribute to observed OH. Previously in the HONO study (figure 5.21), it was found that the quantity of TD mechanism present was fairly small. In this case of allyl alcohol a much greater quantity of TD mechanism has been observed in the N=5 and N=1 levels as seen in figure 5.19. It can also be seen that the TD contribution to N=10 is almost negligible, this is because there is very little rotational thermalisation in this upper rotational level.

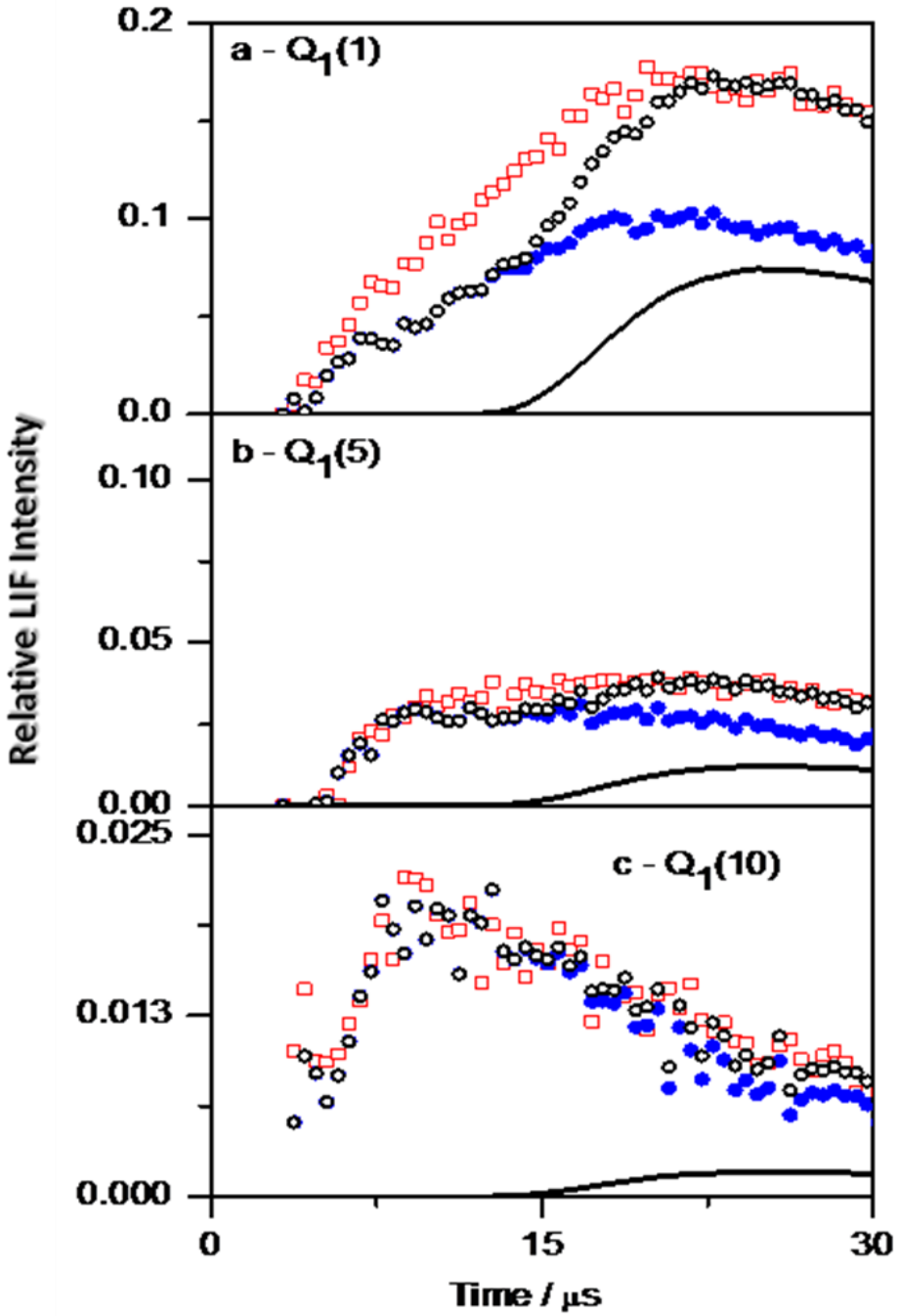

Figure 5.20: The squalane and squalene profiles from figure 5.7 are plotted to 30 µs. The TD mechanism only simulation is superimposed on the plots. Squalane is shown as open red squares, squalane as closed blue circles, the TD simulation is the solid black line and the sum of the TD simulation plus squalene is denoted by open black circles.

Using figures 5.20 (allyl alcohol) and 5.21 (HONO) as a reference, the same trend is repeated where the sum of squalene and the thermal simulation at 300 K look similar at later times where the TD mechanism would be present. This is extremely strong evidence that this TD cooling mechanism is indeed present as it has been observed in both near-thermal and hot pre-collision OH studies. This finding is reminiscent of the

results of Molina and co-workers where an observed increase in reactivity was observed for unsaturated versus saturated species [19, 20].

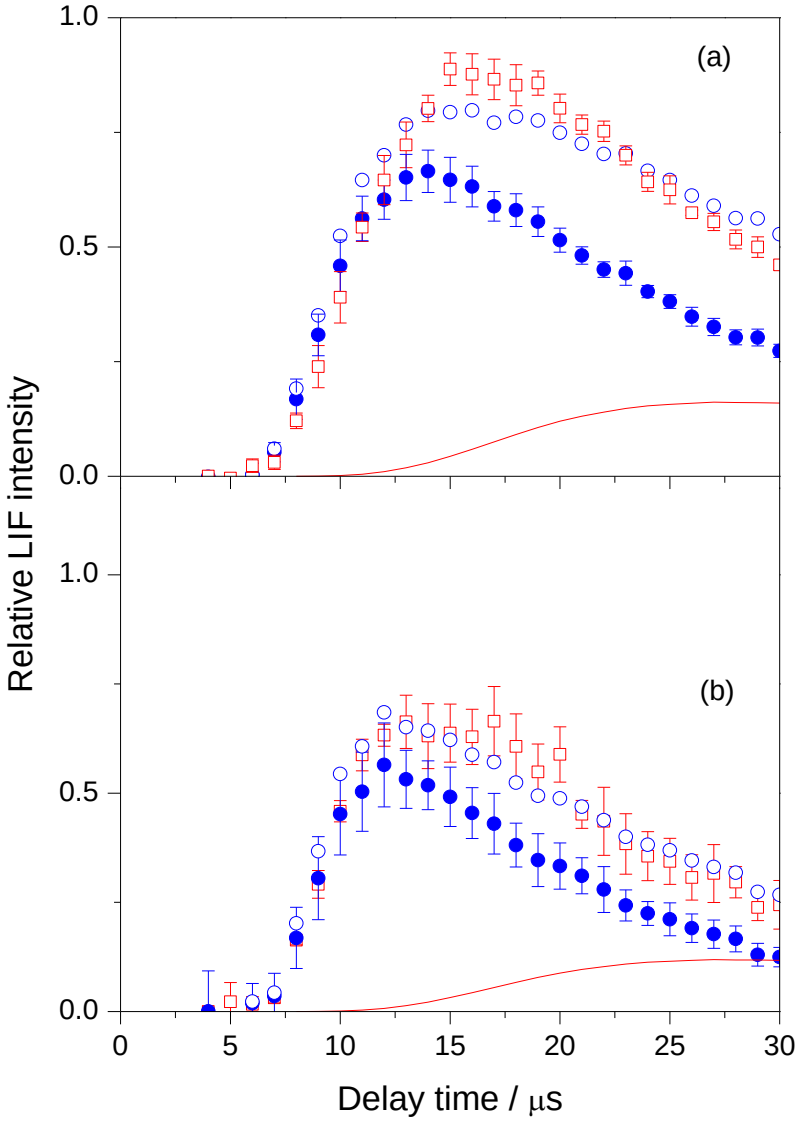

Figure 5.21: OH v' = 0 from HONO number-density appearance profiles. (a) $Q_1(1)$ and (b) $Q_1(5)$ transitions for squalane (red open squares) and squalene (blue closed circles). The normalisation correctly reflects the relative populations between liquids and between N' = 1 and 5. Composite profiles (blue open circles) are the sum of the squalene profile and an adjustable weighted contribution from a Monte-Carlo TD simulation (solid red line). Error bars are the 1σ standard error in the mean. p(HONO) ~1 mTorr, wheel-laser axes distance = 9 mm.

This finding could be extremely important in an atmospheric context and warrants further investigation. It has been theorised previously that uptake coefficient of OH with alkanes and alkenes does not vary much [4] in the atmosphere despite the fact

that addition of OH to an alkene double bond is possible. However, it has now been observed that with both near-thermal and higher temperature OH that a distinct difference in reactivity does occur. This means that this increased reactivity of OH with alkenes is likely universal over all OH energies and although the magnitude of this effect may vary with physical properties, it is likely always present. In fact, this may be more important in an atmospheric context where lower initial translational energies will favour TD style scattering. This means that there may be a potentially larger uptake for two reasons. First of all the addition to double bonds will be more likely as there will be more TD style OH. Secondly, there is less likely to be a direct abstraction mechanism from alkyl sites. This is an important finding relevant to atmospheric reactivity and would benefit from further research in experimental constructs different to the one described here.

In section 5.2 the subject of reactive uptake was discussed for OH generated from allyl alcohol, this quantity is hard to define as there are so many *N* levels to sum over and even a small population in v = 1. This quantity was calculated for the OH from HONO data. The results are summarised in table 5.5.

Liquid	PFPE	Squalane	Squalene
OH reactive uptake, γ	0*	0.30±0.08	0.39±0.07

Table 5.5: The reactive uptake results for OH from HONO. 1σ errors reflect the compounded effects of relative uncertainties in the magnitudes of all contributing appearance profiles. *PFPE is assumed to be 0.

The OH reactive uptake results for OH from HONO are representative of single collision conditions only. Therefore they do not agree with any of the studies presented previously which have a γ of > 1, as those do not represent single collision conditions correctly. The results do agree well with those of Wilson and co-workers [30] where those experiments also allowed single collision conditions to be observed.

For OH interaction with squalene to preferentially lose colder OH to reaction with double bonds, these bonds must be available at the surface of the liquid. For both squalane and squalene to produce, on average, more TD type OH both surfaces must be rough and flexible. To investigate whether or not this was all possible molecular dynamics (MD) simulations were performed on squalane and squalene. These simulations were performed by a project student [37] and are presented here to complement experimental findings.

5.5.4: Molecular dynamics simulations

Molecular dynamics simulations have been performed on the surfaces of squalane and squalene. These results are due to be published fully in an upcoming paper but have previously been described in part by a report [37]. The simulations were performed using the settings detailed in the following publication [42]. The results are summarised in figure 5.22.

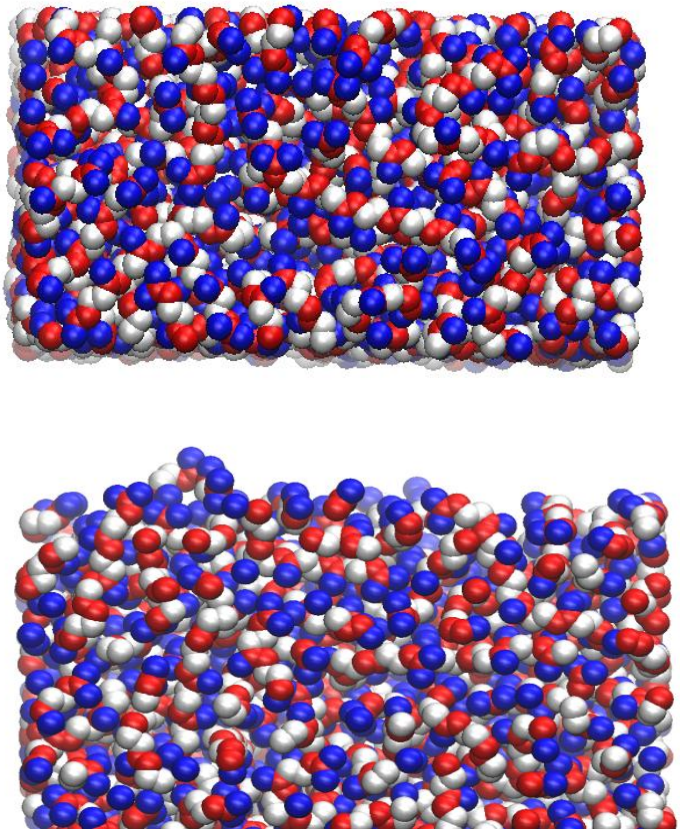

Figure 5.22: Squalene equilibrated surface after 2.3 ns of simulation. Above is the view from the top. Below is the side view. Pseudo-atoms are denoted as: CH_3 marked blue, CH_2 white and C=C red.

From figure 5.22 it can be first seen that the surface is rough, sometimes protruding into the vacuum. The surface also appears to be somewhat flexible as further rigidity would ensure a smoother surface.

It can be clearly seen from the figure that red pseudo-atoms which represent C=C carbons are present at the surface of the liquid squalane and the proposed mechanism of OH addition across the double bonds is entirely possible for OH generated both from HONO and allyl alcohol.

5.6: Conclusions

- The collision dynamics of collision of a rotationally hot source of OH interacting with both inert and potentially reactive liquid surfaces has been measured for the first time.
- The dominant scattering mechanism was found to be impulsive scattering from each of the liquids studied (PFPE, squalane and squalene). This mechanism was especially prevalent at high *N*.
- The first conclusive proof of the thermal trapping mechanism was obtained. This mechanism was naturally observed most easily in low *N* states.
- In all cases it was discovered that a quantity of energy was transferred to the liquid surface this occurred most effectively in the order squalane > squalene > PFPE.
- Translational and rotational correlation existed for all levels where the most rotationally excited molecules were also found to be travelling the fastest.
- Clearly extraction of populations revealed that more than a single temperature is necessary to describe the rotational distributions for all liquids at all the measured points in the appearance profiles. The lower temperature was revealed to be close to thermal while the upper temperature was less certain but typically clustered around ~ 1500 K.
- Many of these observations were also seen in previous HONO data and conclusions were further strengthened here.
- Squalane and squalene differences in both signal magnitude and subsequent scattering mechanisms were observed from both HONO and allyl alcohol especially at long times.
- These differences were proposed to be a possible loss of cold OH by addition across a double bond.
- This possibility was confirmed by the presence of double bonds at the liquid surface by the use of molecular dynamics simulations.
- Cold OH from HONO is useful for observing translational to rotational transformation of energy and for observing the IS mechanism.

- Using a hot source of OH such as allyl alcohol has enabled a much better optimisation of conditions for observing the TD mechanism.

5.7: References

1. P. A. J. Bagot, C. Waring, M. L. Costen and K. G. McKendrick, *J. Phys. Chem. C*, 2008, **112**, 10868-10877.
2. C. Waring, K. L. King, P. A. J. Bagot, M. L. Costen and K. G. McKendrick, *Phys. Chem. Chem. Phys.*, 2011, **13**, 8457-8469.
3. P. Warneck, *Chemistry of the Natural Atmosphere*, Academic Press, 1988.
4. B. J. Finlayson-Pitts and J. N. Pitts Jnr, *Chemistry of the Upper and Lower Atmosphere*, John Wiley & Sons., 2000.
5. D. E. Heard and M. J. Pilling, *Chem. Rev.*, 2003, **103**, 5163-5198.
6. D. Rosenfeld, *Science*, 2006, **312**, 1323-1324.
7. G. B. Ellison, A. F. Tuck and V. Vaida, *Journal of Geophysical Research-Atmospheres*, 1999, **104**, 11633-11641.
8. Y. Rudich, *Chem. Rev.*, 2003, **103**, 5097-5124.
9. D. E. Heard, *Annu. Rev. Phys. Chem.*, 2006, **vol. 57**, pp. 191-216.
10. D. J. Donaldson and V. Vaida, *Chem. Rev.*, 2006, **106**, 1445-1461.
11. P. Davidovits, C. E. Kolb, L. R. Williams, J. T. Jayne and D. R. Worsnop, *Chem. Rev.*, 2006, **106**, 1323-1354.
12. K. A. Prather, C. D. Hatch and V. H. Grassian, *Annu. Rev. Phys. Chem*, 2008, **vol. 1**, pp. 485-514.
13. B. J. Finlayson-Pitts, *Phys. Chem. Chem. Phys.*, 2009, **11**, 7760-7779.
14. I. J. George and J. P. D. Abbatt, *Nature Chem.*, 2010, **2**, 713-722.
15. A. Laskin, J. Laskin and S. A. Nizkorodov, *Environ. Chem.*, 2012, **9**, 163-189.
16. E. A. Weitkamp, A. T. Lambe, N. M. Donahue and A. L. Robinson, *Environ. Sci. Technol.*, 2008, **42**, 7950-7956.
17. A. T. Lambe, J. Y. Zhang, A. M. Sage and N. M. Donahue, *Environ. Sci. Technol.*, 2007, **41**, 2357-2363.
18. S. G. Moussa and B. J. Finlayson-Pitts, *Phys. Chem. Chem. Phys.*, 2010, **12**, 9419-9428.
19. A. K. Bertram, A. V. Ivanov, M. Hunter, L. T. Molina and M. J. Molina, *J. Phys. Chem. A*, 2001, **105**, 9415-9421.
20. J. H. Park, A. V. Ivanov and M. J. Molina, *J. Phys. Chem. A*, 2008, **112**, 6968-6977.
21. T. M. D'Andrea, X. Zhang, E. B. Jochnowitz, T. G. Lindeman, C. Simpson, D. E. David, T. J. Curtiss, J. R. Morris and G. B. Ellison, *J. Phys. Chem. B*, 2008, **112**, 535-544.
22. I. J. George, A. Vlasenko, J. G. Slowik, K. Broekhuizen and J. P. D. Abbatt, *Atmos. Chem. Phys.*, 2007, **7**, 4187-4201.
23. I. J. George and J. P. D. Abbatt, *Atmos. Chem. Phys.*, 2010, **10**, 5551-5563.
24. P. L. Cooper and J. P. D. Abbatt, *J. Phys. Chem.*, 1996, **100**, 2249-2254.
25. J. D. Hearn and G. D. Smith, *Geophys. Res. Lett.*, 2006, **33**.
26. L. H. S. Renbaum, G. D, University of Georgia, Athens, GA 30602, 2010.
27. V. F. McNeill, R. L. N. Yatavelli, J. A. Thornton, C. B. Stipe and O. Landgrebe, *Atmos. Chem. Phys.*, 2008, **8**, 5465-5476.
28. L. H. Renbaum and G. D. Smith, *Atmos. Chem. Phys.*, 2011, **11**, 6881-6893.
29. D. L. Che, J. D. Smith, S. R. Leone, M. Ahmed and K. R. Wilson, *Phys. Chem. Chem. Phys.*, 2009, **11**, 7885-7895.
30. J. D. Smith, J. H. Kroll, C. D. Cappa, D. L. Che, C. L. Liu, M. Ahmed, S. R. Leone, D. R. Worsnop and K. R. Wilson, *Atmos. Chem. Phys.*, 2009, **9**, 3209-3222.
31. C. Waring, Thesis publication, Heriot-Watt University, 2011.
32. R. Vasudev, R. N. Zare and R. N. Dixon, *J. Chem. Phys.*, 1984, **80**, 4863-4878.
33. S. Dhanya, A. Kumar, H. P. Upadhyaya, P. D. Naik and R. D. Saini, *J. Phys. Chem. A*, 2004, **108**, 7646-7652.
34. T. Y. Kang, S. K. Shin and H. L. Kim, *J. Phys. Chem. A*, 2003, **107**, 10888-10892.
35. H. Okabe, *Photochemistry of Small Molecules*, John Wiley & Sons, 1987.

36. J. C. Luque and D. R. Crossley, LIFBASE program, SRI International, 1999.
37. M. Iljina, *Molecular dynamics simulations of liquid squalane and squalene surfaces*, Heriot-Watt University, 2012.
38. M. E. King, G. M. Nathanson, M. A. Hanninglee and T. K. Minton, *Phys. Rev. Lett.*, 1993, **70**, 1026-1029.
39. M. E. Saecker and G. M. Nathanson, *J. Chem. Phys.*, 1993, **99**, 7056-7075.
40. M. E. King, M. E. Saecker and G. M. Nathanson, *J. Chem. Phys.*, 1994, **101**, 2539-2547.
41. G. M. Nathanson, *Annu. Rev. Phys. Chem.*, 2004, **55**, 231-255.
42. K. L. King, G. Paterson, G. E. Rossi, M. Iljina, R. E. Westacott, M. L. Costen and K. G. McKendrick, *Phys. Chem. Chem. Phys.*, 2013, **15**, 12852-12863.

Chapter 6: Reactions of O(^{3}P) at hydrocarbon surfaces

This chapter will describe an experimental study into the gas-liquid interfacial reaction of ground state oxygen, O(^{3}P), with the standard saturated liquid hydrocarbon squalane and its unsaturated counterpart, squalene. This is a continuation of the work of the McKendrick group on the interfacial reactions of O(^{3}P) with squalane [1-12]. There are a number of studies exploring the reaction dynamics of O(^{3}P) with squalane, where direct comparisons can be made. However, this is the first measurement for heterogeneous O(^{3}P) reactions with squalene and therefore no exact comparisons to the literature are possible.

6.1: Introduction to O(^{3}P) reactions with organic substrates

O(^{3}P) is abundant at altitudes 200 – 700 km above the Earth's surface [13]. This region is known as low Earth orbit (LEO) and is a region where satellites and spacecraft are likely to be found. O(^{3}P) has mechanisms of reaction which involve mainly hydrogen abstraction but can also include hydrogen elimination and C-C bond breakage. As a result of this, investigations into the reactions of O(^{3}P) with various substrates which contain hydrogen are relevant to the degradation of materials present on spacecraft and satellites.

The more specific desire to return to investigations of O(^{3}P) here was stimulated by the results of the OH generated from allyl alcohol study (Chapter 5). In that study, it was seen that the distributions of OH returning from squalane and squalene were different. Indeed a possible explanation for this discrepancy may have been the fact that OH was reacting with the squalene molecule by adding across the double bonds. It is even possible that the OH produced by the TD type mechanism was more likely to perform this type of reaction. That study was an example of inelastic scattering where the observed product and pre-collision species are the same. In order to further investigate these differences, squalane and squalene were studied using a reactive-type collision, where the pre-collision species differs from the scattered species. This will form the basis of this chapter where the scattering of O(^{3}P) from squalane and squalene will be studied. It is hoped that this will give an insight into the differences

between scattering from a saturated and unsaturated species and possibly shed some light into the preferred sites for reaction.

6.2: Past O(^{3}P) studies performed by the McKendrick Group

There is a large volume of literature on the subject of O(^{3}P) reactions with a variety of substrates. This literature has been summarised in Chapter 1. The brief further summary here will concentrate on measurements performed by the McKendrick group. As those experiments were performed using the same experimental set-up as the results presented here, they are of most relevance.

The McKendrick group have performed a wide number of studies on O(^{3}P) [1-12], including studies on temperature effects [4], linear versus branched reactivity [9] and an in-depth exploration of the direct scattering component [5]. Most directly relevant here is the basic, proof of concept study in which the reaction of O(^{3}P) with liquid squalane was investigated at room temperature [3].

In that initial study, McKendrick and co-workers measured the quantity of OH/OD produced in O(^{3}P) reactions with both squalane and its deuterated analogue. Appearance profiles and excitation spectra were measured. They detected vibrational ground state products as well as a minor quantity of v' = 1 vibrationally excited component, with $\frac{v'=1}{v'=0}$ = 0.07 for OH.

These results were compared to earlier gas-phase studies [1] conducted by the group. It was concluded that the small quantity of vibrationally excited OH must stem from an abstraction of H from either secondary or tertiary carbon groups or a combination of both, while v' = 0 OH was thought to occur as a result of abstraction from a primary carbon group. In a further paper using labelled SAM's [14], this idea was revised as it was found that reaction from primary sites was much less likely to occur, than from secondary or tertiary sites.

That original study not only identified that abstraction of hydrogen occurred but began to try and identify the likely sites for abstraction. In the current work new evidence will be presented to try and clarify the reaction dynamics associated with hydrogen abstraction. The use of squalene as an unsaturated counterpart is useful as the type of

hydrogens present differ between the two liquids. The extra possible mechanism of addition across the double bonds is introduced with the use of squalene. In the case of data presented here it is unlikely that C-C bond breakage mechanism will occur as the translational energy of the pre-collision $O(^3P)$ is not high enough.

6.3: Experimental summary

The broad experimental set-up for this series of experiments is detailed in Chapter 2. In this section details will be presented which are relevant to only this series of experiments. The liquid hydrocarbons squalane and squalene are used in this study and all experiments were performed at room temperature (297 ± 3 K).

In this case $O(^3P)$ atoms were generated from a low pressure (1 mTorr) of NO_2 (BOC 98 %) photolysed at 355 nm by an Nd:YAG laser (Continuum Surelite SLII-10) as shown in equation 6.1.

$$NO_2 + h\nu \rightarrow O(^3P) + NO \qquad \text{Equation 6.1}$$

The photolysis laser beam was approximately circular with a 5 mm diameter, with its centre situated 6 mm from the liquid surface. Typical pulses were ~ 20 ns in length with energies in the range of 50 - 70 mJ in the centre of the experimental chamber. The photolysis beam was horizontally polarised leading to an optimised fraction of the $O(^3P)$ generated travelling towards the liquid surface.

The OH returning from the liquid surface was probed by the second harmonic of a tuneable dye laser which was pumped by a second Nd:YAG laser (beam also at 6 mm distance, 3 mm diameter, pulse energies ~ 125 μJ) on the $A^2\Sigma^+ - X^2\Pi$ (1,0) band which occurs at around 280 nm. The returning fluorescence was detected by the laser light guide as described in section 2.8.1.

The $O(^3P)$ generated by photolysis of NO_2 has been well characterised previously. The speed is approximately Gaussian and has a lab frame kinetic energy of 15.8 kJ mol^{-1} and an average collision speed of 1340 ms^{-1}. The energy required to break each bond along with the energy available to products varies with the nature of the C-H bond type. An average aliphatic bond has a dissociation energy of 463 ± 2 kJ mol^{-1} while an

allylic bond has a dissociation energy of 372 ± 3 kJ mol^{-1}. The allylic bond is weaker as the allylic carbocation is more stable. When the allylic bond is broken, the reaction is more exothermic.

6.4: Experimental results

Obtaining results from the reaction of $O(^3P)$ with liquid squalane or squalene is much simpler than the experiments detailed in Chapter 5 where OH is present before and after collision. In this case the $O(^3P)$ is not observable by LIF at 282 nm and any OH signal which is seen must be from $O(^3P)$ which has reacted with the liquid surface to abstract a hydrogen and become OH. On return to the probe volume, the OH is detected by LIF and no subtractions are necessary as only this signal is observed.

6.4.1: Appearance profiles

A general description of appearance profiles was provided in section 2.9.1. The description given here will be more detailed and in some ways specific to this set of experiments. The term appearance profiles itself relates to the appearance of OH over time. This is collected while increasing the delay between photolysis and probe. During these scans the probe laser is set at a fixed wavelength of a selected transition.

The day-to-day collection of these appearance profiles followed a set procedure to ensure reproducibility. First a transition was selected (three were studied in this section of work $Q_1(1)$, $Q_1(5)$ and $Q_1(7)$) and the probe laser was set to the approximate wavelength; using the predicted wavelength from LIFBASE [15] as a guide. Then the probe laser was slowly scanned in both wavelength directions at a chosen photolysis-probe delay. The maximum signal at this delay was recorded and monitored regularly to check stability. The set of appearance profiles were then collected at this desired wavelength. Each set comprised of ~10 scans which were collected and then averaged.

After collecting each set of 10 scans, four further scans were taken. Two scans were conducted with the same experimental conditions except with the probe laser blocked. This was known as ‘photolysis only’. A further two scans were with all the same experimental conditions during data collection but with the photolysis laser blocked. These were known as ‘probe only’. Photolysis and probe only averages were both subtracted from the primary data to remove any scattered-light signal from the

lasers. Including these extra scans, each set took just over an hour to collect. All data presented below in graphical form were collected on at least three separate occasions and are therefore an average of around thirty separate appearance profiles. The raw data collected in this manner are presented in figure 6.1.

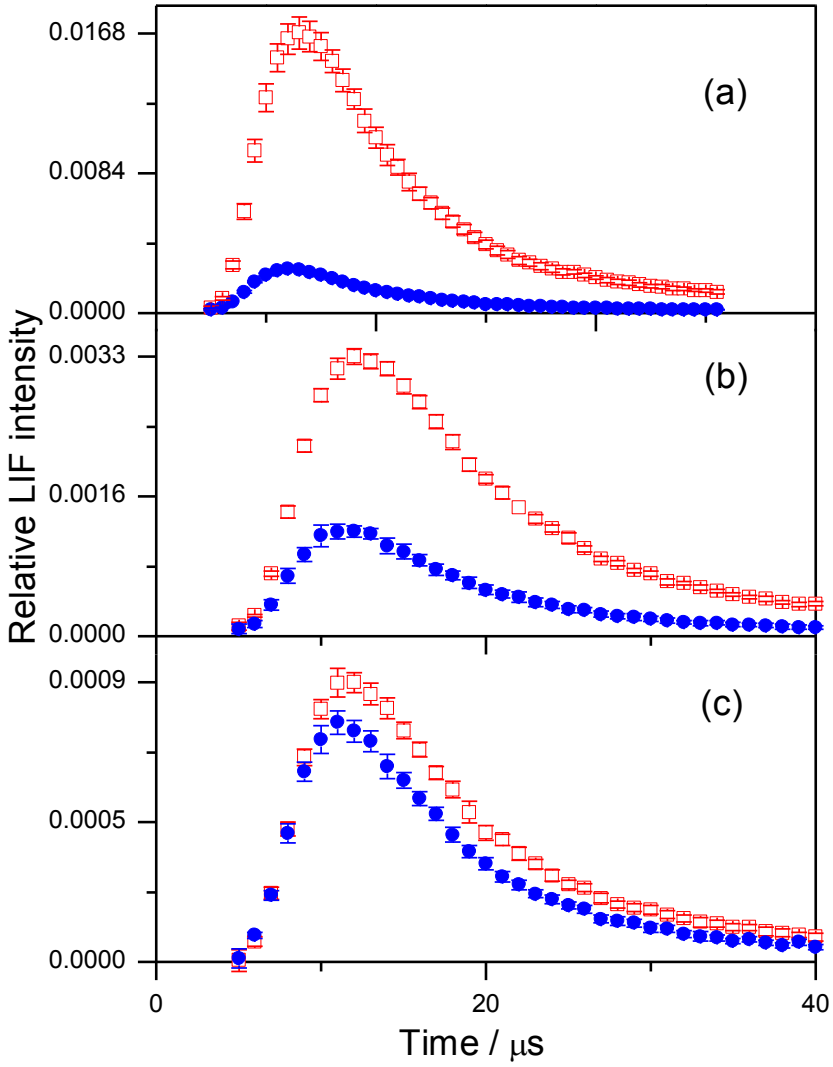

Figure 6.1: OH appearance profiles recorded on: (a) $Q_1(1)$; (b) $Q_1(5)$ and (c) $Q_1(7)$ from squalane (red open squares) and squalene (closed blue circles). Error bars represent the 1σ standard error of the mean.

It can be seen that the absolute signal size of both profiles is reducing as *N* increases, more striking is the difference between the relative sizes of the squalane and squalene profiles. At low *N*, the squalane signal dominates over the squalene but by *N* = 7 the squalene is almost comparable in size. The interpretation of this will be further explored in section 6.5.3. More subtle are the differences in shape between the

squalane and squalene profiles. The squalene profile appears to peak slightly before the squalane in all *N* levels and also the signal appears to decay faster than squalane. These differences are most easily observed in the *N* = 7 appearance profile but do occur throughout. The dynamical reasons for this will be further discussed in section 6.5.3. When comparing the appearance profile data, care should be taken when comparing the shapes of the appearance profiles at delays longer than ~30 μs, as the effects of secondary collisions can appear at or beyond this time delay [16].

Two types of background signals appeared in all of the results presented here. The first was a background from scattered probe light, present at all time delays, even when the photolysis laser was not firing; this was accounted for by subtraction of the probe only signal from the results collected. The second is a short-lived OH LIF signal, present only with both lasers firing. This signal was present after the photolysis pulse and may emanate from electronically excited NO_2 or OH which was the product of photolysis of an impurity in the NO_2 gas. One possible source of this impurity is HONO, which could form from any H_2O in the reaction chamber [17]. HONO could produce OH which would be detected by the experimental apparatus and interfere with the experimental results. However, this signal was only present at early times and does not interfere with the OH produced by reaction on the surface, as it only appears at times up to 5 μs. To ensure that contribution from this signal does not influence results, the appearance profile data is not shown before 5 μs.

However, some of this photolytically produced OH may undergo a collision with the liquid surface and subsequently be detected at later delays. This would therefore contribute to the signal in the appearance profiles. In order to determine whether or not this was occurring, profiles were recorded with the un-reactive liquid PFPE. A representative resulting appearance profile is shown in figure 6.2.

From the data in figure 6.2 it can be seen that the fraction of returning OH from PFPE is extremely small in comparison to the OH generated from squalane. From previous measurements conducted by the McKendrick group [18], it is known that the yield of inelastically scattered OH is lower for squalane and squalene when compared to PFPE. It is therefore reasonable to conclude that all OH detected in our appearance profiles occurs as a result of a reaction at the liquid surface and the quantity which may be

generated from an impurity and then subsequently detected after scattering inelastically from the liquid surface is extremely small.

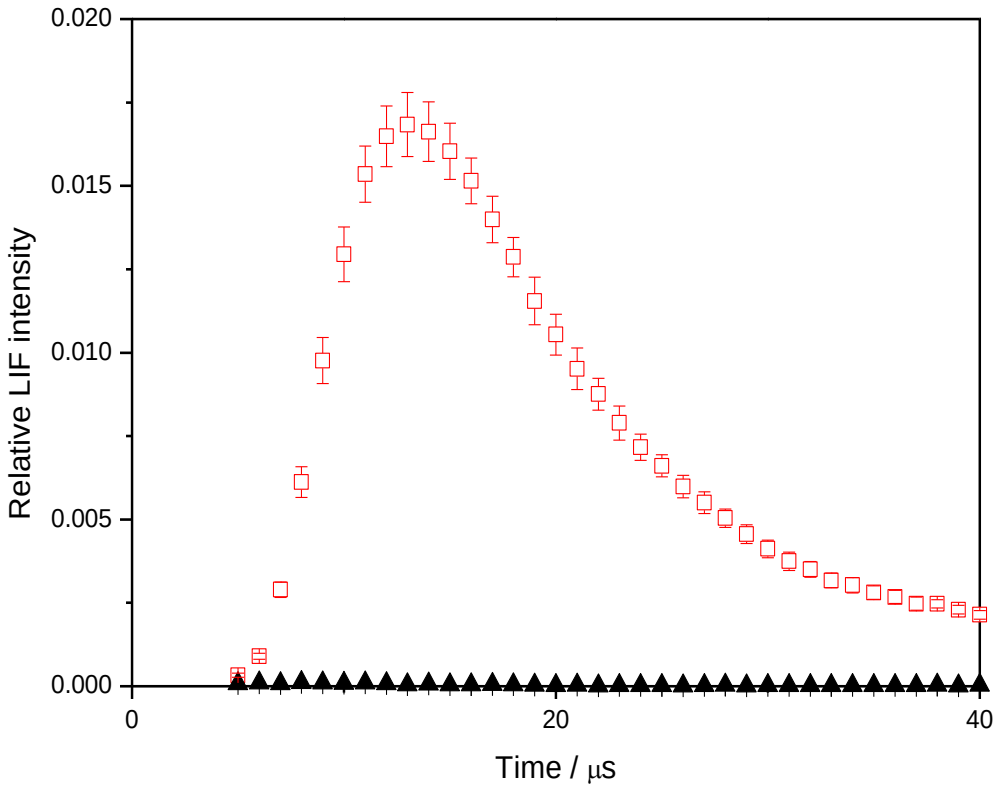

Figure 6.2: Appearance profiles taken on the $Q_1(1)$ line for squalane (open red squares) and PFPE(closed black triangles). The error bars represent the standard 1σ error in the mean.

6.4.2: Rotationally Resolved LIF Excitation Spectra

LIF excitation spectra were collected by varying the wavelength of the probe laser while keeping the delay between the photolysis and probe laser pulses constant. This resulted in a complete LIF excitation spectrum collected across a designated wavelength range.

The LIF excitation spectra were collected after the appearance profiles. From a consideration of the data collected in the appearance profiles; it was decided to collect excitation spectra at a delay of 12 μs. This delay was chosen to correspond to the average peak position of the three appearance profiles for each *N*. A thermalised spectrum was also collected by photolysing 1 mTorr NO_2 in the presence of 250 mTorr

of N_2. The spectrum was recorded at a delay of 30 μs. The higher pressure and long delays were specifically chosen to ensure that the OH produced had become thermally accommodated before the spectrum was collected.

To collect all of the excitation spectra presented a wavelength range was selected, using LIFBASE [15] to identify all the transitions beforehand. After a suitable wavelength range had been selected, a dye curve was constructed by choosing a probe power and setting the motor position of the doubling crystal at each point to ensure this probe power remained constant. This method of constructing a dye curve ensured correct ratios of one branch to another over the entire wavelength range. This method is preferable to setting a maximum power across the entire range where those transitions in the middle of the dye range, where the power is naturally higher, would falsely appear more intense. Once this dye curve had been learned, it was used to scan the wavelength range with each liquid hydrocarbon squalane or squalene present in the reaction chamber. The excitation spectra were collected by a pre-designed data collection programme which was constructed to only collect data within a narrow interval where transitions existed. For this reason, regions with no transitions present appear as straight horizontal lines. This is not representative of a background signal. Excitation spectra collected are presented in figure 6.3.

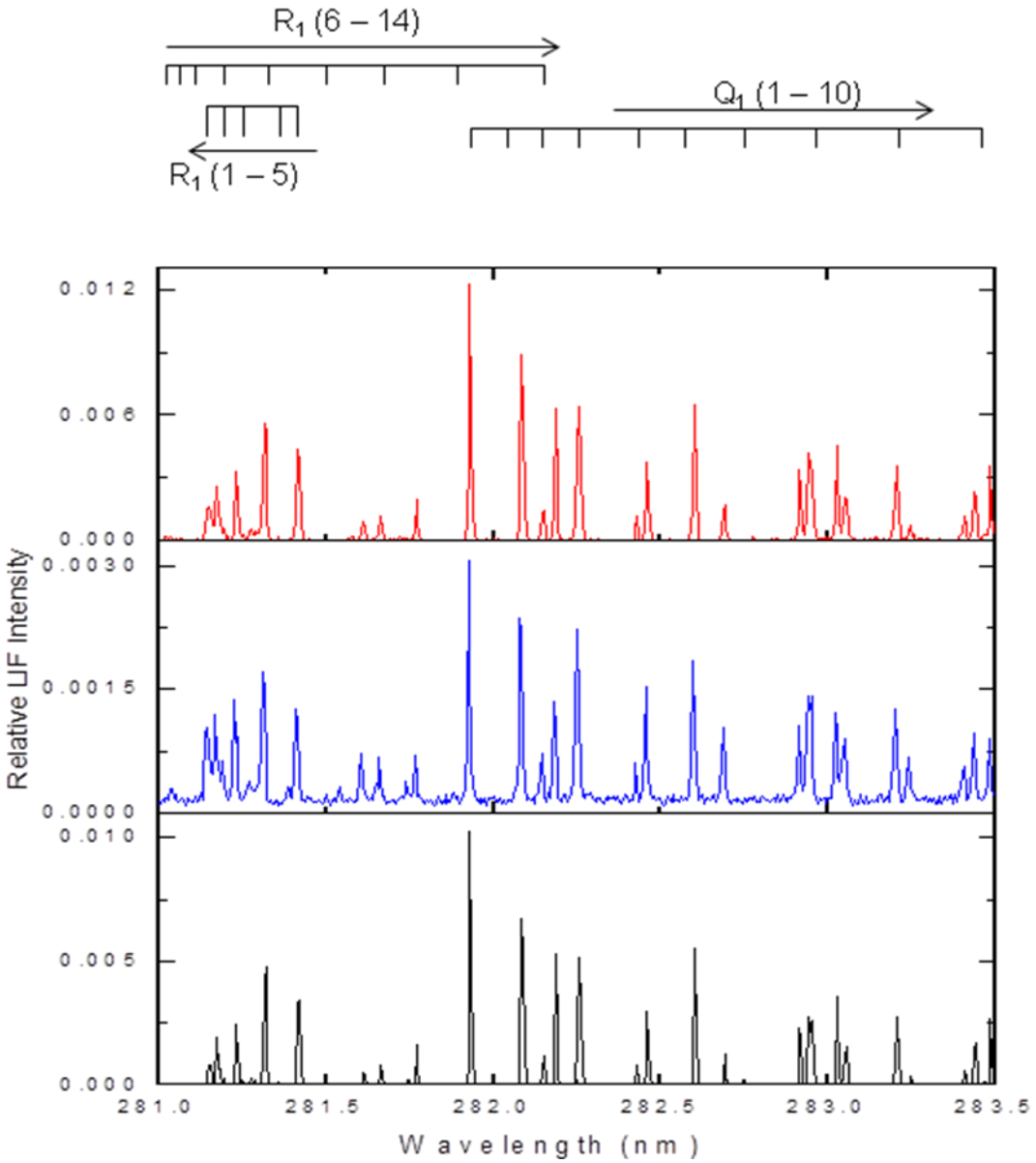

Figure 6.3: LIF excitation spectra on the OH *A-X* (1,0) band at a photolysis-probe delay of 12 μs. The squalane spectrum is shown in red, the squalene spectrum in blue and a subtraction of squalane – squalene in black. Bath temperature ~297 K, $p(N_2O)$ ~1 mTorr, *wheel-laser* axes distance = 6 mm.

At first glance, the spectra for squalane and squalene might appear quite similar. Again it can be noticed that the absolute OH return signal for squalane is much greater than squalene. This will be discussed in more detail in section 6.5.2. Looking more closely at the spectra, subtle differences can be seen between the two. This is perhaps most noticeable in the R_1 band-head which appears much larger for squalene (relative to low *N* lies in the same branch) than squalane. Indeed this general phenomenon appears to repeat throughout the spectrum where higher *N* lines appear larger in the

squalene spectrum (compared to the low *N* lines of the same branch) when compared to squalane. The dynamic rationale for this will be explored in section 6.5.2.

6.5: Analysis of results

To extract any more quantitative information from the results presented in section 4.4, further processing must take place. The most complex of these cases applies to the excitation spectra, where several steps are required to extract populations and subsequently discern other properties such as rotational temperatures. The methods used and information gathered will be presented in the following sections.

6.5.1: Extraction of populations

To try and confirm whether or not the scattered OH conforms to a single rotational temperature, a Boltzmann plot must be constructed where the population of each, individual *N* level divided by the degeneracy is plotted against the energy for each level. The first step in completing this process is to extract populations from the collected excitation spectra presented in figure 6.3.

To extract the populations from an excitation spectrum, the simulation programme LIFBASE was used [15]. The collected excitation spectrum is imported into the simulation programme and the baseline wavelength settings are adjusted so that any wavelength offset is corrected. For each branch in turn, the heights of the simulated spectrum are then adjusted to match the heights of the experimental data collected. For each branch in turn, the heights of the simulated spectrum are matched to the heights of the experimental data collected. The programme then transforms the heights into relative populations. These relative populations can be turned in to absolute populations if required by measuring the intensity of the LIF signal at one particular transition and multiplying the relative populations by this number. In the excitation spectra, it may not be possible to extract populations from all lines as they may be overlapped with another from a different branch. In this case, these lines will be absent from the population data collected. The population data extracted are shown in figures 6.4 and 6.5.

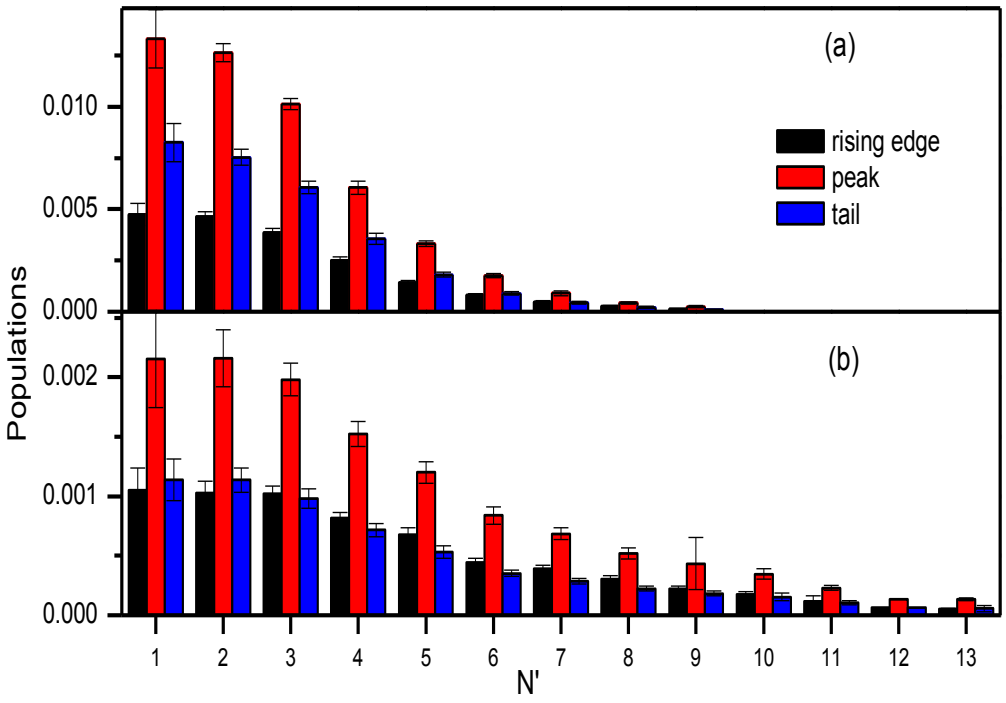

Figure 6.4: Panel (a) shows the OH rotational populations from squalane and panel (b) shows the OH rotational populations from squalene (extracted from the excitation spectra as described in the text). Black bars show populations collected at the rising edge (8 μs); red bars show populations from the peak (12 μs) and blue bars show populations from the tail end of the appearance profile (20 μs).

Looking at the populations in figure 6.4, it is easy to see that for squalane, the distributions differ at each delay. The rising edge population is smaller than the tail population at low *N* but is almost equal by the *N = 8* level. The peak populations also begin much larger than the rising edge and tail populations but by *N = 8*, all populations appear similar in magnitude. This means that the populations collected at an earlier delay are hotter than the populations collected at a later delay.

The squalene populations differ from the squalane populations. They are much smaller in overall magnitude but are spread over more rotational levels. For squalene, the population of all levels measured at the peak is always higher than the rising edge and tail populations. Also the tail populations are larger than the rising edge at low *N*, but the rising edge population becomes larger than the tail by *N = 3*. It appears that at the two highest rotational levels that the magnitudes of these populations are very similar.

These trends are obviously dynamical in origin, possible reasons for them will be discussed in section 6.5.2. To better compare squalane and squalene, the populations at the peak of each distribution have been shown together in figure 6.5.

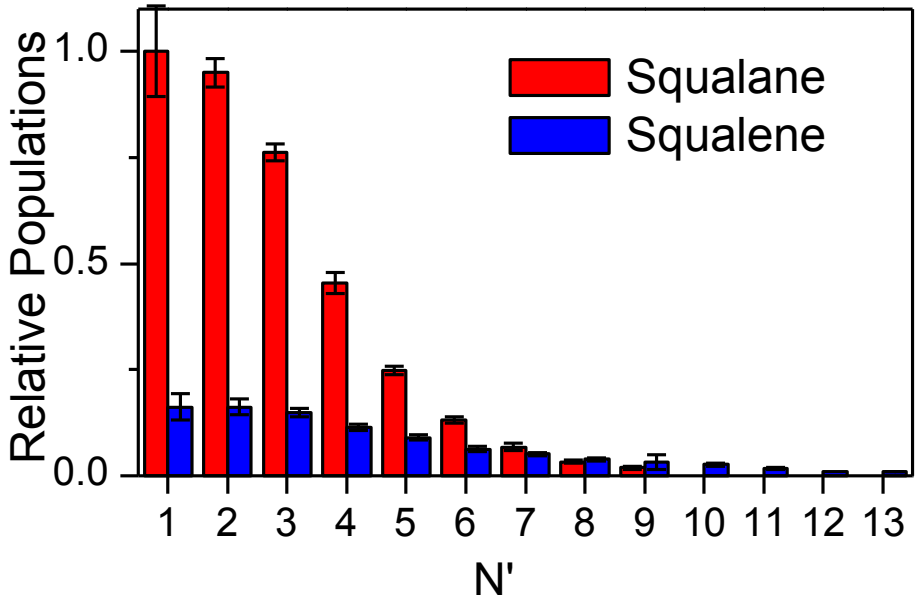

Figure 6.5: Relative populations as a function of rotational quantum number, *N'*, for squalane (red) and squalene (blue) from the delay corresponding to the peak of the appearance profile (12 μs). Squalane is normalized to one at its largest line. Squalene is shown in the correct relative ratio.

Looking at the two liquids together, as shown in figure 6.5, it is much easier to observe the differences in the overall magnitudes of the population. The squalane signal is over four times larger than the squalene signal at the lowest *N* levels but by the time *N=8* is reached the squalene signal is larger and the squalane signal is too small to be seen by *N = 10*.

6.5.2: Analysis of populations

Once the LIF excitation spectra have been transformed into populations, further steps can be taken to transform the populations into Boltzmann plots from which the rotational temperatures can be extracted. The extracted population for each *N* level is divided by the degeneracy of that specific *N* level and then a natural log of this is taken. This value is plotted against the energy of each specific *N* level. This will provide a Boltzmann plot, from which temperature(s) can be extracted (shown in Figure 6.6). If the plot is linear then only a single temperature is present and extraction of the

temperature is simple as it is contained within the slope of the graph. If the graph shape is curved then the temperature must be fitted to a minimum of two-temperature model according to the formula presented in equation 6.2.

$$\frac{P(N')}{g'_j} = c\left(\frac{\propto \exp\left(-\frac{E(N')}{k_B T_1}\right)}{T_1} + \frac{(1-\alpha)\exp\left(-\frac{E(N')}{k_B T_2}\right)}{T_2}\right)$$

Equation 6.2

Where P(*N*) are the populations specific to each *N* level, g_j is the degeneracy at each specific level. C is a n overall scaling constant. T_1 is the colder temperature and T_2 is the hotter temperature. α is the proportion of molecules with the colder temperature T_1. E (*N*) is the energy at each specific *N* level and k_B is the Boltzmann constant.

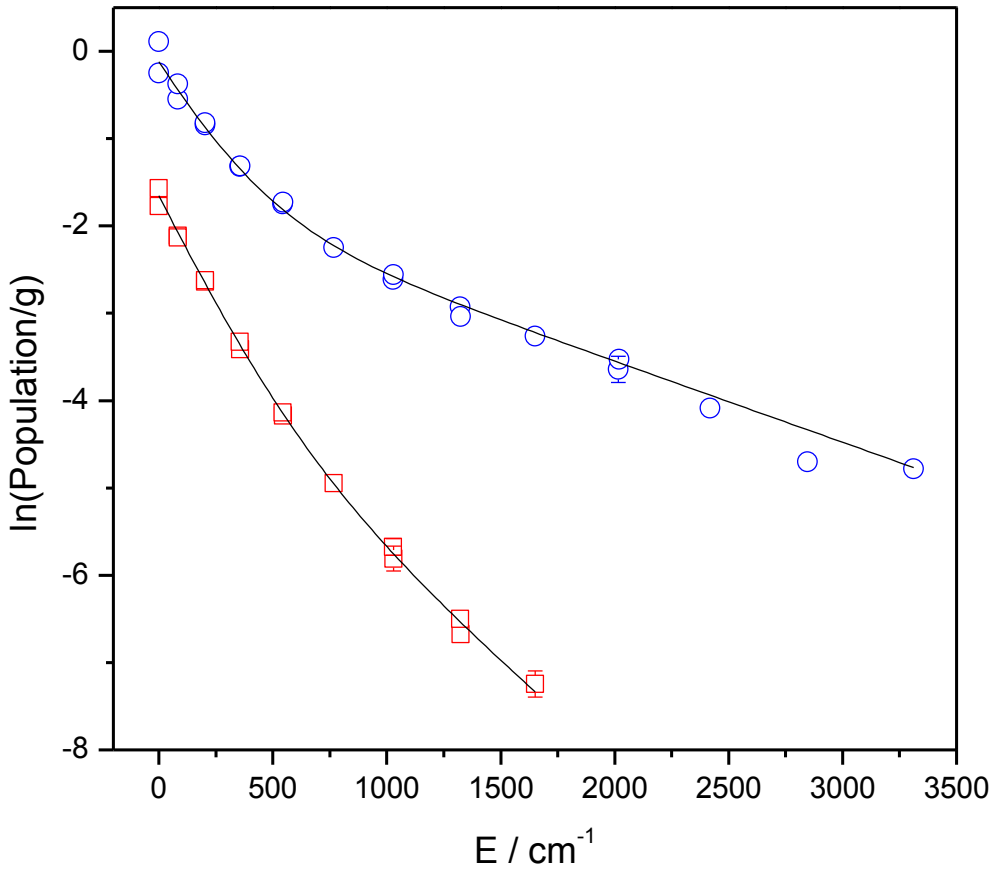

Figure 6.6: The populations collected at the peak of the appearance profiles (12 μs) have been transformed into Boltzmann plots (as described in the text) to extract temperatures. Squalane is shown as open red squares while squalene is shown as open blue circles. Error bars represent the standard 1σ error in the mean.

Observing figure 6.6, it can be seen that the neither the squalane or squalene distribution conforms to a straight line. This means that neither distribution can be fitted to a single temperature. In this case both distributions have been fitted to the dual temperature model as described in equation 6.2. Observing the Boltzmann plot it can be seen that even qualitatively squalane and squalene look very different. Squalane is only slightly curved and indeed may at first be mistake for a single temperature distribution. Squalene is very obviously curved and much hotter than squalane overall. The best-fit dual temperatures extracted are presented in table 6.1.

Squalane			
Delay / μs	α	T_1 / K	T_2 / K
8	0.73 ± 0.12	290 ± 28	818 ± 239
12	0.70 ± 0.13	256 ± 26	625 ± 124
20	0.70 ± 0.20	249 ± 34	559 ± 143
Squalene			
8	0.35 ± 0.06	268 ± 38	1106 ± 275
12	0.43 ± 0.05	301 ± 34	1588 ± 128
20	0.53 ± 0.03	290 ± 19	1606 ± 216

Table 6.1: The results of the dual temperature fitting for squalane and squalene at the rising edge, peak and the tail of the appearance profile distribution as collected from the Boltzmann plots of the type shown in Figure 6.6. The confidence intervals represent a standard error of 1σ in the mean.

From the information presented in table 6.1, it can be seen that each of the liquids has a lower temperature which roughly corresponds to thermal (within error margins). Provided that the reaction occurring is direct then this temperature would not be lower than the temperature of the liquid, even in a thermal desorption mechanism. As the liquid temperature is ~ 298 K, this is the lowest reasonable temperature for a direct process.

The second temperature is the hotter component of the two-temperature distribution; this temperature ranges from 600 – 800 K for squalane and 1100 – 1600 K for squalene.

Dynamically there are two possible explanations for these differences. The end result is probably due to a combination of both. First, and the most likely possible explanation is that squalene contains a large number of allylic sites where hydrogens can be abstracted. These allyl hydrogens are much more weakly bound and are more exothermic than aliphatic C-H bonds as discussed in section 6.3. The presence of these allyl sites may be responsible for the differences in T_2 for squalene compared to squalane. Secondly the O(^{3}P) and the formed OH may add across the double bond and be lost. This mechanism is most likely to occur for those molecules involved in a trapping desorption mechanism because of their longer residence time at the surface. If this were the case then the squalene distribution would appear hotter than the squalane. From the data presented in Chapter 5, it has already been shown by molecular dynamics simulations that the double bonds present in the squalene are present at the surface of the liquid, meaning than an addition mechanism is possible. These are also the reasons why the squalene high *N* lines appeared larger than the squalane high *N* lines in the excitation spectra.

In figure 6.7, the normalised squalane and squalene distributions are plotted with a Monte Carlo simulation (described fully in appendix 1) of the trapping desorption mechanism.

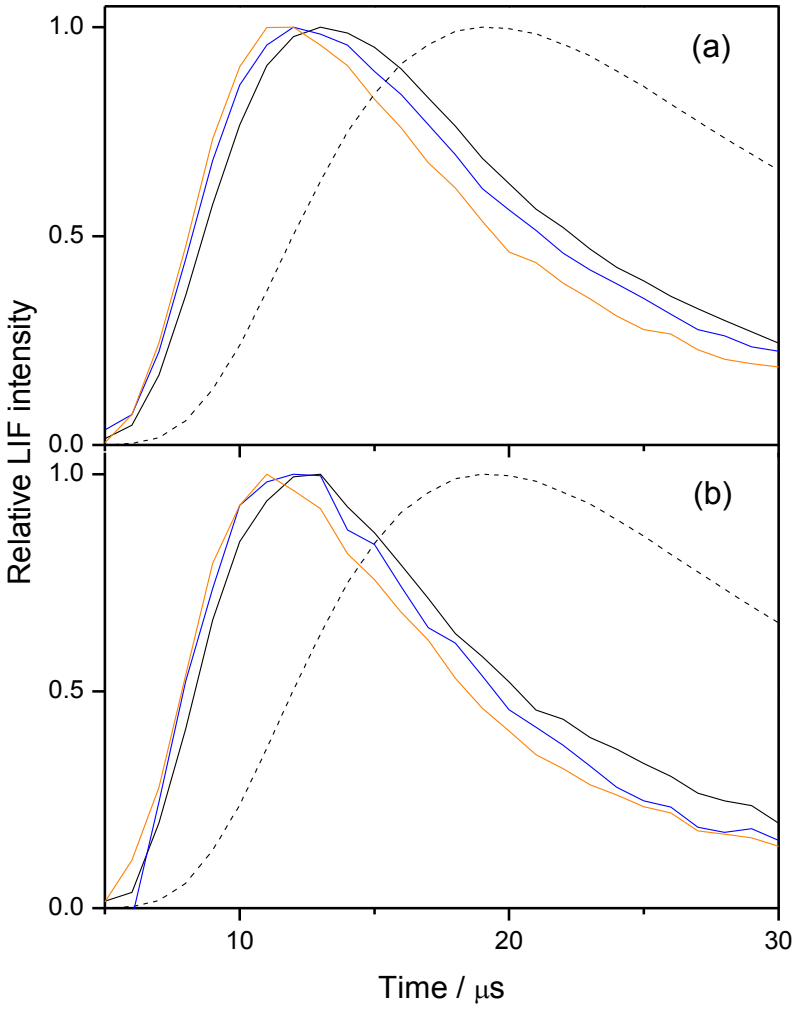

Figure 6.7: Squalane (a) and squalene (b): $Q_1(1)$ – black line, $Q_1(5)$ – blue line and $Q_1(7)$ – red line. The Monte Carlo generated TD simulations are shown as dashed black lines. All profiles have been normalised at the peak of their distributions.

From the profiles shown in figure 6.7, it can be seen that for both liquids, a substantial fraction of the observed scattering is generated from the impulsive scattering mechanism. This can be said definitively as the scattering is simply too early to be from a TD style mechanism. In both liquids, it can also be said that at least some of the later scattering is consistent with a trapping desorption style mechanism. This point is further enhanced by the fact that for both liquids, the tails descend in the order of low to high *N*. This occurs as more TD style molecules are present in low *N* levels.

There are also observable differences between the two liquids. The squalane curve is much wider at the peak than the squalene curve. The squalene curve appears to decay more rapidly once past the peak. These differences may be attributed to either the fact that slower O(^{3}P) or generated OH is adding preferentially across the double bonds of squalene or the liquid surface itself. The nature of the squalane surface is soft and flexible. It is therefore a better energy sink and tends to be effective at rotational cooling. Squalene still has a measure of rigidity from the double bonds and is not as effective at cooling molecules during collision. However these effects are likely to only show minor contributions to results at the most.

The most likely cause of the variations between squalane and squalene stems from the nature of the carbon bonds. The variation occurs from the presence of the double bonds in squalene which effectively remove hydrogens and change the nature of the carbon bonds from all aliphatic (in squalane) to having some allylic bonds (in squalene). Allylic bonds are weaker than aliphatic bonds (as discussed in section 6.3) and therefore release more energy during bond dissociation. This added exothermicity is likely responsible for the changes in T_2 as presented in table 6.1. These variations are also likely to cause the differences shown in figure 6.7 where it can be seen that squalane produces more TD style OH than squalene.

This study is presently ongoing and more data are being collected to further strengthen the arguments presented here. The nature of the work being undertaken is discussed further in Chapter 7.

6.6: Conclusions

- The dynamics of reactive scattering of $O(^3P)$ from liquids has been expanded to include scattering from an unsaturated hydrocarbon.
- Impulsive scattering and trapping desorption style mechanisms were observed from both liquids.
- Squalene produced less OH overall than squalane.
- Extracted populations showed dynamical differences between the rising edge, peak and tail collection points of squalane and squalene.
- Scattering of $O(^3P)$ from both squalane and squalene exhibited more than one temperature when fitted to a Boltzmann model with the upper temperature for squalene was much greater than for squalane.
- A likely cause of these liquid differences was attributed to the presence of allylic C-H bonds in squalene which are more exothermic than aliphatic C-H bonds.
- Another possible minor cause of these differences was proposed to be the preferential adding of TD style $O(^3P)$ and OH across the double bonds.

6.7: References

1. F. Ausfelder and K. G. McKendrick, *Prog. React. Kinet. Mech.*, 2000, **25**, 299-370.
2. F. Ausfelder, H. Kelso and K. G. McKendrick, *Phys. Chem. Chem. Phys.*, 2002, **4**, 473-481.
3. H. Kelso, S. P. K. Kohler, D. A. Henderson and K. G. McKendrick, *J. Chem. Phys.*, 2003, **119**, 9985-9988.
4. S. P. K. Kohler, M. Allan, H. Kelso, D. A. Henderson and K. G. McKendrick, *J. Chem. Phys.*, 2005, **122**, 024712.
5. S. P. K. Kohler, M. Allan, M. L. Costen and K. G. McKendrick, *J. Phys. Chem. B*, 2006, **110**, 2771-2776.
6. S. P. K. Kohler, S. K. Reed, R. E. Westacott and K. G. McKendrick, *J. Phys. Chem. B*, 2006, **110**, 11717-11724.
7. M. Allan, P. A. J. Bagot, M. L. Costen and K. G. McKendrick, *J. Phys. Chem. C*, 2007, **111**, 14833-14842.
8. M. Allan, P. A. J. Bagot, S. P. K. Kohler, S. K. Reed, R. E. Westacott, M. L. Costen and K. G. McKendrick, *Phys. Scr.*, 2007, **76**, C42-C47.
9. M. Allan, P. A. J. Bagot, R. E. Westacott, M. L. Costen and K. G. McKendrick, *J. Phys. Chem. C*, 2008, **112**, 1524-1532.
10. C. Waring, P. A. J. Bagot, M. T. Raisanen, M. L. Costen and K. G. McKendrick, *J. Phys. Chem. A*, 2009, **113**, 4320-4329.
11. C. Waring, P. A. J. Bagot, J. M. Slattery, M. L. Costen and K. G. McKendrick, *J. Phys. Chem. A*, 2010, **114**, 4896-4904.
12. C. Waring, P. A. J. Bagot, J. M. Slattery, M. L. Costen and K. G. McKendrick, *J. Phys. Chem. Letts.*, 2010, **1**, 429-433.
13. E. Grossman and I. Gouzman, *Nucl. Instrum. Methods Phys. Res. Sect. B-Beam Interact. Mater. Atoms*, 2003, **208**, 48-57.
14. C. Waring, P. A. J. Bagot, M. W. P. Bebbington, M. T. Raisanen, M. Buck, M. L. Costen and K. G. McKendrick, *J. Phys. Chem. Letts.*, 2010, **1**, 1917-1921.
15. J. C. Luque and D. R. Crossley, SRI International, 1999.
16. R. Vasudev, R. N. Zare and R. N. Dixon, *J. Chem. Phys.*, 1984, **80**, 4863-4878.
17. K. A. Ramazan, D. Syomin and B. J. Finlayson-Pitts, *Phys. Chem. Chem. Phys.*, 2004, **6**, 3836-3843.
18. C. Waring, K. L. King, P. A. J. Bagot, M. L. Costen and K. G. McKendrick, *Phys. Chem. Chem. Phys.*, 2011, **13**, 8457-8469.

Chapter 7: Concluding Remarks and Future Work

This chapter will summarise the goals set at the beginning of this thesis and evaluate the extent to which they have been met. This chapter will also describe the future work that would be interesting to investigate using the current experimental set-up.

The aims of this thesis were to improve the current understanding of reactions at the gas-liquid interface, infer the nature of the liquid surface and, where relevant, relate results to reactions which occur in atmospheric chemistry.

7.1: O^1D concluding remarks and future work

This thesis presented the first results on the collision dynamics of $O(^1D)$ with a liquid surface (Chapter 4). This study was used to investigate the dynamics of reaction of $O(^1D)$ with liquid squalane and inferences were made about the scattered OH produced from this reaction. The discovery of a dual temperature in the scattered species was made and some scattered products could be attributed to reaction mechanisms used to describe corresponding gas-phase experiments.

As this study was the first of its kind, there are a great variety of further investigations which could be completed using $O(^1D)$ as a collision species. An interesting study would be to detect any vibrationally excited OH produced from $O(^1D)$ reacting with squalane. The results collected could be compared with known reaction pathways observed in comparable gas-phase reactions.

Another logical thing to do would be to investigate the collision dynamics of $O(^1D)$ with an unsaturated species such as squalene. The results of this could then be compared to the results of $O(^3P)$ and OH with the same liquids. $O(^1D)$ could also be used with SAM surfaces and the results compared to $O(^3P)$. $O(^1D)$ has a higher speed and collision energy and it would be interesting to see whether this means that the $O(^1D)$ projectiles can penetrate and react with carbons further down the SAM chain than was possible for $O(^3P)$ [1].

7.2: OH concluding remarks and future work

In Chapter 5 allyl alcohol was used to generate a rotationally hot source of OH. The dominant scattering mechanism was confirmed to be impulsive scattering. Strong evidence of a trapping desorption was also presented and believed to be an alternative scattering mechanism. Use of the rotationally hot source of OH made the trapping desorption much easier to characterise. In this case a dual rotational temperature was also observed in the scatter from liquids PFPE, squalane and squalene. Properties of the scattered OH were liquid dependent and reflected the nature of the liquid surface.

The work on OH is most relevant to reactions occurring in the troposphere. It would be very useful to investigate the effects of different functional groups on the scattering dynamics of OH from liquids. This may include alcohols, aldehydes and ketones, all of which may be found in the troposphere as a part of aerosols. In addition to this, specifically relating to allyl alcohol, there is a small quantity of population present in the excited vibrational state (~10 %). It would be interesting to investigate the dynamics of scattering of the excited vibrational state and compare these to the ground vibrational state. In our investigations, both a thermal and hot source of OH have been used as pre-collision species. Currently within the McKendrick group, a molecular beam is being developed so that the dynamics of collisions of an internally cold source of OH with variable translational energy can be investigated with various liquid surfaces. Results from an internally cold source would be interesting to compare with both the thermal and hot sources of OH already completed.

7.3: O(^{3}P) concluding remarks and future work

Using O(^{3}P) the differences in reactive scattering dynamics from a saturated and an unsaturated hydrocarbon liquid were investigated. Both liquids exhibited a dual rotational temperature the extent of which varied with each liquid. Large differences were seen for the scattering dynamics from squalane and squalene. The dominant reason for this was attributed to the presence of allylic carbon bonds in squalene which altered the scattering dynamics. Chapters 5 and 6 showed the possibility of an addition mechanism for either OH or O(^{3}P) across the double bonds in the unsaturated liquid, squalene, although this contribution was thought to be minor. It is believed that

the slower, TD style post-collision species are more likely to perform this type of reaction.

The O(^{3}P) study was only a small part of ongoing work which is occurring within the McKendrick group presently. The dynamics of scattering of the vibrational state (v = 1) of OH generated from reaction of O(^{3}P) with a liquid surface from both squalane and squalene is to be investigated. The results of this are to be compared and contrasted with the OH ground vibrational state data presented here. In addition to this the scattering dynamics, the mechanisms will be explored in more depth. After this, the ongoing plan is to investigate the scattering dynamics of O(^{3}P) from ionic liquid surfaces. Previous studies by the McKendrick group have begun this work [2, 3] but there is much scope to investigate a wider variety of ionic liquids.

7.3: References

1. C. Waring, P. A. J. Bagot, M. W. P. Bebbington, M. T. Raisanen, M. Buck, M. L. Costen and K. G. McKendrick, *J. Phys. Chem. Letts.*, 2010, **1**, 1917-1921.
2. C. Waring, P. A. J. Bagot, J. M. Slattery, M. L. Costen and K. G. McKendrick, *J. Phys. Chem. A*, 2010, **114**, 4896-4904.
3. C. Waring, P. A. J. Bagot, J. M. Slattery, M. L. Costen and K. G. McKendrick, *J. Phys. Chem. Letts.*, 2010, **1**, 429-433.

Appendix 1: Monte Carlo Simulations

In each results chapter of this thesis (Chapters 4 – 6), Monte Carlo (MC) simulations were conducted to simulate the thermal desorption component of the collision of projectiles with the liquid surfaces. In chapter 4, MC simulations were also used to model the impulsive scatter of $O(^3P)$ from the liquid surface. This appendix will describe the process used to generate these simulations.

The simulation is set-up to model the probe laser as a cylinder and the photolysis laser as a cuboid. They are both centred at the same point. The shapes of each laser and distance from the liquid wheel can be changed as necessary, for variances in each experiment. The liquid light guide is directly above the laser axes and has a 1 cm diameter where fluorescence can be detected. Only the top half of the wheel is modelled as the bottom half will be in the liquid filled bath and unavailable for collision. The wheel is modelled as its actual size.

The MC simulations model individual free flight paths (with no force fields) emanating from any point in the photolysis laser cuboid. The angular and velocity distributions are randomly selected from a pre-set range (speed from the correct weighted speed distribution and angle using the correct weighted angular distribution including anisotropy considerations.) This simulation determines from the x and y co-ordinates (where z = 0,0) whether the radical will hit the liquid wheel or not. Both the hits and non-hits are counted along with the length of travel to the surface.

For the return journey, the simulation can calculate from an inelastic collision, a thermal desorption mechanism or a random mix of both. For the thermal trapping desorption return the journey begins from the same coordinates as the collision (this time, z is included). The velocity is calculated from a Maxwell-Boltzmann thermalised distribution of speeds (cos θ) and the angle from an evenly distributed azimuthal (cone) angle. If the line does not intersect the cylinder, the OH is not detected. However, the intersection of this trajectory with the laser cylinder from the probe beam in the region where the liquid light guide is counts as a single detection (effectively a 3D intersection of a line and circle). The simulation also detects the exit points on the cylinder to ensure the time spent in the cylinder is known as one OH can

contribute to multiple time points. The information can then be used to plot a simulation curve, of the types shown in chapter 4-6.

Appendix 2: Publications

Please note that all publications were published under the author's maiden name and therefore are credited as K. L. King.

1: *Collision Dynamics and Reactive Uptake of OH Radicals at Liquid Surfaces of Atmospheric Interest*

C. Waring, K. L. King, P. A. J. Bagot, M. L. Costen and K. G. McKendrick; *Phys. Chem. Chem. Phys.*; 2011, **13**, 8457 – 8469.

2: *Dynamics of the Gas-Liquid Interfacial Reaction of $O(^1D)$ with a Liquid Hydrocarbon*

C. Waring, K. L. King, M. L. Costen and K. G. McKendrick; *J Phys. Chem. A*; 115, **25**, 7210 – 7219.

3: *Inelastic Scattering of OH Radicals from Organic Liquids: Isolating the Thermal Desorption Channel*

K. L. King, G. Paterson, G. E. Rossi, M. Iljina, R. E. Westacott, M. L. Costen and K. G. McKendrick; *Phys. Chem. Chem. Phys.*; 2013, **15**, 12852 – 12863.

4: *Site and Bond Specific Dynamics of Reactions at the Gas-Liquid Interface*

M. A. Tesa-Serrate, K. L. King, G. Paterson, M. L. Costen and K. G. McKendrick; *Phys. Chem. Chem. Phys.*; 2014, **16**, 173 – 183.